RADIATION-INDUCED CONDUCTIVITY IN AMORPHOUS CARBON

Thesis by

Todd J. Jones

In Partial Fulfillment of Requirements
for the Degree of
Doctor of Philosophy

California Institute of Technology
Pasadena, California

1989

(Submitted April 5, 1989)

ACKNOWLEDGMENTS

I thank my wife, Dorothy Razulis, for all of her patience and support during my stay at Caltech. I am indebted to her for her assistance with voluminous data entry, word processing, and general vax omniscience. I also thank Dr. Tombrello for providing the ways and means of performing this research. He gave advice that was useful both academically and economically. He was also very patient with my frequent dead ends and diversions.

Additional thanks go to the many people at Caltech who gave support, moral and otherwise: Duncan Weathers created Figure 3.6 and provided valuable "how-to" experience with respect to design and machining; Alan Rice maintained the Tandem Accelerator in excellent working order and helped with the electronics; Max Dobeli assisted with the temperature effects; Bruce Vogelaar gave much of his time to show me how to use the Nufit program; Fulin Xiong and Rogerio Livi helped to fine-tune the ion beam when needed; Steve Spicklemire and Gary Gutt gave their time and efforts to make the computational work go smoothly; Dr. Thad Vreeland made the Nikon Profile Projector available; Mechelle Vine provided the secretarial prowess necessary to keep the group going in the Caltech environment.

Finally, I thank my parents and grandparents who made it possible for me to benefit from a quarter-century of quality education.

ABSTRACT

Amorphous carbon films were irradiated with high energy chlorine ions with energies between 1 and 45 MeV. The electrical conductivity was measured *in situ* over a range of doses from 2×10^{10} to 5×10^{15} $ions/cm^2$. It was found that the conductivity increases over three to four orders of magnitude. The variation of the conductivity with temperature is successfully fitted by a Mott hopping conduction model. The energy sensitivity of the effect (excitation curve) does not parallel the electronic stopping power of chlorine in carbon, but a multihit δ electron theory based on an ion-track model closely matches the excitation curve. The 1 and 2 MeV irradiations show the effect of nuclear stopping associated with low energy irradiation.

TABLE OF CONTENTS

ACKNOWLEDGMENTS ii

ABSTRACT iii

TABLE OF CONTENTS iv

I. INTRODUCTION 1

- 1. Electrical Conductivity 1
- 2. Amorphous Carbon 2
- 3. Importance of Increased Conductivity 7

II. EXPERIMENTAL 8

- 1. Samples and Preparation 8
- 2. Sample Irradiation 9
- 3. Conductivity Measurements 11

III. THEORY 15

- 1. Electrical Conduction in Amorphous Materials 15
- 2. Ion-Track Model For High Energy Ion Modification of the Electrical Properties of Matierials 17

IV. ANALYSIS 28

- 1. Setting Up Conductivity vs. Dose Curves 28
- 2. Thermal Modeling of Targets 34
- 3. Investigation of Mott Conductivity 35
- 4. Correcting Beam Heating Effects 43

V. RESULTS 47

- 1. A Close Look at Conductivity vs. Dose 47
- 2. Cross Sections for Conductivity Change 47
- 3. Cross Sections at Different Energies 56
- 4. Comparision with the Ion-Track Model 63

VI. CONCLUSIONS 69
1. Temperature-Dependent Conductivity 69
2. Cross Sections and Hydrogen Loss 69
3. Low Energy Effect 70
4. Further Work 70
APPENDIX A 72
APPENDIX B 81
REFERENCES 95

I. INTRODUCTION

1. Electrical Conductivity

Electrical conductivities of materials are known to cover a larger range than any other physical property. From teflon to silver there is a span of 25 orders of magnitude in the room-temperature conductivity. At lower temperatures this range goes to infinity when superconductors are considered. This latitude comes about because the conductivity σ depends on both the number n and the mean-free path ℓ of the charge carriers in the medium:

$$\sigma = \frac{ne^2\ell}{mv_o} , \tag{1.1}$$

where m is the carrier effective mass and v_o is the Fermi velocity of the carrier. In comparison to σ and ℓ the mass and velocity are relatively constant for different materials. For the best insulator the low carrier concentration is due to a large band gap E_g between the filled valence band and the empty conduction band. Fermi-Dirac statistics yield the law of mass action for the carrier concentration:

$$n_i = 2\left(\frac{k_BT}{2\pi\hbar^2}\right)^{3/2}(m_c m_v)^{3/4}\exp\left[\frac{-E_g}{2k_BT}\right] , \tag{1.2}$$

shown in its intrinsic form for low impurity concentrations. With the effective carrier masses m_c and m_v equal to the standard electron mass, and the temperature $T = 300°K$:

$$n_i = 2.5 \times 10^{19}\ \exp\left[\frac{-E_g}{2k_BT}\right] \quad carriers/cm^3 . \tag{1.3}$$

Large band gaps, such as $5.47eV$ (Sz81), for diamond are known. With the mass-action law this band gap would provide $10^{-27} carriers/cm^3$. However, the likely existence of impurities and defects will give rise to a much higher minimum concentration. If that is taken to be about 1 $carrier/cm^3$ then a concentration range may be estimated. At the other extreme, the carrier concentration of a metal is approximately equal to the atomic concentration of the material, *e.g.*, 10^{23} $carriers/cm^3$. That gives 23 orders of magnitude to be credited to the carrier concentration. For the mean-free path, insulators provide a lower bound of the order of the atomic spacing: ~ 1Å. The upper bound is determined by crystalline purity and regularity. A perfect crystal (at $T = 0 \deg K$) 10 cm in length is reasonable. This limit credits nine orders of magnitude in variability to the mean-free path. Together, the carrier concentration and mean-free path provide approximately 32 orders of conductivity. The appearance of more orders than the 25 mentioned earlier occurs because the extremes in the cases of carrier concentration and mean-free path need not exist in the same material. Table I categorizes various materials and lists their conductivities. The table shows that amorphous carbon has a conductivity intermediate to diamond and graphite.

2. Amorphous Carbon

Carbon as an element finds its way into all forms of life. Mankind eats, breathes and lives by carbon. The highly symmetric sp^3 bonding state yields a material of ultimate hardness: the diamond. Diamonds cut, polish, and decorate. The sp^2 bonding state provides one of the softest yet strongest materials: graphite. Graphite lubricates friction intense surfaces. It forms fibers of great strength. Electrical motors depend on graphite brush blocks for the smooth delivery of high currents to moving parts. It is used as electrodes in caustic processses where no other material would survive. The random arrangement of both sp^3 and sp^2 bonding states produces a substance which is plain filthy: amorphous carbon. Amorphous carbon is used as the industrial precursor to graphite. Available as lampblack, carbon black, acetylene black, bone char, vegetable char, and coke, amorphous carbon is pyrolyzed to form the crystal graphite. Lampblack and carbon black are the

TABLE I

Conductivities *

Substance	Conductivity $(\Omega cm)^{-1}$	Ref.
Metals, Semimetals	10^3–10^6	
Silver	630520	a
Copper	595950	a
Gold	446000	a
Aluminum, 99.996%	376680	a
Calcium, 0°C	256000	a
Beryllium	250000	a
Magnesium	225000	a
Rhodium	222000	a
Sodium	210000	a
Iridium	190000	a
Molybdenum, 0°C	190000	a
Tungsten, 27°C	177000	a
Zinc	169000	a
Brass, 70% copper	162000	b
Cobalt	160000	a
Niobium boride	155000	c
Cadmium, 0°C	146000	a
Nickel	146000	a
Yellow brass	143000	d
Titanium	140000	b
Potassium	139000	a
Phosphor bronze	130000	e
Indium	121000	a
Osmium	110000	a
Plain carbon steel	110000	d
Lithium	108000	a
Iron, 99.99%	103000	a
Red brass, 85% copper (casting)	100000	d
Platinum, 99.85%	94300	a

a *Handbook of Chemistry and Physics* 66th *Edition* (CRC Press, 1985), F-120.
b *Handbook of Chemistry and Physics* 66th *Edition* (CRC Press, 1985), F-111.
c F.W. Glaser, J.Met., **4** (1952), 391
d *Handbook of Chemistry and Physics* 66th *Edition* (CRC Press, 1985), C-184.
e *Handbook of Chemistry and Physics* 66th *Edition* (CRC Press, 1985), E-88.

---

* at room temperature unless noted otherwise.

TABLE I (cont.)

Conductivities *

Substance	Conductivity $(\Omega cm)^{-1}$	Ref.
Metals, Semimetals (cont.)	10^3–10^6	
Tin, 0°C	90000	a
Tantalum	80320	a
Chromium, 0°C	77500	a
Gallium	57500	a
Cesium	48880	a
Lead	48431	a
Molybdenum silicide	46500	f
Vanadium	38500–40300	a
Uranium	33000	a
Arsenic	30000	a
German silver, 18% nickel	30000	e
Natural graphite (Ticonderoga) σ_a	26000	d
Antimony, 0°C	25600	a
Zirconium	25000	a
AgPd disordered alloy	23800	g
Molybdenum boride α	22000	h
400 Monel	20700	b
Kovar	20400	b
Yttrium	17500	a
Cast gray iron	15000	f
Stainles steel, AISI Type 316	13500	b
600 Inconel	10200	b
Mercury, 50°C	10200	a
NiCr disordered alloy	9000	g
Plutonium, 107°C	7072	a
Manganese α	5400	a
AlTi disordered alloy	5000	g

a *Handbook of Chemistry and Physics* 66th *Edition* (CRC Press, 1985), F-120.
b *Handbook of Chemistry and Physics* 66th *Edition* (CRC Press, 1985), F-111.
d J.R. Ferraro, J.M. Williams, *Introduction to Synthetic Electrical Conductors* (Academic Press, 1987), p.254.
e *Handbook of Chemistry and Physics* 66th *Edition* (CRC Press, 1985), E-88.
f F.W. Glaser, J.Appl.Phys., **22** (1951), 103.
g J.H. Mooij, Phys. Stat. Sol., **17** (1973), 521.
h R. Steintz, J.Met., **4** (1952), 148.

---

* at room temperature unless noted otherwise.

TABLE I (cont.)

Conductivities *

Substance	Conductivity $(\Omega cm)^{-1}$	Ref.
Semiconductors	10^{-9}–10^{3}	
Carbon, graphite, 0°C	727.3	a
Germanium, p-type, $10^{15} cm^{-3}$ impurities	3.4	i
Boron carbide	1.3–3.3	j
Selenium	1.0	a
Tellurium	0.229	a
Silicon, p-type, $10^{15} cm^{-3}$ impurities	0.083	i
GaAs, p-type, $10^{15} cm^{-3}$ impurities	0.046	i
Amorphous carbon	0.04–0.25	k
Silicon carbide	0.0050–0.00935	j
Insulators	10^{-20}–10^{-5}	
Corning 0080 glass, 350°C	8.0×10^{-6}	l
Boron, 0°C	5.6×10^{-7}	a
Diamondlike carbon films	10^{-7}	m
Alkali halide crstals	10^{-8}–10^{-2}	n
Vycor 7900 glass, 350°C	7.7×10^{-9}	l
Iodine	7.7×10^{-10}	a
Pyrex 1710 glass, 350°C	4×10^{-10}	l
G. E. Clear (silica glass), 350°C	3×10^{-11}	l
Cellulose nitrate	10^{-11}	o
Neoprene rubber	10^{-12}–10^{-11}	p
Polyvinyl chloride (PVC)	10^{-12}–10^{-11}	o
Hydrogenated amorphous carbon, a-CH:H	10^{-12}	q
Phenolic molding compounds (Bakelite)	10^{-13}–10^{-9}	o
Silicone rubber	10^{-13}	p

a *Handbook of Chemistry and Physics* 66th *Edition* (CRC Press, 1985), F-120.
i S.M. Sze, *Physics of Semiconductor Devices* 2nd *Edition* (John Wiley & Sons, New York, 1981), p.32.
j I.E. Campbell, *High Temperature Technology* (John Wiley & Sons, New York, 1956).
k This work.
l *Handbook of Chemistry and Physics* 66th *Edition* (CRC Press, 1985), E-56.
m S. Prawler et al., J.Appl.Phys., **61** (1987), 4492.
n N.W. Ashcroft, N.D. Mermin, *Solid State Physics* (Saunders College, Philadelphia, 1976), p.621.
o J.B. Birks, *Modern Dielectric Materials* (Heywood & Company, London, 1960).
p F.M. Clark, *Insulating Materials for Design and Engineering Practice* (John Wiley & Sons, New York, 1962).
q B. Dischler et al., Solid State Comm., **48** (1983), 105.

---

* at room temperature unless noted otherwise.

TABLE I (cont.)

Conductivities *

Substance	Conductivity $(\Omega cm)^{-1}$	Ref.
Insulators (cont.)	10^{-20}–10^{-5}	
Viton A rubber	10^{-13}	r
Asbestos paper with Silicone resin impregnant	10^{-13}	p
Porcelain	10^{-14}–10^{-12}	r
SiO_2 (quartz), $\parallel$ to principal axis	10^{-14}	j
Diamond	2×10^{-15}	s
Beeswax, yellow	1.3×10^{-15}	r
Magnesium oxide	10^{-15}	j
Polymethyl methacrylate (Super Glue)	10^{-15}	o
SiO_2 (vitreous)	10^{-15}	j
Styrene-butadiene rubber	10^{-16}–10^{-14}	p
Muscovite mica	10^{-16}–10^{-15}	p
Alumina (aluminum oxide), 14°C	10^{-16}	j
Parawax	10^{-16}	r
SiO_2 (quartz), $\perp$ to principal axis	5×10^{-17}	j
Natural rubber	10^{-17}–10^{-15}	p
Paper with dielectric impregnant	10^{-17}	o
Phosphorus, white, 11°C	10^{-17}	a
Sulfur, yellow	5×10^{-18}	a
Titanium dioxide	10^{-18}–10^{-13}	r
Titanate ceramics	10^{-18}–10^{-15}	p
Polytrifluorochloroethylene	10^{-18}	o
Ceresine wax	2×10^{-19}	r
Paraffin	10^{-19}–10^{-15}	r
Polyethylene	10^{-19}	o
Polyethylene terephthalate (Mylar)	10^{-19}	o
Polystyrene	10^{-19}	o
Polytetrafluoroethylene (Teflon)	10^{-19}	o
G.E. H26X aluminosilicate glass	10^{-20}	o

a *Handbook of Chemistry and Physics* 66th *Edition* (CRC Press, 1985), F-120.
j I.E. Campbell, *High Temperature Technology* (John Wiley & Sons, New York, 1956).
o J.B. Birks, *Modern Dielectric Materials* (Heywood & Company, London, 1960).
p F.M. Clark, *Insulating Materials for Design and Engineering Practice* (John Wiley & Sons, New York, 1962).
r *Handbook of Chemistry and Physics* 66th *Edition* (CRC Press, 1985), E-55.
s R. Berman, *Physical Properties of Diamond* (Clarendon Press, Oxford, 1965), p.9.

---

* at room temperature unless noted otherwise.

light-absorbing basis of printing inks and toners. Bone char and vegetable char are important as efficient fluid filters. The amorphous carbon used in the research described herein is in the form of evaporated thin foils. These delicate foils are typically intended to strip electrons from energetic ions after the first stage of acceleration in a tandem accelerator.

3. Importance of Increased Conductivity

Highly conductive pathways written on an otherwise insulating surface could be useful to the electronics industry for making intricate connections between devices. Certain polymer films have been found to be semiconducting (Ta80). These films show increased conductivity by chemical doping (Ch77), (Ni79). It is possible to produce p-n junctions in the films; however, they are unstable and last about a month in the open air (No84); however, the possibility of inexpensive plastic integrated circuits should not be dismissed. A thorough understanding of the conduction process in carbon films seems supportive of the goal to stabilize doped junctions in polymer films, because there is an implicit similarity between amorphous carbon and multiply linked chains of hydrocarbons. Some amorphous carbon films are inherently heavily hydrogenated ~20 *to* 30 *atomic percent* (Ba83). Thus, this work is partially in response to the growing interest in ion-irradiated polymer films. In particular, much work is being put forth to understand the modification of electrical properties of such films: (Ab82), (Dr84), (Hi83), (Ma83), (Ve83). The early beginnings of this project go back to the experiments of Venkatesan et al. (Ve85), where amorphous carbon films were bombarded with high and low energy ions. The conductivity was found to decrease with low energy ions and to increase with high energy ions. They found these processes to be 100% reversible. The purpose of this study was to improve upon and explore further the high energy process.

II. EXPERIMENTAL

1. Samples and Preparation

Thin films of amorphous carbon were purchased from the *Arizona Carbon Foil Company.* These films were produced by evaporation of spectrographically pure graphite. The films are deposited under high vacuum on one inch by three inch microscope slides. The substrates are held far enough away from the resistive source so that they are found cool to the touch upon removal: $\sim 40°C$ *. A proprietary release agent is applied to the glass slide prior to evaporation. This "detergent" disolves when the films are floated free from the glass slide. The film's surface density is measured optically with ±10% accuracy. It is uniform to ±10% across the microscope slide. Product literature from *Arizona Carbon Foil* states that the density of the foils used in this work is $2.00 \pm 0.02 g/cm^3$.

These films were presliced into $0.127cm \times 2.44cm$ strips with curved surgical blades. It was noticed that the blades dulled quickly because of the abrasive edge of the glass slide. To assure smooth edges on the samples the blades were shifted frequently in their mounts so as to expose fresh portions of blade. Each portion of blade performed no more than three cuttings. When all the portions of a blade's cutting edge were used up, the blade was replaced with a new one. The rough edge of the microscope slides was avoided as much as possible.

After ten strips had been cut, the backside of the slide was scored with a glass cutter to sever the part and its strips. This was then tapped lightly to break off the prepared part. The next step was to suspend the part with its ten slices over one liter of ultra-pure water. A lab jack was used to raise the pool of water steadily up to the sliced film. When the piece of

---

* Private communication 10/13/88 with John Stoner of *Arizona Carbon Foils.*

glass was submerged, all ten slices would be liberated—usually intact. Each of the floating slices was then trapped and mounted on a $0.64cm \times 2.54cm$ portion of microscope slide. These were attached with small strips of *Scotch Double Stick Tape* to a brass holder. The holder accommodated six samples. The samples were chosen so that their glass slide mount thickness were all the same to within $\pm 3\mu m$. This proved to be critical for good electrical contact of the amorphous carbon to the ion beam current integrator. This electrical contact was achieved by a narrow brass bar pressed down upon the six samples at their left edges. If one sample was thinner than the rest, then that sample would not have electrical contact with the brass bar. This would be detected by the four-point probe only after the samples were in the chamber under vacuum. To increase the odds of getting good contact with all samples, the brass bar was wet-sanded immediately prior to placement in order to remove any oxide layer. The pristine films are very delicate and subject to scratching by the least mechanical abrasion. The brass bar was spring-loaded to restrain it from rubbing the samples as it was clamped upon them.

Three of these six-packs of targets were mounted on three sides of an hexagonal target holder made of aluminum. They were electrically isolated from the hexagon by $0.50cm$ slabs of plexiglass. Their electrical contact to the beam current integrator came via individual wires. This electrical isolation is necessary when very small beam currents are used. The target positioning shaft would otherwise introduce noise into the current integrator by the motion of static charge on nearby moving parts such as people's arms.

2. Sample Irradiation

High energy chlorine ion beams were generated with the Caltech Tandem Van de Graff accelerator. Ions of specific charge and energy bombarded the samples through a rectangular collimator made of $0.16cm$ quartz plates. The size of the collimator was $0.199cm \times 0.638cm$. The collimator was located about two inches upstream from the samples. The ion beam was rastered at $\sim$10 Hz on the x axis and $\sim$1 Hz on the y axis. The typical beam spot was about $0.2cm$ in diameter. This produced a uniform dose across the sample, which was free of Lissajous-type patterns. The beam was precollimated further upstream from the quartz collimator. The precollimation was achieved by closing adjustable slits to the point where the luminescence from the edge of the quartz was almost gone. This practice tends to cut down on the number of wide angle ions straying beyond the region of planned irradiation. The samples were adjusted vertically to coincide with the quartz collimator. The region of planned irradiation straddles the width of the carbon sample. Precise vertical adjustment is possible using a level telescope to check sample position relative to the collimator center line.

Beam current integration accuracy was improved by using $300V$ batteries to deflect secondary electrons. A biased grid was positioned $1.3cm$ in front of the samples along with another cylindrical grid surrounding the entire hexagonal target holder. These grids were maintained at $-300V$. The target holder is grounded through the current integrator. The effect of the biased grids is twofold. First, they repel secondary electrons dislodged from the grounded quartz collimator. Second, they turn back secondaries leaving the target.

Beam currents from 0.4nA to 100nA were used depending on ion charge state and energy. It was found that the change in sample conductivity was independent of the magnitude of the beam current. High beam currents caused the samples to warm up faster. This produced a small temperature effect, to be discussed later.

3. Conductivity Measurements

Sample conductivities were measured *in situ* with an *Alessi* C4S four-point probe. The probe uses spring-loaded osmium tips with radii of 0.005 *inch*. The tips are spaced 0.0500 ± 0.0005 *inch* apart. The manufacturer set the probe-tip spring pressure to 40 *grams* in equivalent weight. The probe-tip pressure used in this work was much less, by necessity. The *Alessi* unit was lab-modified with ultrafine set screws in order to bring all four tips into a common line. It is important that the four tips land simultaneously on the delicate pristine carbon films. No pressure is needed to make an ohmic contact to the carbon. The probe was mounted on a swing arm, which was controlled by one of the two directional arms in the 24-inch central scattering chamber shown in Figure 2.1. Large angle swings of the probe arm moved the four spring-loaded osmium tips out of the way of the ion beam. Fine control of the assembly was achieved by pinning the atmosphere side of the lever to a modified tool-holding micrometer secured to the top rim of the chamber. The probe tips were thus eased onto the film with $6 \mu m$ accuracy. Pushing the tips any further than this quickly destroyed pristine films. Irradiated films were seemingly indestructible.

The probe assembly was also useful in aligning the targets. The four tips were in a horizontal plane which bisected the ion beam's quartz collimator. The tips were brought up close to the sample and the vertical target adjustment was moved to center the target strip with respect to the probe tips. This could be done very accurately (to ±5% of the sample width) with the leveled telescope mentioned earlier. The four-point probe was also useful in making sure that the sample was perpendicular to the ion beam to ±10 minutes of arc. This was accomplished by adjusting the target holder's rotational position until probe tips number 1 and 4 touched the film surface simultaneously. This alignment step was always done at the edge of the

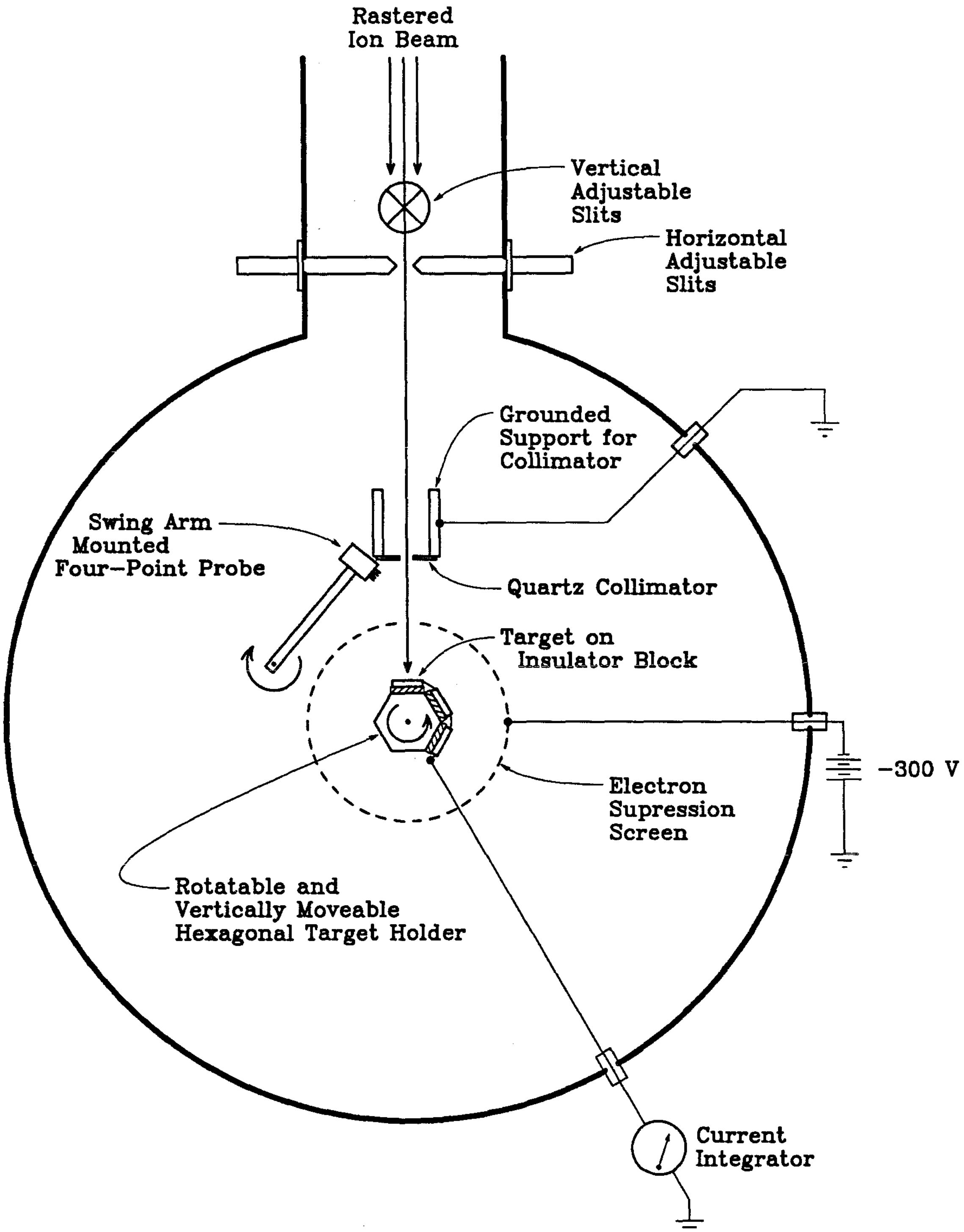

Figure 2.1

Target setup for sample irradiation in the 24 inch scattering chamber on the Caltech EN Tandem Van de Graff accelerator. Only one electron suppression screen is shown.

target strip, where scratches would not interfere with probe contact in the center of the sample.

Probe tips 1 and 4 send a direct current through the carbon strip. Tips 2 and 3 measure the IR voltage generated by the passing current. Pristine samples required approximately $1\mu A$ to generate 1 volt. As the resistivity dropped the driving current would have to be stepped up occasionally to maintain a significant voltage across tips 2 and 3. Heavily bombarded samples required as much as $2mA$. The current sent through the samples came from a *Keithley 225* current source which was stable to about one part in a thousand. The voltage across tips 2 and 3 was measured with a *Keithley 614* multimeter which has as input impedence of $10^{14}\Omega$. The *Keithley 614* was also used to give an accurate measure of the current from the *Keithley 225.*

The sample conductivity is given by the inverse of the resistivity:

$$\sigma = 1/\rho \ . \qquad 2.1$$

The resistivity is given by the formula:

$$\rho = \Lambda \frac{v}{i} \ , \qquad 2.2$$

where Λ is a geometrical factor derived in Appendix A. The most important factors in Λ are sample width w and thickness τ and probe-tip spacing s:

$$\Lambda \propto \frac{w\tau}{s} \ . \qquad 2.3$$

The sample thicknesses were determined by dividing the film's surface density M by the density of the amorphous carbon D:

$$\tau = M/D \ . \qquad 2.4$$

Both quantities were provided by *Arizona Carbon Foil.* Typical film thicknesses were ~ 1000Å.

The samples' widths were all measured postirradiation on a large screen projection microscope (*Nikon Model 6C Profile Projector*). During this measurement any abnormalities could be spotted. Some samples had very rough edges—evidence of a dull cutting blade. One showed a crack in the film which nearly isolated it from the beam-current integration bar. All samples showed that the zone of irradiation straddled the narrow strip of carbon. The irradiated portions appear metallic and are readily noticed. Occasionally probe-tip sitz marks are visible. Using a particular array of sitz marks, it was possible to obtain an accurate measure of the probe-tip spacing s. It was found to be $0.1262 \pm 0.0003 cm$.

III. THEORY

1. Electrical Conduction in Amorphous Materials

Electrical conduction in amorphous carbon can be successfully modelled by the temperature-dependent hopping conduction formula,

$$\sigma = \sigma_o \exp\left[-\left(\frac{C}{k_B T}\right)^{\alpha}\right] , \tag{3.1}$$

originally derived by Mott (Mo68) with $\alpha = \frac{1}{4}$. In this model, electrons move by phonon-induced tunneling between localized states. These states are randomly located in the amorphous medium. Their energies are also randomly distributed within the mobility gap. The principal dependence of the factor C is:

$$C = \frac{\lambda s^3}{g} , \tag{3.2}$$

where s is the exponential decay length of the localized s-like states, g is the density of the localized states, and λ is a dimensionless constant whose exact value depends on the method of derivation (Am71).

In the process of irradiation with heavy ions, structures may be produced in the amorphous media. These will be likely places for electron traps or localized states. Thus, the increase in conductivity with ion beam dose may be a manifestation of an increase in the density of localized states. There may also be an effect upon the decay length s of those localized states.

The temperature exponent used in Equation (3.1) is $\alpha = 0.25$. There is, however, conflicting experimental evidence that leaves the value of α ambiguous (Mo87). As shown by Hamilton in 1972, the value of α is determined by the functional form of the density of states written as (Ha72):

$$g(E) = g_o E^p , \tag{3.3}$$

where E is the energy above or below the Fermi level. To derive Eqn. (3.1) Mott uses $p = 0$ to represent a constant density of states. The number of states that exist within a sphere of radius R and have energy E from the Fermi level is:

$$\begin{aligned} n &= \frac{4\pi R^3}{3} \int_0^E g(E) dE \\ &= \frac{4\pi R^3}{3} \frac{g_o E^{p+1}}{p+1} \quad . \end{aligned} \tag{3.4}$$

The conduction process is represented by a hop of an electron within this sphere. When the sphere is just large enough to contain one state, the hop will be made. Setting $n = 1$ and calling δE, the hopping energy gives the sphere's radius:

$$R = \left[\frac{3(p+1)}{4\pi g_o (\delta E)^{p+1}} \right]^{\frac{1}{3}} \quad . \tag{3.5}$$

The tunneling probability between two s-like states separated by distance R is:

$$|T|^2 \propto e^{-2sR} \ , \tag{3.6}$$

where s is the exponential decay length of the s-state written as e^{-sR}. The Boltzman factor can be used to estimate the number of electrons with energy δE above the Fermi level. Together these give the probability of hopping conduction:

$$\nu \propto \exp\left[-2\alpha R - \frac{\delta E}{k_B T} \right] \quad . \tag{3.7}$$

Using Eqn.(3.5) in this expression, the minimum of the exponent occurs when:

$$\delta E_{min}^{\frac{(p+4)}{3}} = \left(\frac{3(p+1)(2\alpha)^3}{4\pi g_o} \right)^{\frac{1}{3}} \frac{(p+1)}{3} k_B T \ , \tag{3.8}$$

which gives:

$$\nu \propto \exp\left[-\left(\frac{C}{k_B T} \right)^{\frac{(p+1)}{(p+4)}} \right] \ , \tag{3.9}$$

where

$$C^{\frac{(p+1)}{(p+4)}} = \left(\frac{6\alpha^3}{\pi g_o}\right)^{\frac{1}{(p+4)}} \left[\left(\frac{3}{p+1}\right)^{\frac{(p+1)}{(p+4)}} + \left(\frac{p+1}{3}\right)^{\frac{3}{(p+4)}}\right] (p+1)^{\frac{1}{(p+4)}} \ . \qquad (3.10)$$

The conductivity will be proportional to the probability ν in Equation (3.9):

$$\sigma = \sigma_o \exp\left[-\left(\frac{C}{k_B T}\right)^{\frac{(p+1)}{(p+4)}}\right] . \qquad (3.11)$$

So, when the density of states obeys Equation (3.3), the temperature exponent α will be:

$$\alpha = \frac{p+1}{p+4} \ . \qquad (3.12)$$

Mott's original formula is obtained when $p = 0$. Cases of $\alpha = \frac{1}{2}$ are known to exist (Ab75). These may be the result of a density of states that is parabolic with $p = 2$ in Equation (3.3).

2. Ion-Track Model For High Energy Ion Modification of the Electrical Properties of Matierials

As high energy ions penetrate a medium, they cause excited electrons to be ejected along their path. These secondary electrons (also called δ electrons) give rise to a deposited energy density e ($eV/\text{Å}^3$) as they interact with the local region surrounding surrounds the ion-track. In this model, a portion of the amorphous carbon medium is affected when the deposited energy density exceeds some level. The theory behind the model was originally developed by Robert Katz in the early 1970's (Ka78). Katz's theory of radiation damage was adopted by Hedin et al. as a model for ion-induced desorption of labile biomolecules (He85). The Hedin model is applied here to explain the ion *energy* dependence of the modification process of the conductivity in amorphous carbon. The model makes the approximation that each member in the swarm of secondary electrons has the same stopping power

ϵ_o ($eV/\text{Å}$). This approximation affords the luxury of not having to worry about the distribution of electron energies. This means that the deposited energy density is nearly proportional to the number of δ electrons that have passed through a given location. An area one Ångstrom on a side will be in a region of deposited energy density e when e/ϵ_o electrons have passed through. If the region has volume L^3, then the average number of δ electrons to hit that region is:

$$\lambda = L^2 e/\epsilon_o \ . \tag{3.13}$$

The region will be affected by the δ electrons if the number λ exceeds some threshold m. Using Poisson statistics, the probability of hitting the region k times is:

$$p_k(\lambda) = \frac{\lambda^k e^{-\lambda}}{k!} \ . \tag{3.14}$$

The probability that the region will be hit by m or more δ electrons is the sum:

$$P(m,\lambda) = \sum_{k=m}^{\infty} \frac{\lambda^k e^{-\lambda}}{k!} \ . \tag{3.15}$$

The overall cross section σ_H for affecting the medium around the ion track is given by integration of $P(m,\lambda)$:

$$\sigma_H = \int_0^{\infty} 2\pi C(r) P(m,\lambda(r)) r dr \ . \tag{3.16}$$

The deposited energy density is radially symmetric about the track core and the factor $C(r)$ is used to account for the destructive effects of the high energy ion at the core of the track:

$$C(r) = \begin{cases} 0, & r < r_d \\ 1, & r \geq r_d \end{cases} , \tag{3.17}$$

where r_d is the radius of destruction. The extent of the integration is only to the farthest expected δ electron penetration. This range ζ is proportional to the kinetic energy per amu (v^2) of the ion and inversely proportional to the density ρ of the medium (Ko68):

$$\zeta = \frac{3.9 \times 10^5}{\rho}\left(\frac{v}{c}\right)^2 \mathring{A}\ , \tag{3.18}$$

where the density is in g/cm^3. The δ electron stopping power ϵ_o is proportional to the density and may be approximated by (Ko68):

$$\epsilon_o \simeq \frac{\rho}{0.991}\ eV/\mathring{A}\ . \tag{3.19}$$

The deposited energy density drops off with distance from the track. The distribution goes as $1/r^2$ until $r = \zeta$, where for the present purpose it goes to zero (Ka78).

The source of the deposited energy density is the ion stopping power dE/dx shown in Figure 3.1 for chlorine ions bombarding carbon (No70). About 50% of that energy is converted into δ electrons. Considering a disk of thickness L and radius ζ, the deposited energy density must satisfy:

$$L \int_{r_{0.5}}^{\zeta} 2\pi e(r) r dr \simeq 0.5\left(\frac{dE}{dx}\right) L\ . \tag{3.20}$$

Since $e(r)$ goes as $1/r^2$,

$$e(r) = \begin{cases} \dfrac{0.5\left(\frac{dE}{dx}\right)}{2\pi \ln\left(\frac{\zeta}{r_{0.5}}\right) r^2}, & r_{0.5} < r < \zeta \\ 0, & r > \zeta \end{cases}\ . \tag{3.21}$$

The expression for $e(r)$ is to be inserted into Equation (3.13). Then $\lambda(r)$ is to be inserted into Equation (3.15). This gives a $P(m,\lambda(r))$ which can be integrated as in Equation (3.16) to give the cross section σ_H. However, the rapidly changing functional form of the integrand and the possibility that L is large suggest that $e(r)$ be averaged over the extent of the region L^3. The averaged result for $e(r)$ is denoted by $\bar{e}(r)$ and takes the form:

$$\bar{e}(r) = \begin{cases} \dfrac{0.5\left(\frac{dE}{dx}\right)}{2\pi \ln\left(\frac{\zeta}{r_{0.5}}\right) rL} \ln\left(\frac{r+\frac{1}{2}L}{r-\frac{1}{2}L}\right), & r_{0.5} < r < \zeta \\ 0, & r > \zeta \end{cases}\ . \tag{3.22}$$

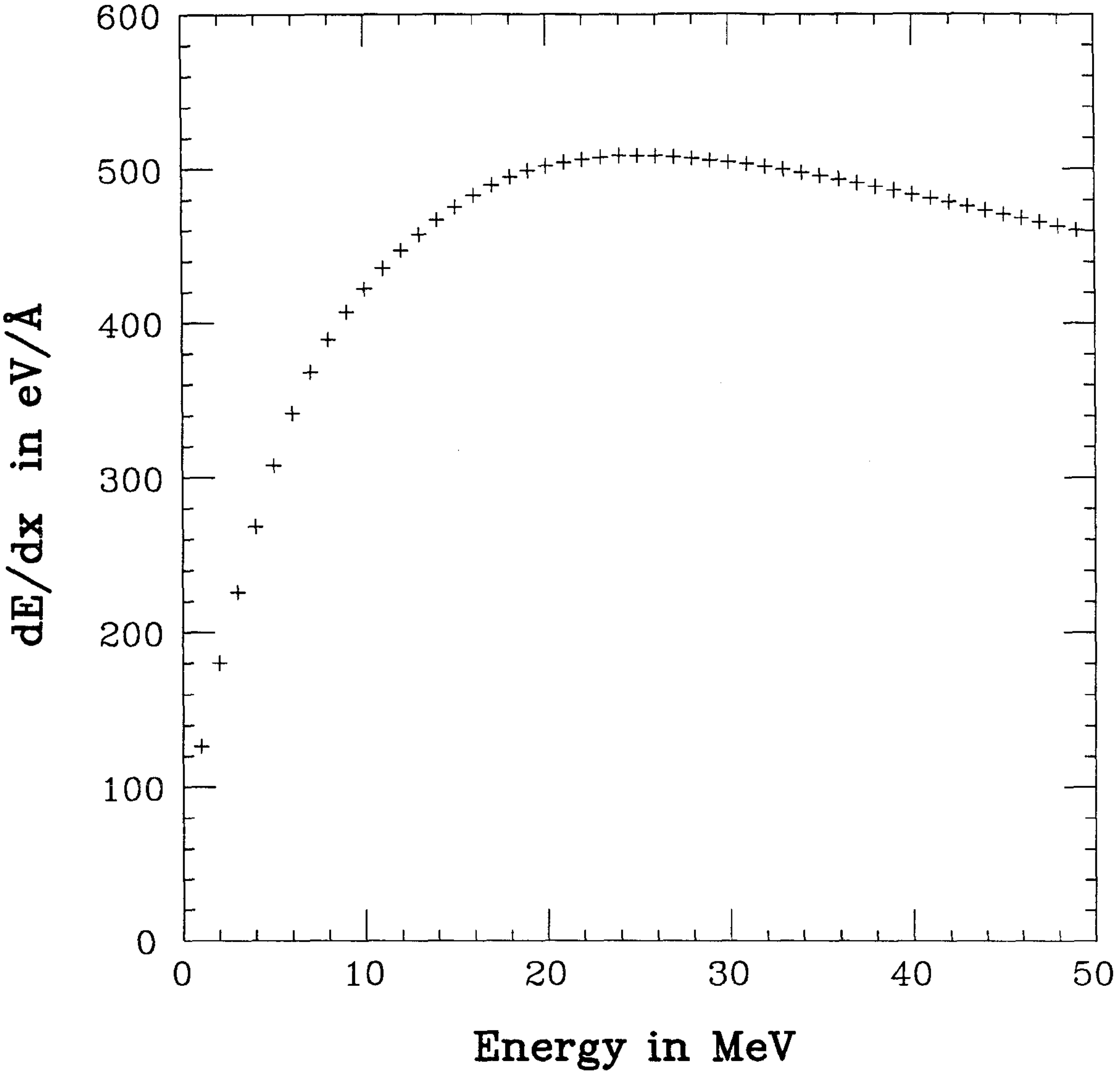

Figure 3.1

Electronic stopping power for chlorine ions in carbon of density 2.0 *grams*/*cm*^{3}. *The curve was calculated by using the method of cubic splines on the data of Northcliffe and Schilling (No70).*

The difference between $\bar{e}(r)$ and $e(r)$ becomes negligible for $r \gg L$. The average number of δ electrons to hit the region is now:

$$\lambda(r) = L^2 \bar{e}(r)/\epsilon_o \ . \tag{3.23}$$

Since $\lambda = 0$ for $r > \zeta$,

$$P(m, \lambda) = 0 \qquad r > \zeta \ . \tag{3.24}$$

Equations (3.16) and (3.17) give:

$$\sigma_H = 2\pi \int_{r_d}^{r_s} P(m, \lambda) r dr + 2\pi \int_{r_s}^{\zeta} P(m, \lambda) r dr \ , \tag{3.25}$$

where the first integral uses the region-averaged energy density in Equation (3.23) and the second integral uses Equation (3.13). The radius r_s is determined by the condition that the second integral be less than one percent of the first integral. The second integral is integrated analytically. The first integral is evaluated by Simpson's Method using 40 divisions.

Typical results of Equation (3.25) are shown in Figure 3.2. The effect of increasing the number of hits needed to affect the L^3 region is to decrease and sharpen the excitation curve. The cross section increases approximately with the square of the region size L as shown in Figure 3.3. The effect of changing the 50% radius, $r_{0.5}$, is to move the location of the peak as shown in Figure 3.4. The peak's location seems to be independent of all the other parameters. The effect of increasing the destruction radius r_d is to reduce the cross section σ_H as shown in Figure 3.5.

The intended application of these calculations is to compare curves such as those in Figures 3.2, 3.3, 3.4, and 3.5 with experimentally determined cross sections. Adjustments will be made to determine the size of the affected regions and the number of δ electron hits needed to produce the effect.

The dE/dx stopping-power data of Northcliffe and Schilling represents only the electronic stopping power. The lower energy ions will also be

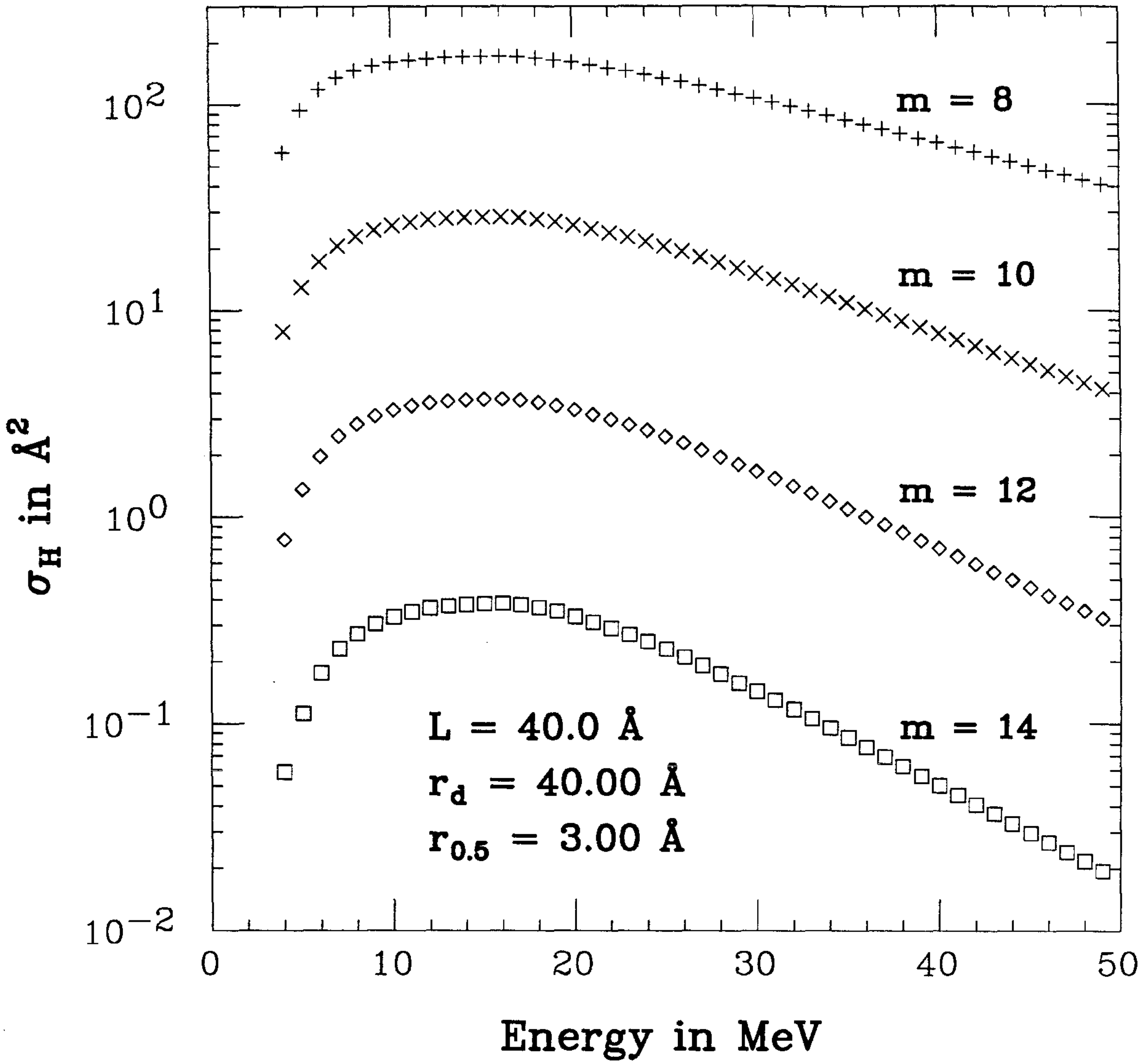

Figure 3.2

Typical cross sections for the Hedin model. For all four curves the region size is $40\AA$*, the track radius of destruction is* $40\AA$*, and the track radius for* 50% *of ion energy deposition is* $3\AA$*. The four curves show the effect of requiring an increasing number of hits* m *in the* L^3 *region.*

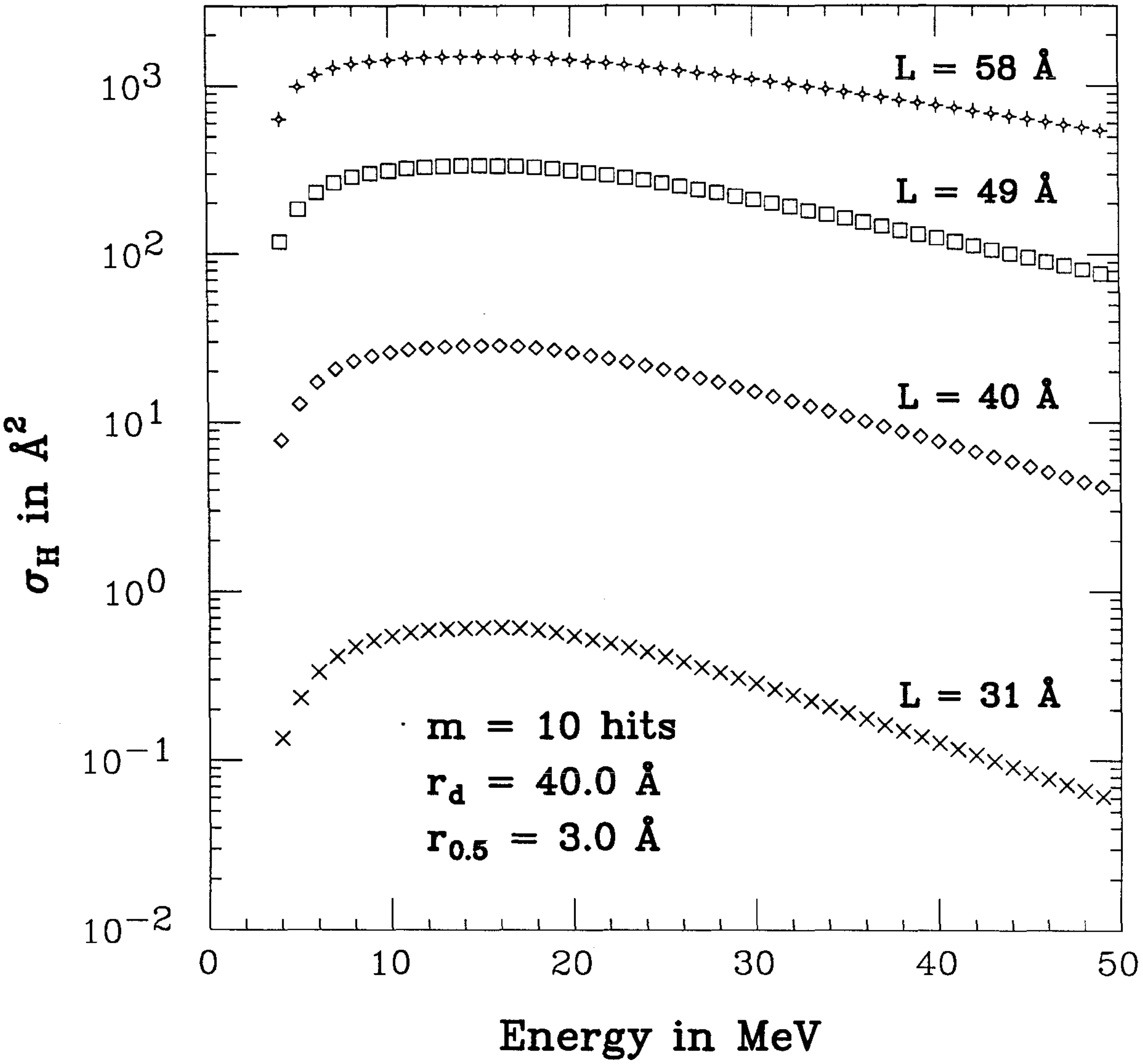

Figure 3.3

Typical cross sections for the Hedin model. For all four curves the required number of hits in the L^3 *region is 10, the track radius of destruction is* $40\AA$*, and the track radius for* 50% *of ion energy deposition is* $3\AA$*. The four curves show the effect of changing the size of the affected region.*

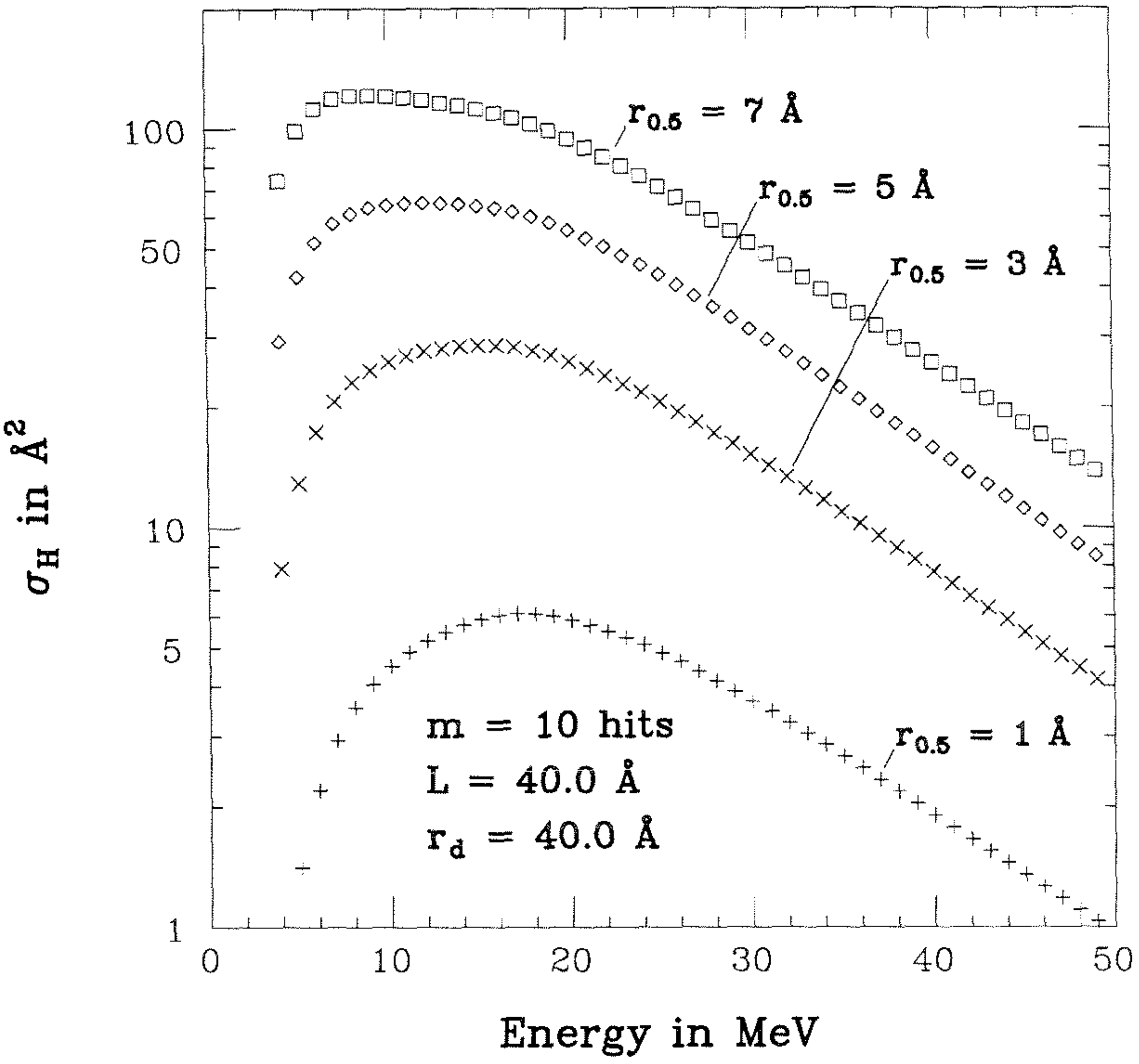

Figure 3.4

Typical cross sections for the Hedin model. For all four curves the required number of hits in the L^3 *region is 10, the size of the affected region is* 40Å, *and the track radius of destruction is* 40Å. *The four curves show the effect of changing the track radius for the* 50% *of ion energy deposition.*

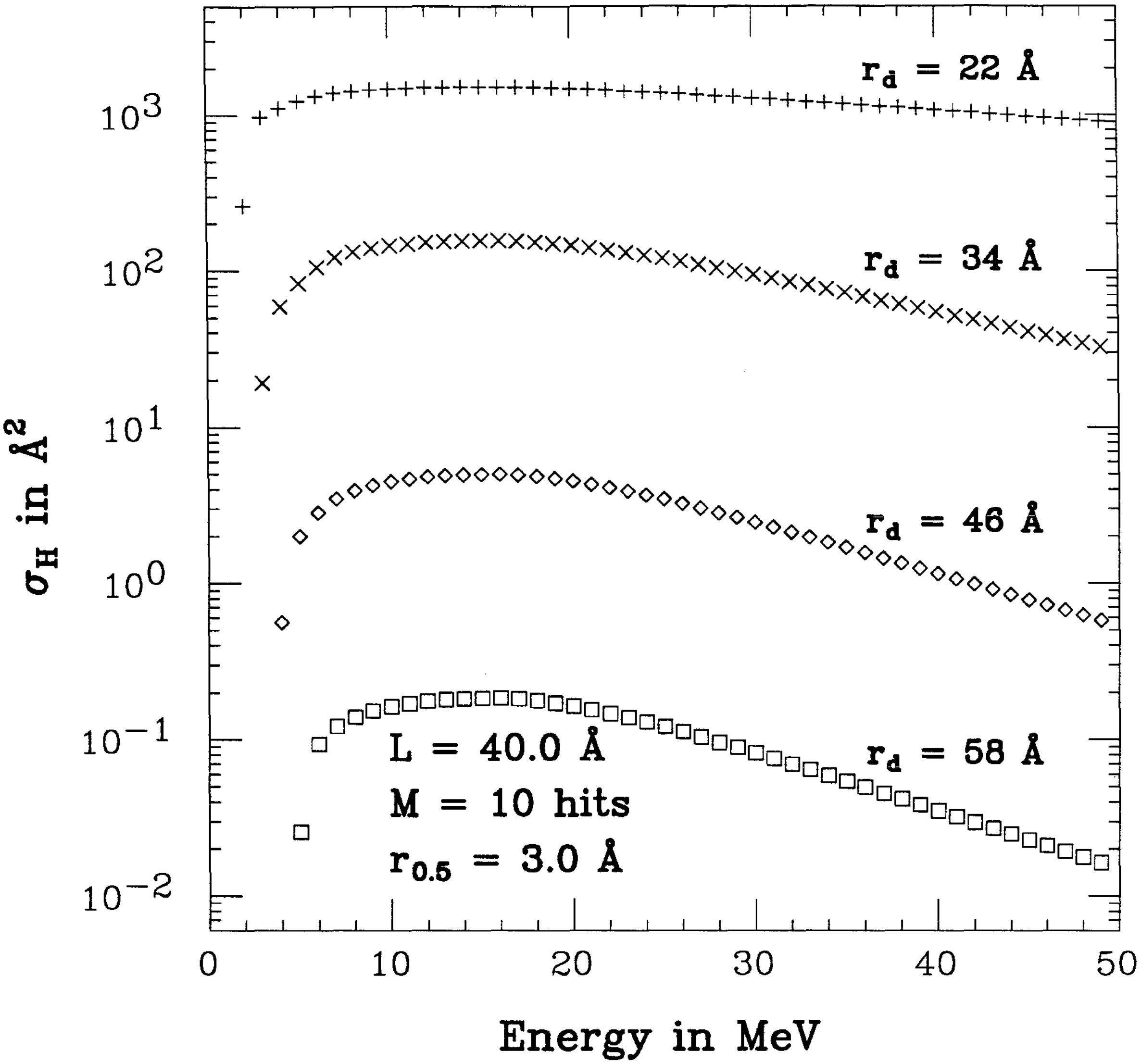

Figure 3.5

Typical cross sections for the Hedin model. For all four curves the region size is $40\AA$*, the required number of hits in the* L^3 *region is 10, and the track radius for* 50% *of ion energy deposition is* $3\AA$*. The four curves show the effect of allowing different track radii of destruction.*

slowed by nuclear stopping. Figure 3.6 shows how and where the nuclear stopping power dominates the electron stopping power (We89). The experiment of Venkatesan et al. demonstrated the effect of nuclear stopping (Ve85). Their low energy ions caused the conductivity to decrease with dose. The lowering effect of the nuclear stopping may be present to a limited degree in the 1 and 2 MeV irradiations of this work.

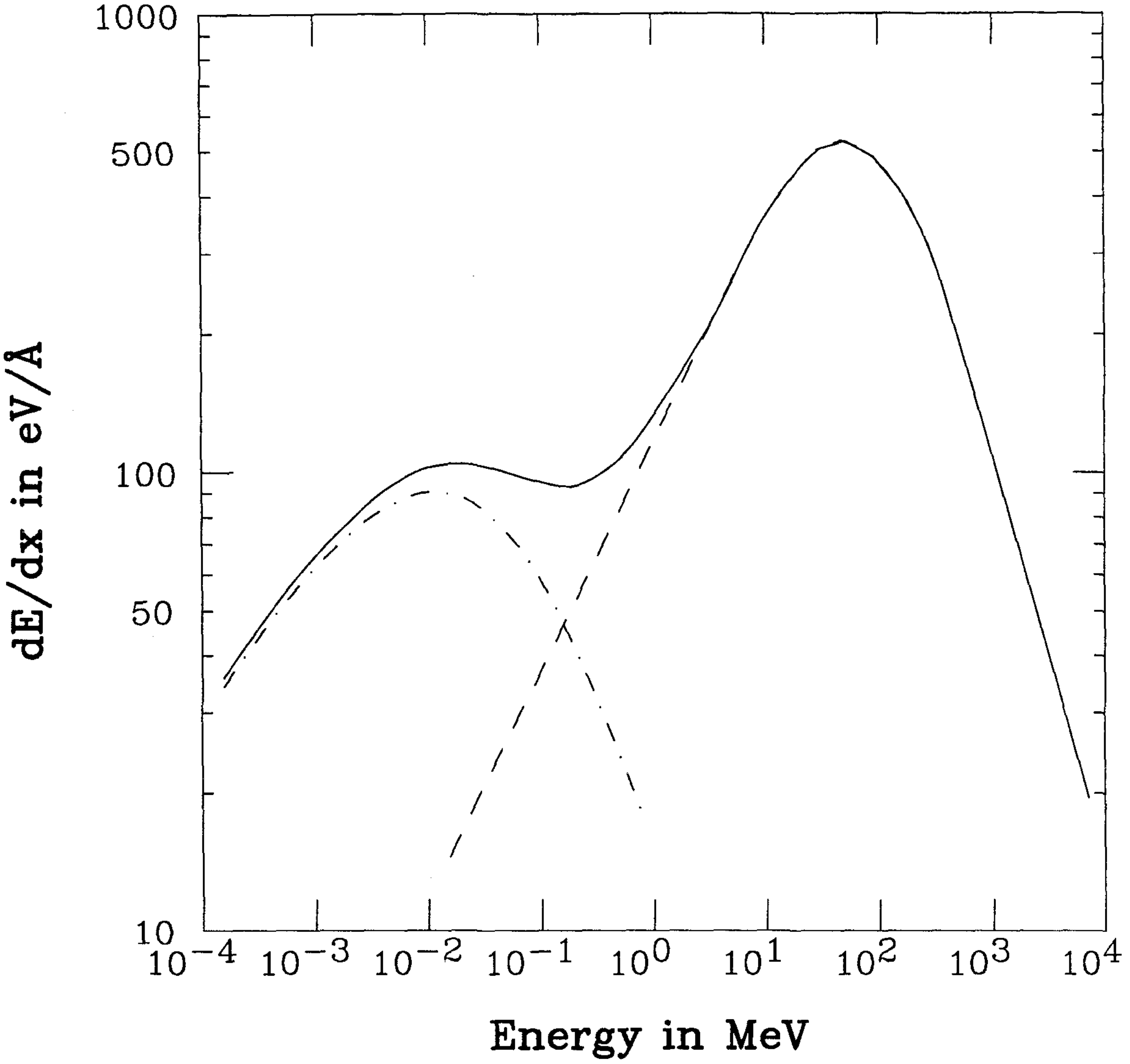

Figure 3.6

Total ion stopping power for chlorine ions in carbon of density $2.0 g/cm^3$. *This curve includes the very low and very high energy stopping powers. The dashed curve is the electronic stopping power, while the dot-dashed curve is the nuclear stopping power. Their sum is the solid curve. The contribution of the nuclear stopping is negligible for energies above* $\sim 3MeV$. *It dominates, however, in the* keV *range.*

IV. ANALYSIS

> *"The description of track structure, and of radiation effects is not simple, it is not separable, it is not linear and it certainly does not lend itself to additive or multiplicative correction factors."*
>
> *Robert Katz*

1. Setting Up Conductivity vs. Dose Curves

Four-point probe voltages and current information taken at sequential ion beam doses were entered into a computer database. Additional sample geometrical information was included with each data set. The voltages and currents were converted into conductivities as described in Appendix A. Each of the resulting curves of conductivity versus dose begins at zero dose with the pristine film conductivity. This can be between 0.03 $(\Omega cm)^{-1}$ and 0.12 $(\Omega cm)^{-1}$, depending on the thermal conditions of the film at the time it was evaporated in Arizona. Some of the data sets include very high doses, which take the film's conductivity near a saturation level of $\sim$300 $(\Omega cm)^{-1}$.

It was recognized early in the experiment that all of the samples seemed to be heading toward the same level of saturation, which was independent of the energy of the bombarding ion. This cannot be said to hold exactly because actual saturation levels were not achieved. However, the data show a general trend at high doses. It is possible to project what the saturation conductivity will be based on the data leading up to it. The projected σ_{sat} for several ion energies are shown in Figure 4.1. Since no trend is apparent for σ_{sat} vs. E, it will be considered essentially constant. The item that changes with ion energy is the efficiency by which σ_{sat} is reached.

Most of the data sets stop short of the onset of saturation. The samples bombarded with ion energies between 8 MeV and 20 MeV approach saturation faster than the lower or higher energy targets. Figures 4.2, 4.3,

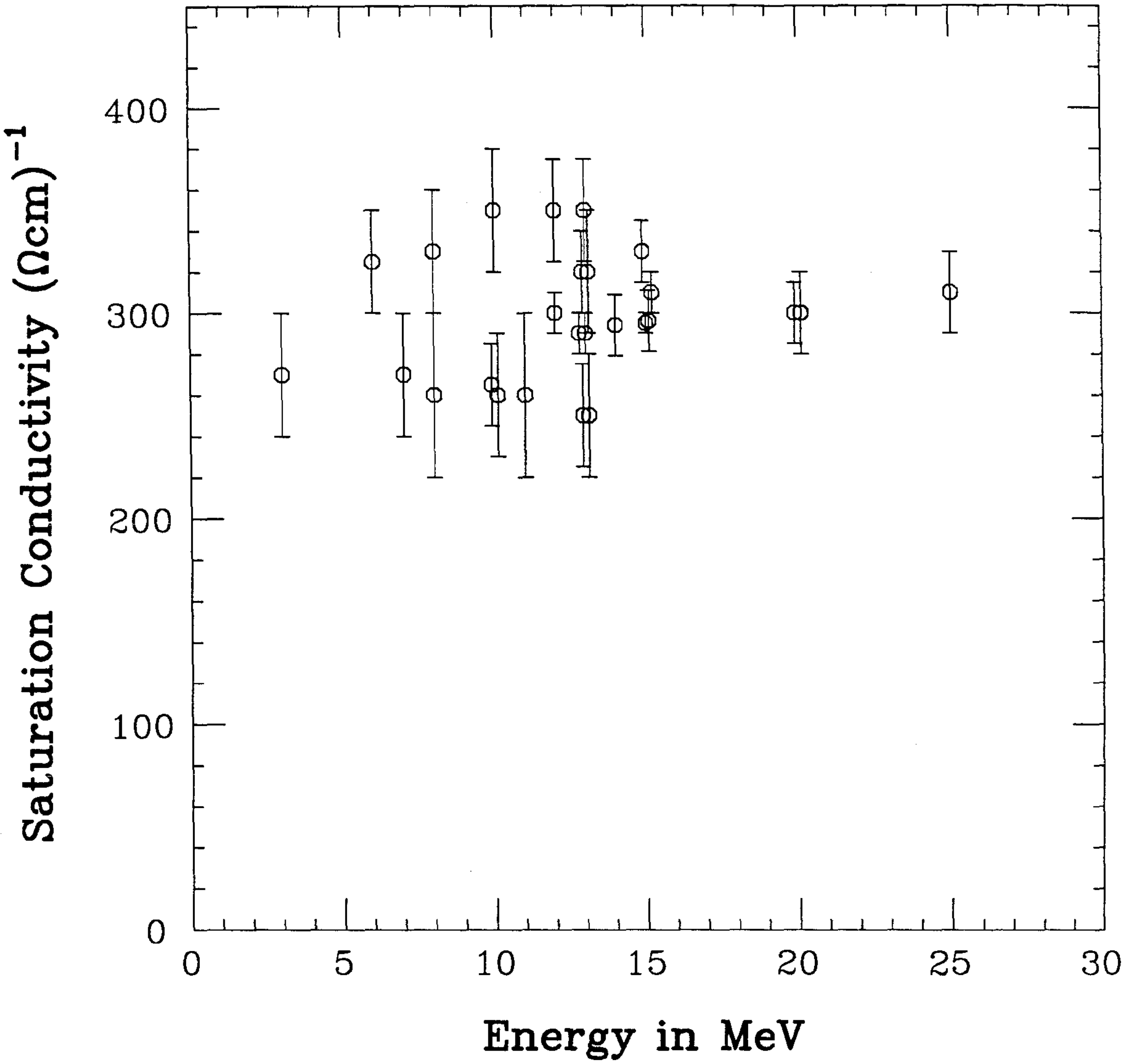

Figure 4.1

The saturation conductivity is the highest conductivity that would be achieved by irradiation with chlorine ions of a given energy. These data indicate that σ_{sat} is probably independent of ion energy (in the MeV range of this work). Data points at 10, 13, 15, and 20 MeV are slightly displaced to prevent eclipsing.

and 4.4 show conductivity versus dose data for three ranges of incident ion energy. The conductivities are plotted in the form $\sigma - \sigma_{pristine}$ to show the change from the pristine state.

The uncertainty in the conductivities is taken to be 1% because of target heating by the ion beam. Voltage readings were taken as soon as possible after each step of beam dose. The 1% uncertainty comes about because of small differences in the time needed to secure a four-point probe reading. The samples begin cooling immediately after the beam is blocked. For pristine samples, the conductivity drops about 1% per $^\circ C$:

$$\sigma = \sigma_o(1 - 0.01\ \delta T)\ . \tag{4.1}$$

This dependence diminishes with dose. The thermal time constant θ was measured to be $\sim 100\ sec$. The worst case sample heating would be $T_\delta \sim 50^\circ C$ above initial temperature (there was one sample that may have been heated by $150^\circ C$). The thermal decay is modeled as:

$$\delta T = T_\delta\left(1 - e^{-t/\theta}\right)\ . \tag{4.2}$$

For small times t:

$$\delta T \cong T_\delta \frac{t}{\theta}\ . \tag{4.3}$$

From Equation (4.1):

$$\frac{\sigma - \sigma_o}{\sigma_o} = -0.01\ T_\delta \frac{t}{\theta}\ . \tag{4.4}$$

There was an irregularity of $\delta t \sim 2$ seconds in the time to take the voltage reading. This is the time needed to apply the four-point probe, apply current, and obtain a stable voltage on the DVM. Thus, the estimate for the error in the conductivity is:

$$\left|\frac{d\sigma}{\sigma}\right| = \left|0.01\ T_\delta \frac{\delta t}{\theta}\right| = 0.01\ . \tag{4.5}$$

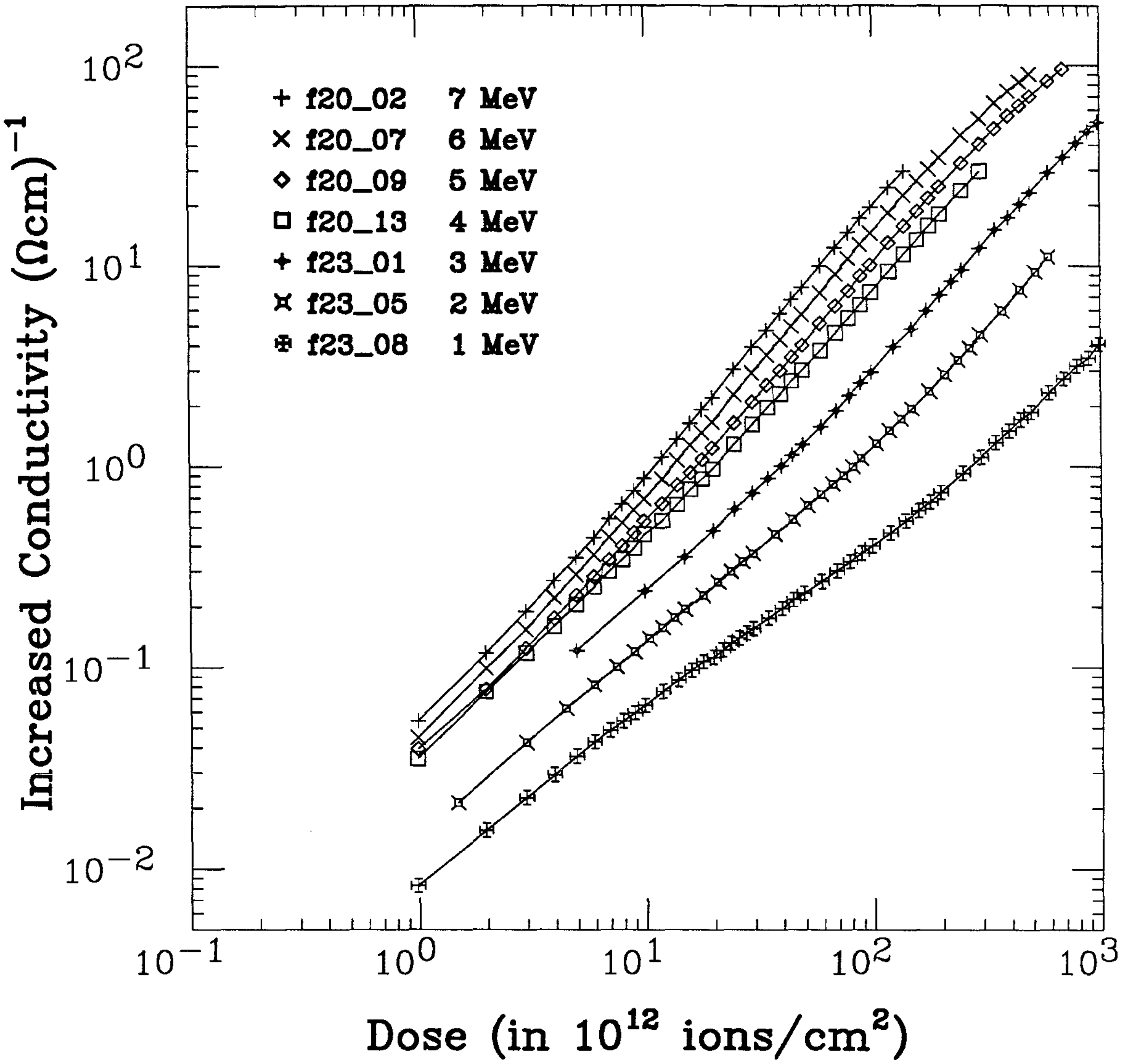

Figure 4.2

Change in conductivity, $\sigma - \sigma_{pristine}$*, for 1 to 7 MeV irradiations. These curves show that the 7 MeV ions are about 10 times more effective than the 1 MeV ions at changing the sample conductivity. The 1, 2, and perhaps 3 MeV curves show a somewhat different shape from those of the higher energies.*

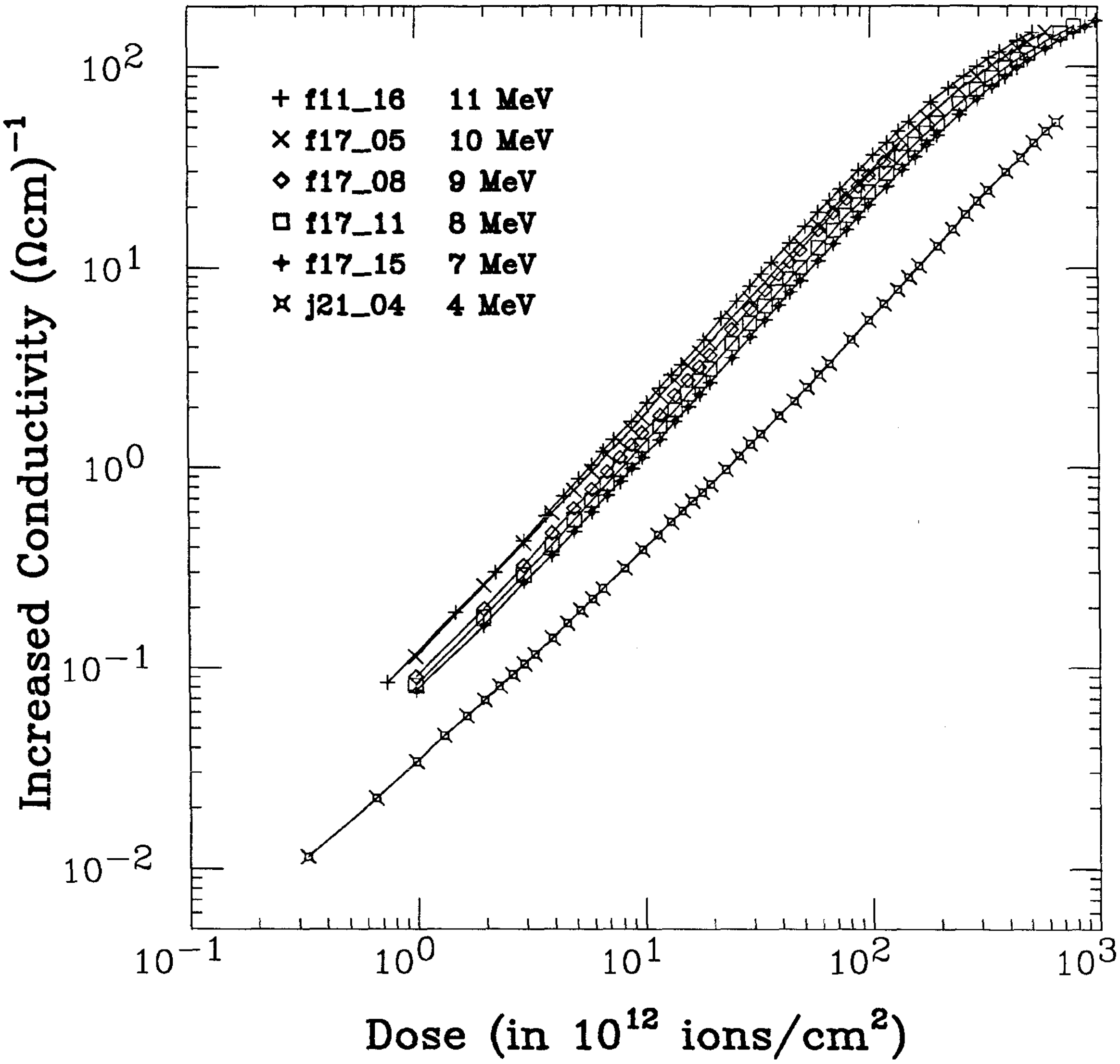

Figure 4.3

Change in conductivity, $\sigma - \sigma_{pristine}$, for 4 to 11 MeV irradiations. The 9 and 10 MeV curves are very close to each other. The data curves for 11, 12, and 13 MeV irradiations would be at about the same place as the 9 and 10 MeV curves. These energies are all about equally effective.

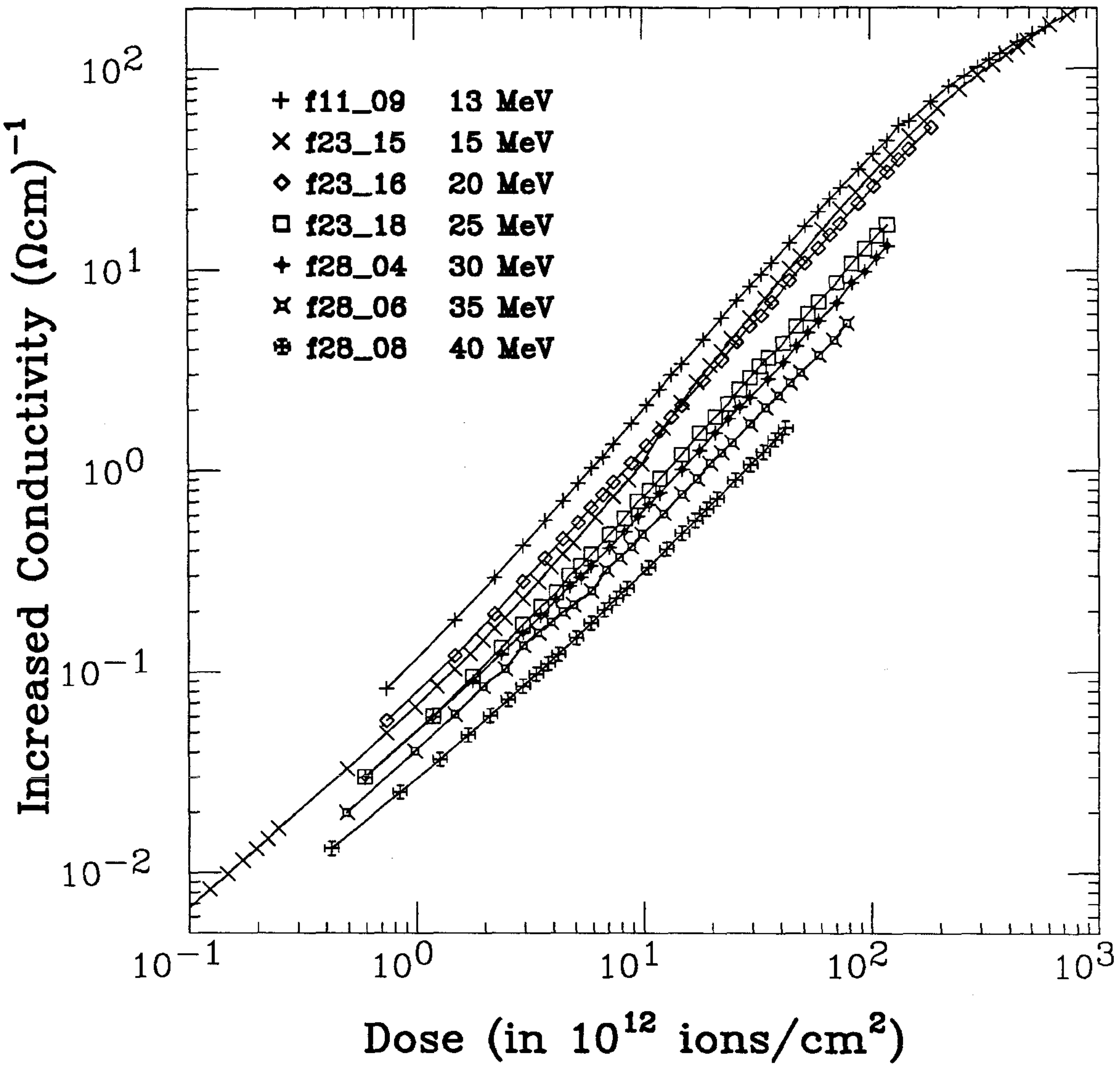

Figure 4.4

Change in conductivity, $\sigma - \sigma_{pristine}$, *for 13 to 40 MeV irradiations. These curves show than the 40 MeV ions are less effective than the lower energy 13 MeV ions at inducing increased conductivity. These high energy ions are still much more effective than the 1 MeV ions represented in Figure 4.2.*

2. Thermal Modeling of Targets

A two-step thermal model was used to simulate the target temperature during the data taking. Energy input came via the energetic ions stopping in the glass substrate. The first step of heat loss was by conduction to the brass slab. The second step consists of heat conduction from the brass slab to the large aluminum target holder through the 0.5 *cm* thick plexiglas slab. This additional step was introduced to account for the possibility that the brass slab may be getting very warm by the end of a long irradiation. This would have an effect on the amount of heat transported away from the even warmer glass target substrate.

A more detailed 3-dimensional treatment of the thermal problem could be used; however, the improvements would not be worth the additional complication. The goal was to provide a rough accounting of target heating by the ion beam.

The model makes use of the following definitions:

$\phi_i =$ cumulative dose after i steps;

$A =$ area of bombarded region;

$T_{io} =$ initial target temperature at step number i;

$E =$ bombarding ion energy;

$i_o =$ ion beam current;

$Q =$ absolute value of incident ion charge;

$C_p =$ heat capacity of target region;

$T_H =$ temperature of brass slab;

$\kappa =$ conductivity of heat away from the target to the brass slab;

$t_i =$ bombarding time;

$$t_i = \frac{AQ(\phi_i - \phi_{i-1})}{i_o} \ . \tag{4.6}$$

The temperature of the target at the end of the i^{th} step at the instant of stopping the beam is:

$$T_i = T_{io} + \left[\frac{E_{io}}{QC_p\kappa} - (T_{io} - T_H)\right](1 - e^{-\kappa t_i}) \ . \tag{4.7}$$

The temperature drops when the beam is cut. At time t_r after the beam is cut,

$$T_i(t_r) = T_i - (T_i - T_H)(1 - e^{-\kappa t_r}) \ . \tag{4.8}$$

This is the temperature of the target when the four-point probe voltage is read. At time $t_r + t_w$ the next dose step begins. The temperature is given by Equation (4.8):

$$T_{i+1\ o} = T_i(t_r + t_w) \ . \tag{4.9}$$

This temperature is used with Equation (4.7) while changing subscripts from i to $i+1$ to begin the next cycle.

To account for brass slab heating, an analogous sequence of steps is employed to map the slab temperature T_H step by step.

3. Investigation of Mott Conductivity

The effect of beam heating was not anticipated. The slow rise in probe voltage was a nagging reminder that even the most fundamental experiment is not simple. What was causing the voltage to drift away in an exponential decay? Depending on circumstances, the amount of drift could be from 1% to 30%.

It was not an *RC* time-constant problem because the drift persisted without probe contact.

The other obvious cause was ion beam heating of the target. By how much does the temperature change? How sensitive is the conductivity to temperature? The Mott formula shown in Equation (3.1) does not give $\frac{d\sigma}{dT}$ until the factor C is known.

A reconfigured target holder carried a captive Chromel-Alumel thermocouple junction and a 50 Watt heating block. Torrseal adhesive fused the thermocouple onto a typical glass substrate. The thermocouple voltage appeared on a sensitive DVM. The target was arranged in the hope that maybe direct irradiation of the thermocouple probe will cause a detectible increase in the temperature of the small gob of Torrseal. There was a strong effect. The $20nA$ beam of 15 MeV Cl^{4+} ions caused an immediate rise in temperature that lasted as long as the beam fell on the thermocouple. Starting and stopping the beam caused the indicated temperature to rise and fall with negligible delay. A strip-chart recording showed that the temperature obeyed Equations (4.2), (4.3), and (4.4). The time constant was $\sim$ 140 *seconds*. The indicated heat capacity of the Torrseal + thermocouple + glass substrate was $\sim 0.2\ J/{}^{\circ}C$. A larger value would be expected for the whole piece of glass. This suggests that the beam heating is restricted to an immediate locale around the irradiated region. The heat is transported to the brass slab faster than to the farther portions of the glass substrate.

This experiment was not yet over. Several samples received various doses by the same ion beam. One pristine sample was not subjected to irradiation. The heating block supplied a steady 25 *Watts* (50% *power*) to the entire target assembly. The temperature made a slow climb to $\sim 70^{\circ}C$. Meanwhile, the pristine and irradiated samples all showed continuously changing conductivities. The pristine sample changed the most. The most heavily irradiated sample was nearly insensitive to its thermal environment. The conductivities versus temperature are shown in Figure 4.5. The uncertainty in the data and the narrow range of temperature covered prohibit making a definitive choice for the exponent α in Equation (3.1).

In a separate experiment, pristine and irradiated samples (using 15 MeV Cl^{4+}) were cooled to near liquid-nitrogen temperatures. Their conductivities were monitored by directly measuring the resistance R of the carbon film between two evaporated silver pads. The conductivity is then:

$$\sigma = \frac{b}{R\tau w} , \tag{4.10}$$

where τ is the film thickness, w the sample width, and b is the distance between the conducting pads. The data from three pristine and three irradiated samples show that the exponent α is not constant. It starts out at $\frac{1}{2}$ for the pristine samples and changes over to $\frac{1}{4}$ for those that were irradiated. Conductivity is plotted versus $T^{-\frac{1}{2}}$ for one pristine sample in Figure 4.6. Another sample, bombarded with 15 MeV Cl^{4+} ions to a moderate dose of 1.87×10^{12} $\frac{ions}{cm^2}$, has its conductivity plotted versus $T^{-\frac{1}{4}}$ in Figure 4.7.

The relative temperature dependence of the conductivity is according to Equation (3.1):

$$\frac{T}{\alpha}\frac{d\sigma}{dT} = \alpha\left(\frac{C}{k_B T}\right)^{\alpha} . \tag{4.11}$$

It is presented in Table II for several samples including those of Figures 4.5, 4.6, and 4.7. Taking $\alpha = \frac{1}{2}$ for the pristine samples, $297°K$ for the room temperature, and 3.745 for the average pristine relative temperature dependence, gives $C = 1.4387eV$. The exponent α, which changes over to $\alpha \sim\frac{1}{4}$, is given by solving (at room temperature)

$$\frac{T}{\alpha}\frac{d\sigma}{dT} = \alpha\left(\frac{1.4387eV}{k_B T}\right)^{\alpha} \tag{4.12}$$

for each relative temperature dependence. Denoted by $\alpha(\phi)$, these are also shown in Table II and plotted versus dose in Figure 4.8. The 15 MeV data

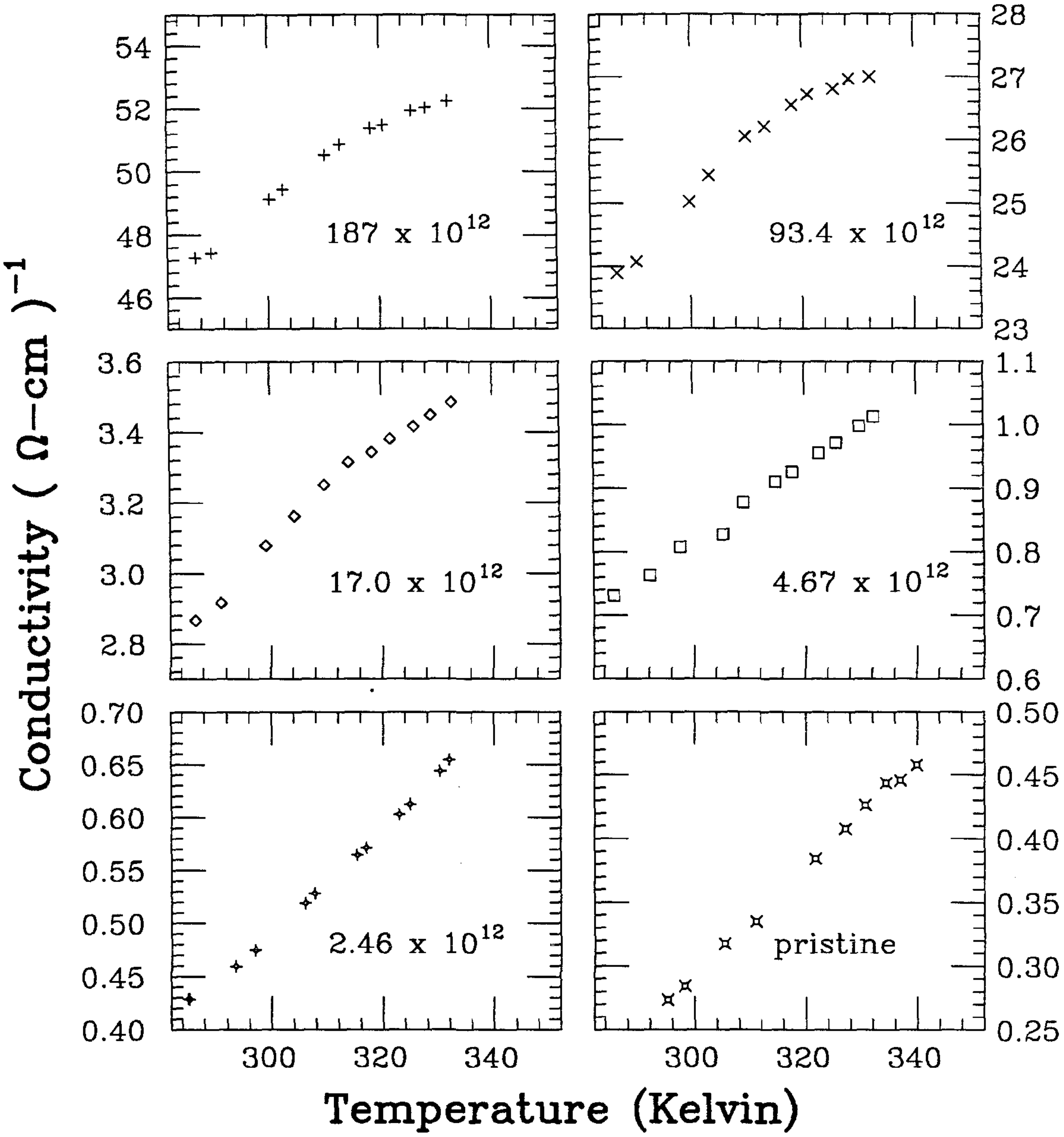

Figure 4.5

Plots of conductivity versus sample temperature at various doses. The number by each curve is the dose of 15 MeV Cl^{4+} $\frac{ions}{cm^2}$ *delivered to the sample at an earlier time. The pristine sample is the most sensitive to changes in temperature. Its conductivity nearly doubles over the range shown.*

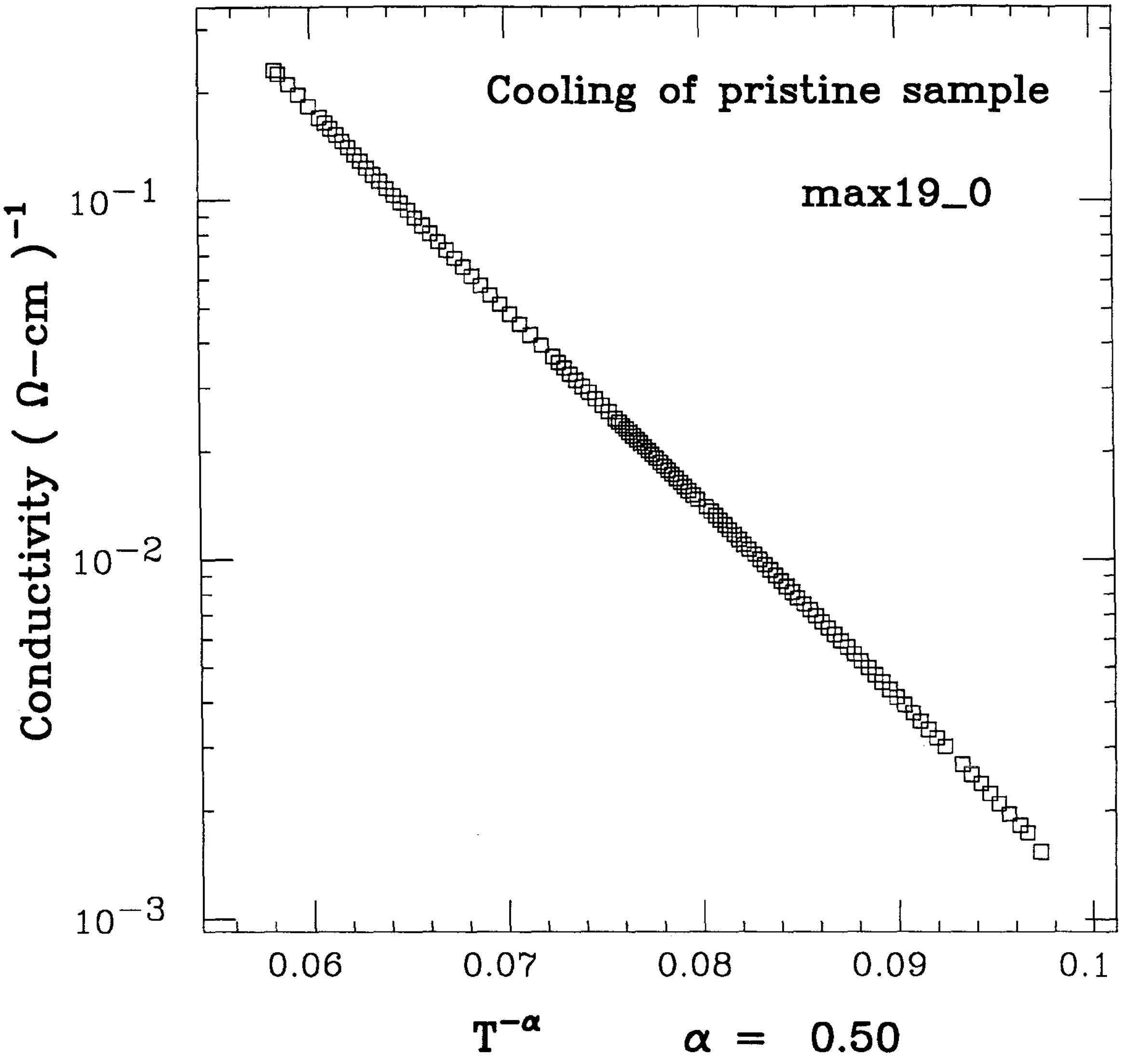

Figure 4.6

Sample conductivity plotted on a logarithmic scale versus an exponentiated temperature. The $\alpha = \frac{1}{2}$ *gives the best straight-line fit for pristine samples. The temperature is measured in* $^\circ K$. *The lowest temperature achieved was* $105.6^\circ K$.

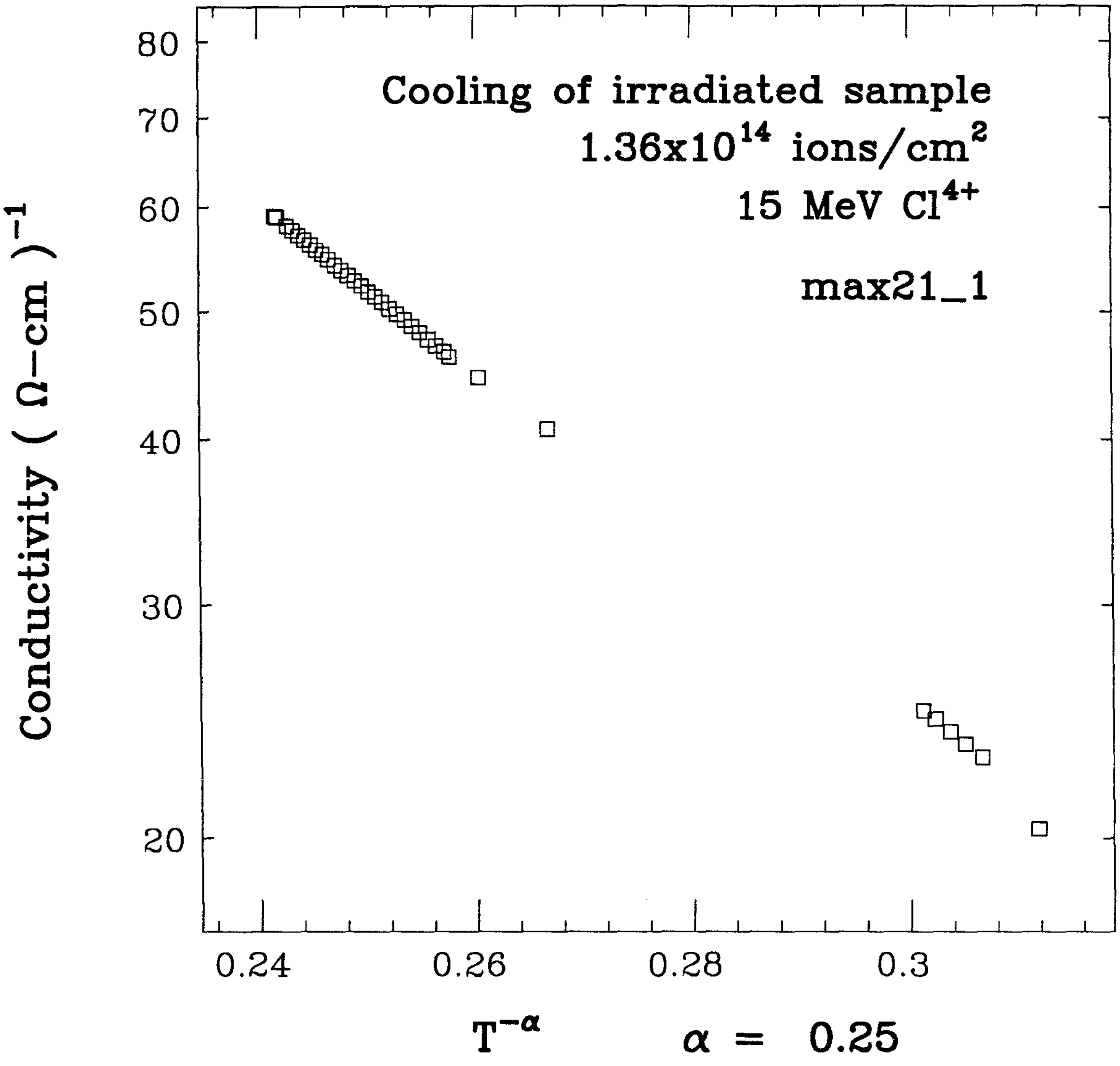

Figure 4.7

Sample conductivity plotted on a logarithmic scale versus an exponentiated temperature. This sample was pre-irradiated with 15 MeV Cl^{4+} *ions to a dose of* 1.36×10^{14} $\frac{ions}{cm^2}$. *The exponent* $\alpha = \frac{1}{4}$ *gives the best straight-line fit in this case.*

TABLE II

Relative Temperature Dependence and Mott Temperature Exponent

Sample Number	Dose in 10^{12} $ions/cm^2$	Energy MeV	$\frac{T}{\sigma}\frac{d\sigma}{dT}$	$\alpha(\phi)$
Max19–0	pristine	—	$3.71^{+.04}_{-.04}$	$0.498^{+.002}_{-.002}$
Max20–0	pristine	—	$3.67^{+.01}_{-.10}$	$0.497^{+.000}_{-.005}$
Max21–0	pristine	—	$3.64^{+.08}_{-.10}$	$0.495^{+.003}_{-.005}$
tpr1	pristine	—	$3.96^{+.08}_{-.14}$	$0.509^{+.003}_{-.006}$
Max20–1	1.05	15	$3.44^{+.02}_{-.09}$	$0.486^{+.001}_{-.004}$
ts13–01	2.46	15	$2.74^{+.11}_{-.07}$	$0.449^{+.006}_{-.004}$
ts13–02	4.67	15	$2.23^{+.06}_{-.05}$	$0.417^{+.004}_{-.003}$
Max20–2	7.7	15	$2.70^{+.03}_{-.07}$	$0.447^{+.002}_{-.004}$
ts13–03	17.	15	$1.60^{+.02}_{-.21}$	$0.366^{+.002}_{-.021}$
tf11–17	51.6	11	$1.79^{+.08}_{-.05}$	$0.383^{+.006}_{-.004}$
tf28–06	78.6	36	$2.53^{+.42}_{-.08}$	$0.436^{+.024}_{-.005}$
ts13–04	93.4	15	$1.10^{+.01}_{-.15}$	$0.312^{+.001}_{-.020}$
tf20–16	98.3	3	$3.08^{+.14}_{-.14}$	$0.468^{+.007}_{-.007}$
Max21–1	136.	15	$0.86^{+.06}_{-.07}$	$0.279^{+.009}_{-.012}$
ts13–05	187.	15	$0.83^{+.03}_{-.09}$	$0.275^{+.005}_{-.014}$
tf23–15	5160.6	15	$0.44^{+.02}_{-.02}$	$0.199^{+.004}_{-.006}$

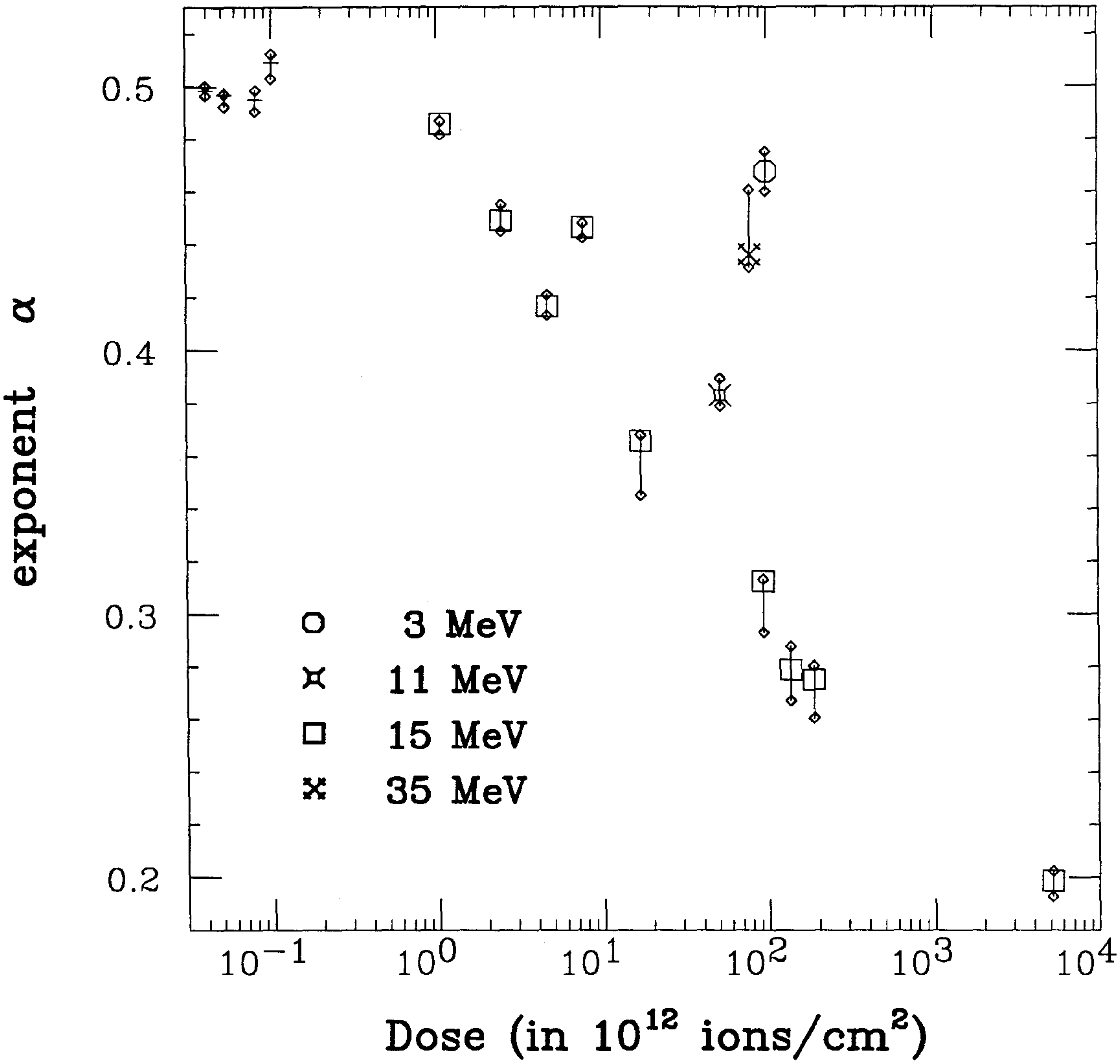

Figure 4.8

The Mott exponent α, which solves Equation 4.12, is plotted versus beam dose for various ion energies. The best-fit confidence limits are indicated by the small diamonds. All but one of the 15 MeV data points seem to fall on a sigmoidal curve. The points plotted to the left of 10^{-1} *indicate the α's for the four pristine samples.*

appear to lie on a sigmoidal curve decreasing from $\alpha = \frac{1}{2}$ to perhaps $\alpha = \frac{1}{4}$ (or less). The energies 3, 11, and 35 MeV have only one representative α each. It is likely that α behaves in a similar manner for these energies as well. The sigmoidal curve may be merely displaced along the dose axis for each different energy.

4. Correcting Beam Heating Effects

The Mott conductivity formula in Equation (3.1) is the basis of thermal corrections to the conductivity data in this work. The correction is never large. It is also never uniform or simple. If $\alpha(\phi, T)$ is the measured conductivity at dose ϕ and temperature T, then the conductivity at room temperature at that dose is:

$$\sigma(\phi, T_{RT}) = \sigma(\phi, T) \frac{\exp\left[-\left(\frac{C}{k_b T_{RT}}\right)^{\alpha}\right]}{\exp\left[-\left(\frac{C}{k_b T}\right)^{\alpha}\right]} . \tag{4.13}$$

C is $1.487 eV$ and $\alpha(\phi)$ is at least approximately understood. Also, $T = T(\phi)$ is provided by the procedure outlined in Section 4.2.

Some examples of the effect of Equation (4.13) are shown in Figures 4.9, 4.10, and 4.11. In addition to showing the uncorrected and corrected data points, the figures also show a solid continuous line. This line is a parameterization of the data. The formulation of the parameterization is given in Appendix B. Generally, the fit of the parameterization curve to the data is better than the 1% error of the data. The purpose of the parameterization curve is to guide the eye and to provide an indication of where the conductivity would be expected to go if the irradiation continued into higher dosages. Its usefulness will be more apparent in the next chapter where the derivative of conductivity with respect to dose is examined.

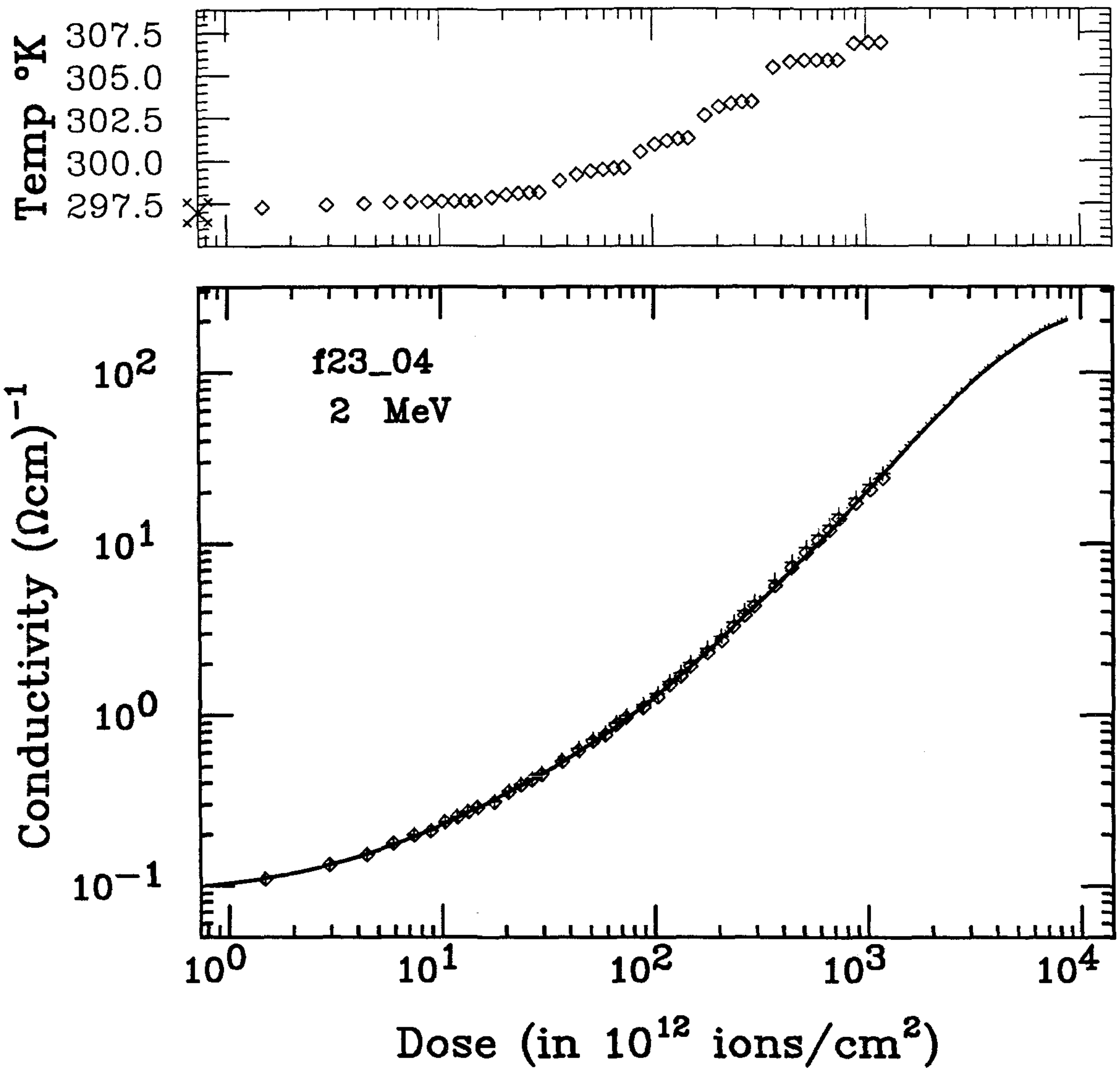

Figure 4.9

Target temperature, as predicted by the procedure outlined in Section 4.2, appears in the upper graph. The unirradiated target temperature is 297° K, *denoted by the large symbol on the left side.*

The lower graph shows the uncorrected and corrected sample conductivity. The dotted line is the uncorrected parameterized conductivity. The solid line is the corrected parameterized conductivity. The uncorrected and corrected original data are marked by plus signs and diamonds, respectively.

In this figure, the 2 MeV *ions did not cause a large increase in the target temperature, and so a very small correction to conductivity is seen.*

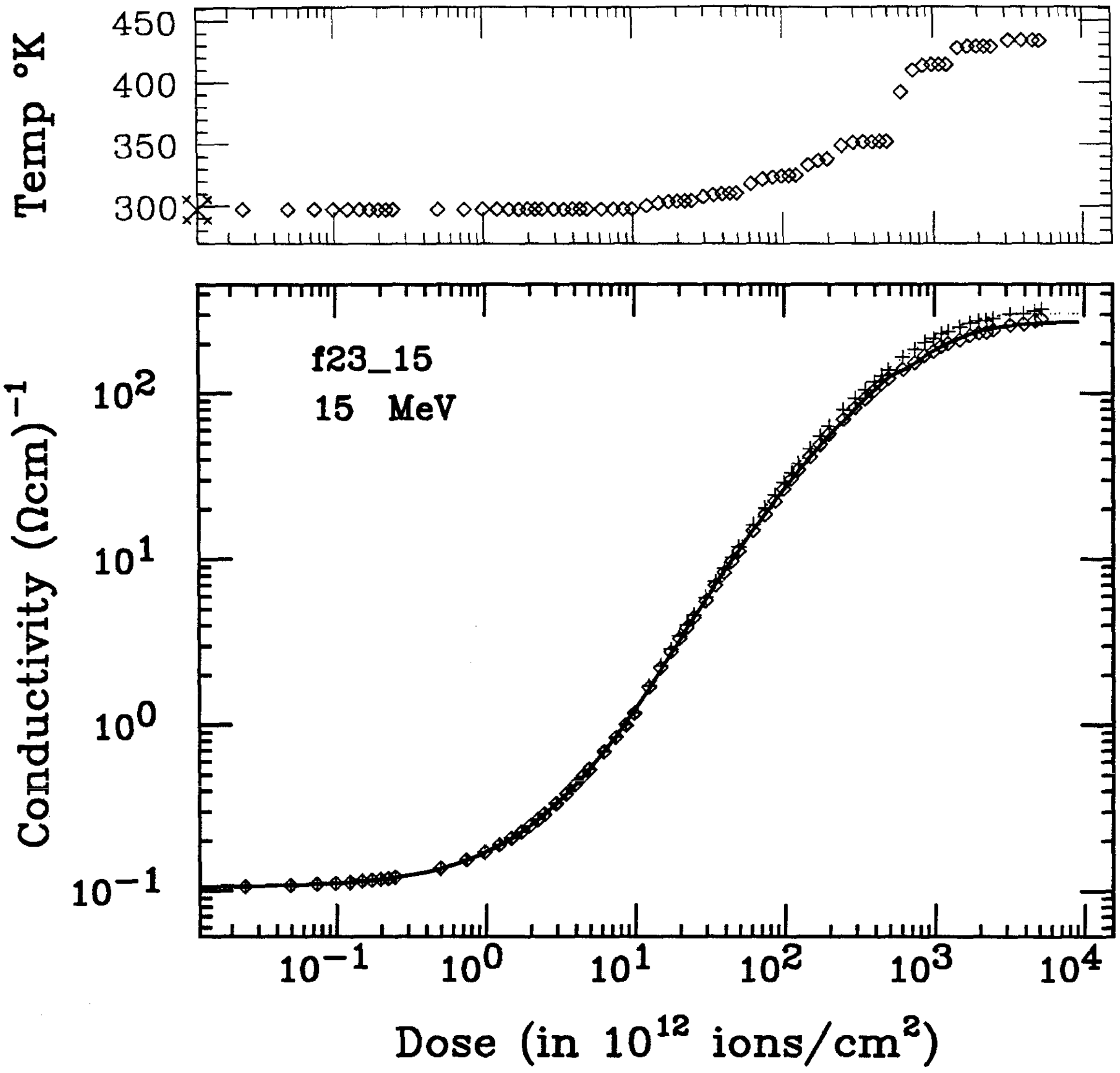

Figure 4.10

Target temperature, as predicted by the procedure outlined in Section 4.2, appears in the upper graph. The unirradiated target temperature is 297° K, *denoted by the large symbol on the left side.*

The lower graph shows the uncorrected and corrected sample conductivity. The dotted line is the uncorrected parameterized conductivity. The solid line is the corrected parameterized conductivity. The uncorrected and corrected original data are marked by plus signs and diamonds, respectively.

In this figure, very strong beam currents of 15 MeV *ions caused a large increase in target temperature. This caused the conductivity to increase by as much as* 20% *at some points during the irradiation.*

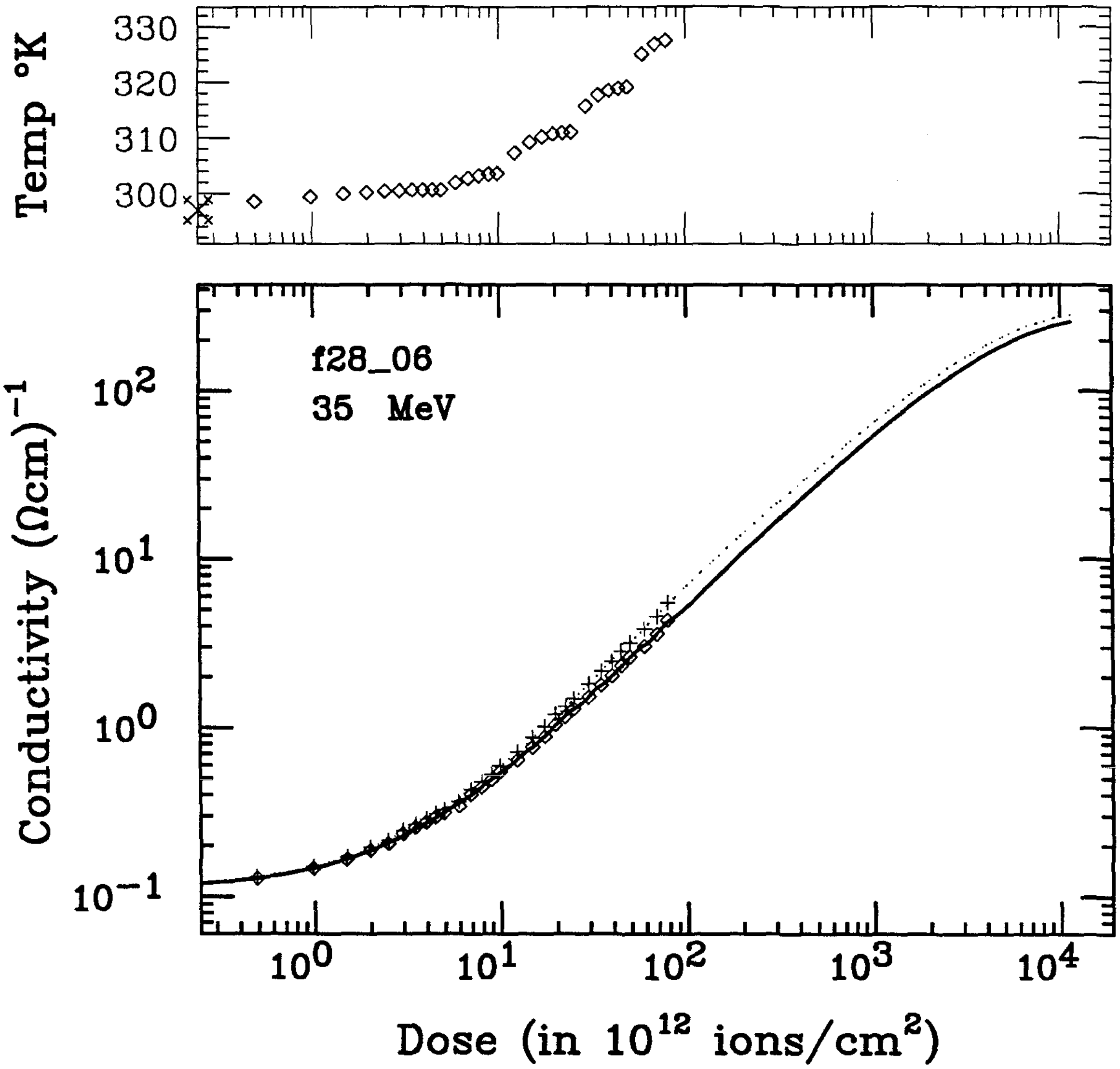

Figure 4.11

Target temperature, as predicted by the procedure outlined in Section .2, appears in the upper graph. The unirradiated target temperature is $297°K$*, denoted by the large symbol on the left side.*

The lower graph shows the uncorrected and corrected sample conductivity. The dotted line is the uncorrected parameterized conductivity. The solid line is the corrected parameterized conductivity. The uncorrected and corrected original data are marked by plus signs and diamonds, respectively.

This time, the target was moderately heated by the 35 MeV *ion beam. Since the heating occurs when the sensitivity to thermal changes is large (at low beam dose), the correction to the conductivity is large, as in Figure 4.10.*

V. RESULTS

1. A Close Look at Conductivity vs. Dose

The conductivity curves presented in Figures 4.9, 4.10, and 4.11 are plotted on a log-log basis. An interesting event is seen to take place on a typical conductivity curve when the curve is plotted linear-linear. A set of such plots is shown in Figures 5.1 to 5.7. It is clear that at first the change in conductivity is simply proportional to the ion beam dose. Each increment of ion beam exposure produces the same amount of increase in the conductivity. Then the curve begins to lift away from a strictly linear function. This departure soon heads the curve onto another linear, generally steeper, dependence on dose. And once again the conductivity increases by the same amount for each same increment of dose. Eventually, this second linearity softens as the conductivity begins to saturate in the neighborhood of 300 $(\Omega cm)^{-1}$. The example presented in the figures was a 15 MeV irradiation. The data for 1 MeV irradiations exhibit a low dose slope that is greater than the medium dose slope. Each energy of irradiation seems to produce its own unique pair of low dose and medium dose slopes. The next section examines these slopes and interprets their meaning.

2. Cross Sections for Conductivity Change

If one bombarding ion produces a change $\delta\sigma$ in conductivity then n ions should cause a change $n\delta\sigma$. That holds if n is small, say, less than 10^{10}. The reason it does not hold for all n is that the regions damaged by the ions start to overlap. Neglecting overlap for the moment, the change in conductivity is proportional to the ion dose $d\phi$. This proportionality constant must have dimensions of conductivity times area. It is related to the cross section, b, of producing change with energetic ion irradiation. If the constant is to have the correct dimensions, it must be a product of a conductivity and

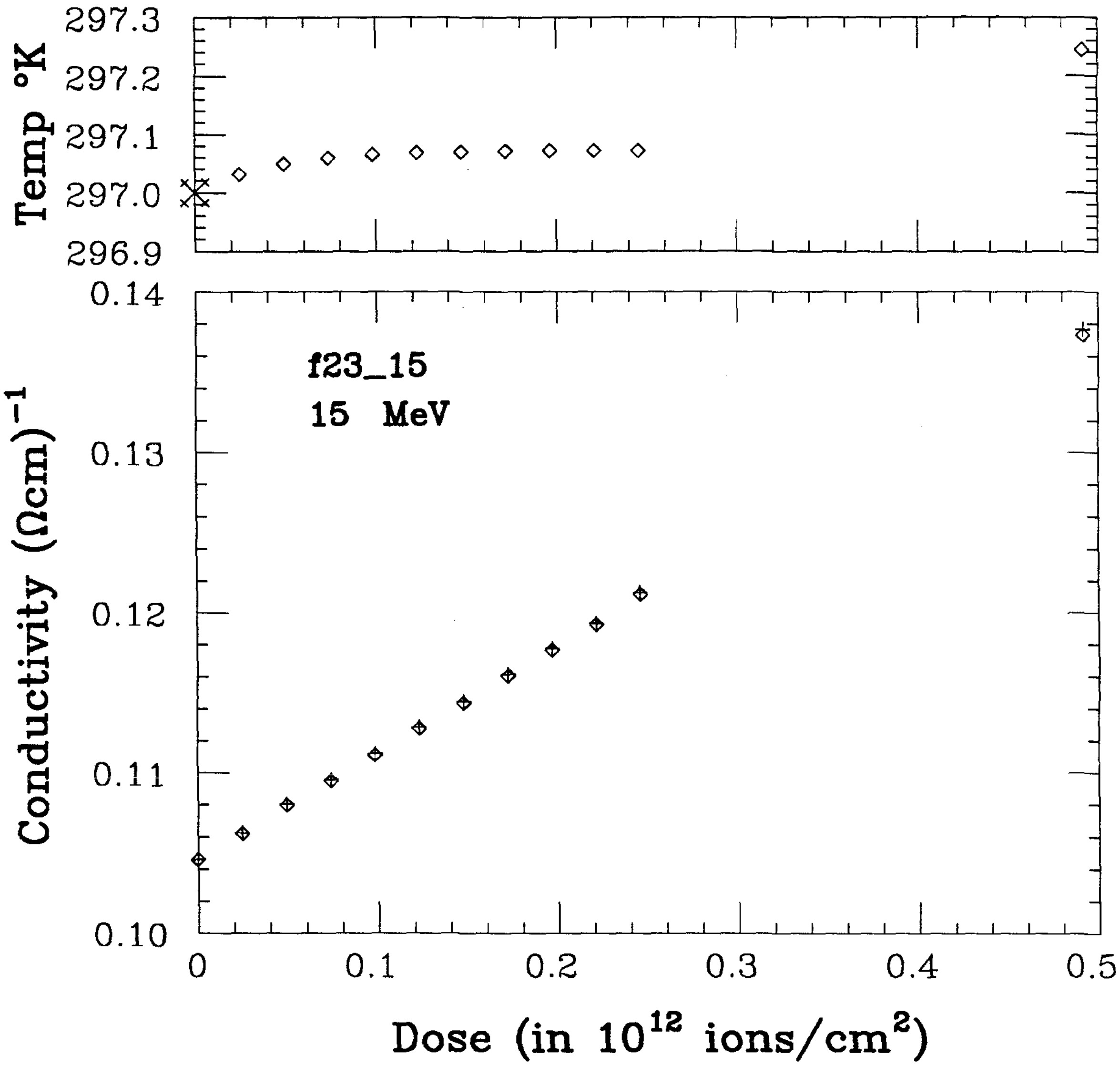

Figure 5.1

First in a series of seven figures showing the detailed increase in conductivity with ion beam irradiation. In this figure the low dose slope is very well defined by the perfect linearity of the first ten data points. The plus symbols are uncorrected data and the diamonds are corrected data. The graph at the top shows the temperature used to calculate the correction.

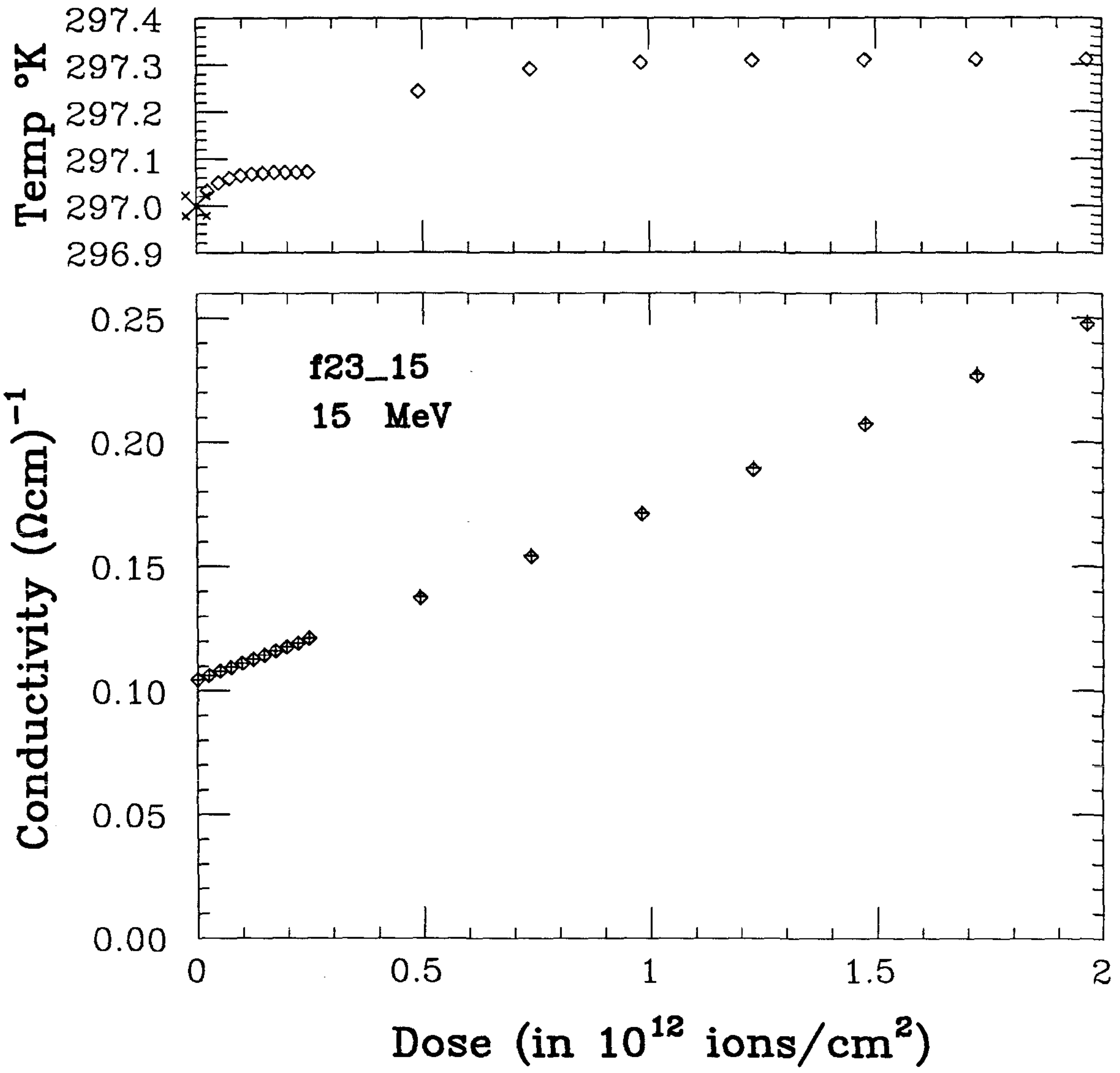

Figure 5.2

Second in a series of seven figures showing the detailed increase in conductivity with ion beam irradiation. In this figure the conductivity is beginning to rise away from the original linearity. The plus symbols are uncorrected data and the diamonds are corrected data. The graph at the top shows the temperature used to calculate the correction.

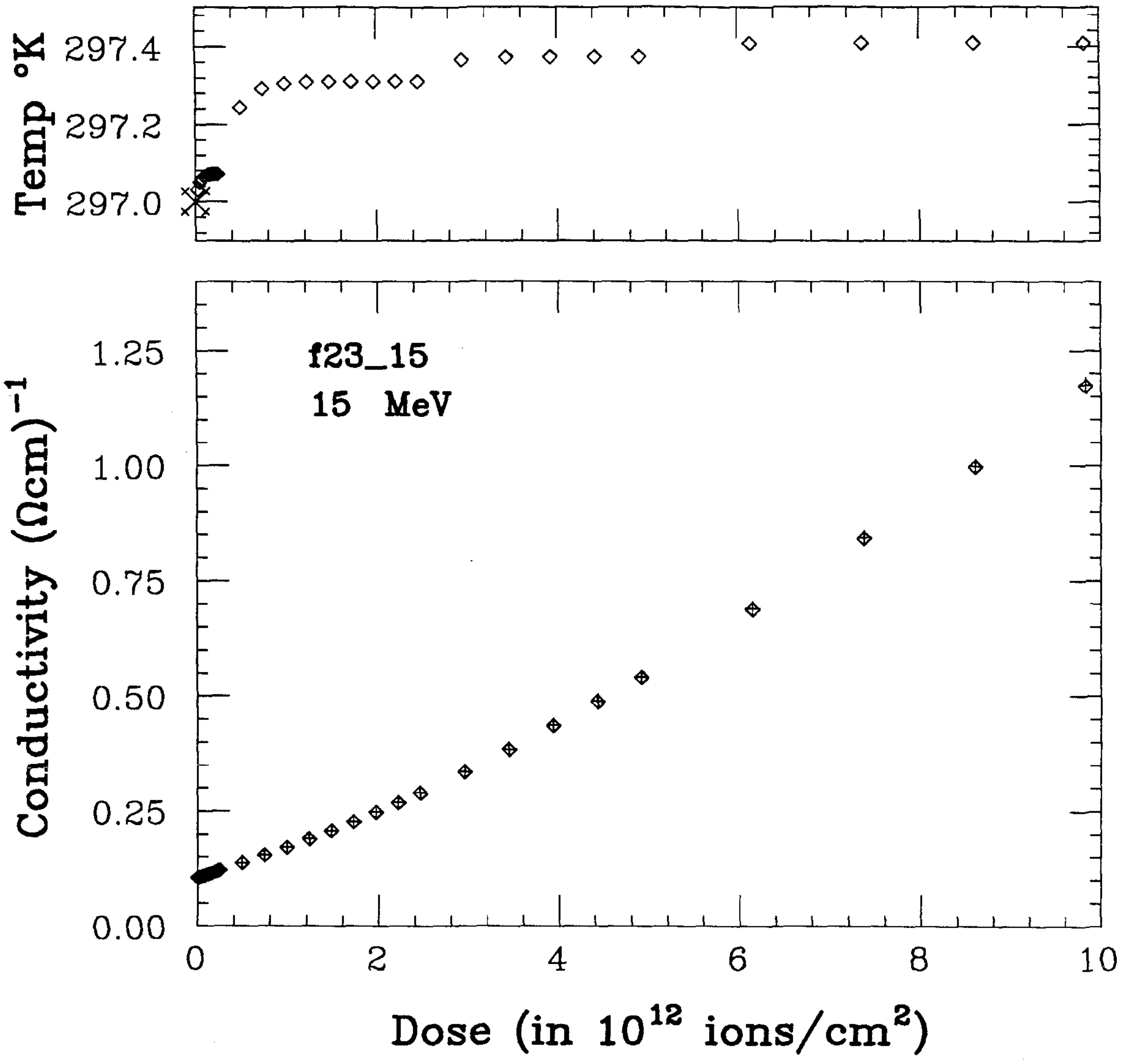

Figure 5.3

Third in a series of seven figures showing the detailed increase in conductivity with ion beam irradiation. In this figure the conductivity is well above the low dose slope linearity as it makes the transition to the medium dose slope. The plus symbols are uncorrected data and the diamonds are corrected data. The graph at the top shows the temperature used to calculate the correction.

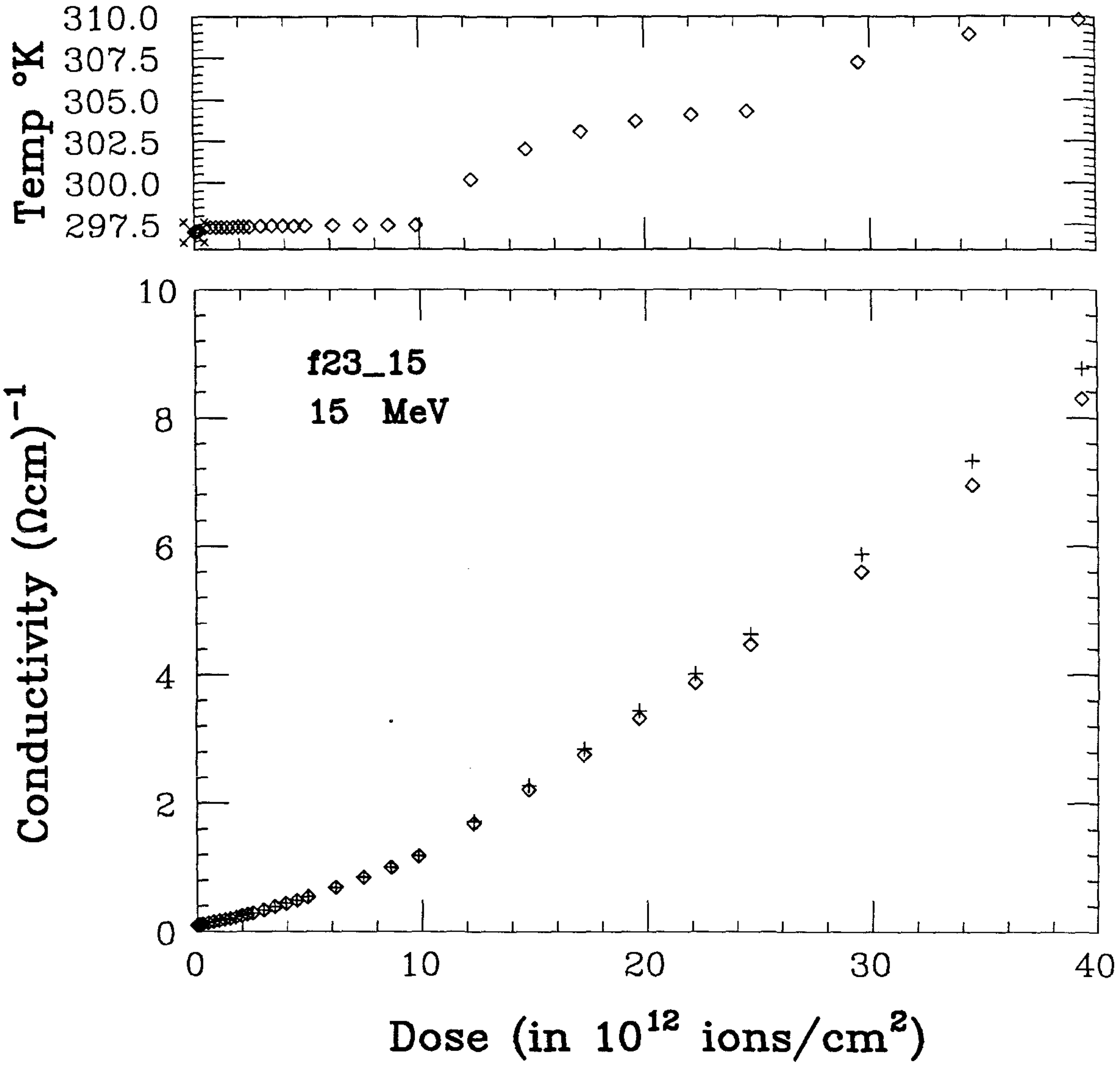

Figure 5.4

Fourth in a series of seven figures showing the detailed increase in conductivity with ion beam irradiation. In this figure the transition from low dose slope to medium dose slope is nearly complete. The plus symbols are uncorrected data and the diamonds are corrected data. The graph at the top shows the temperature used to calculate the correction.

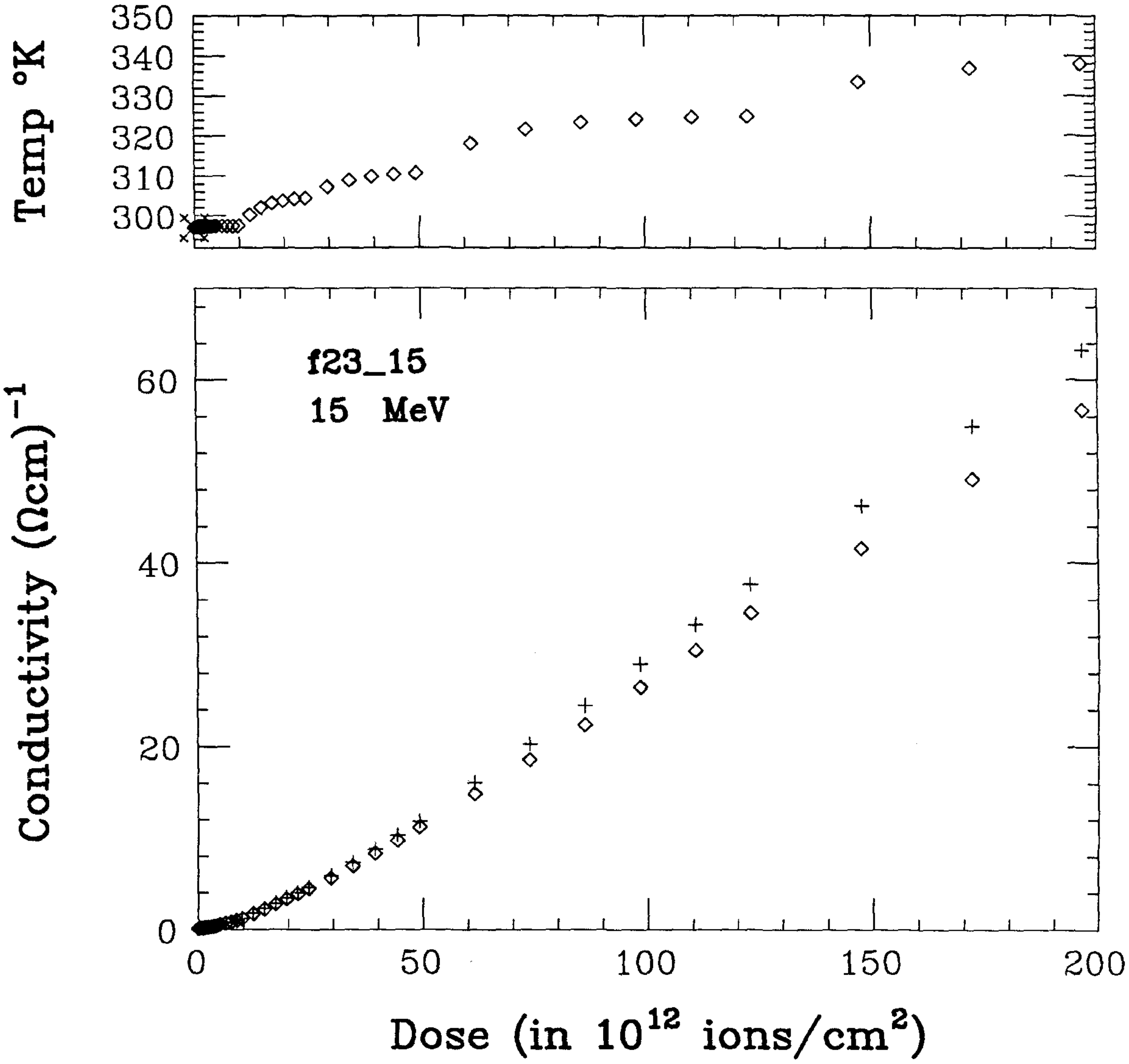

Figure 5.5

Fifth in a series of seven figures showing the detailed increase in conductivity with ion beam irradiation. In this figure the conductivity has completed its transition to the second region of linearity. The plus symbols are uncorrected data and the diamonds are corrected data. The graph at the top shows the temperature used to calculate the correction.

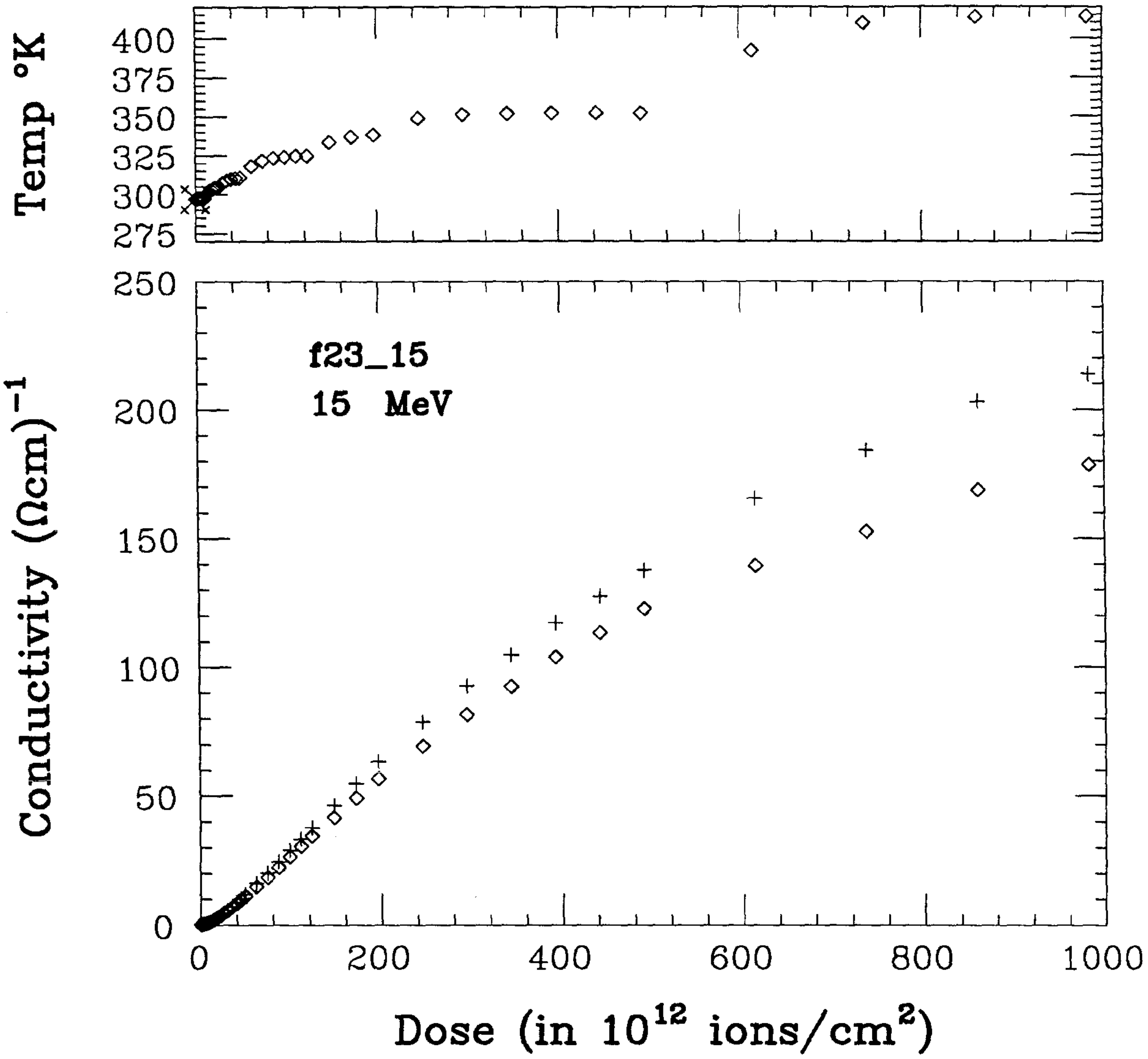

Figure 5.6

Sixth in a series of seven figures showing the detailed increase in conductivity with ion beam irradiation. In this figure the conductivity begins to fall away from linearity as it approaches saturation. The plus symbols are uncorrected data and the diamonds are corrected data. The graph at the top shows the temperature used to calculate the correction.

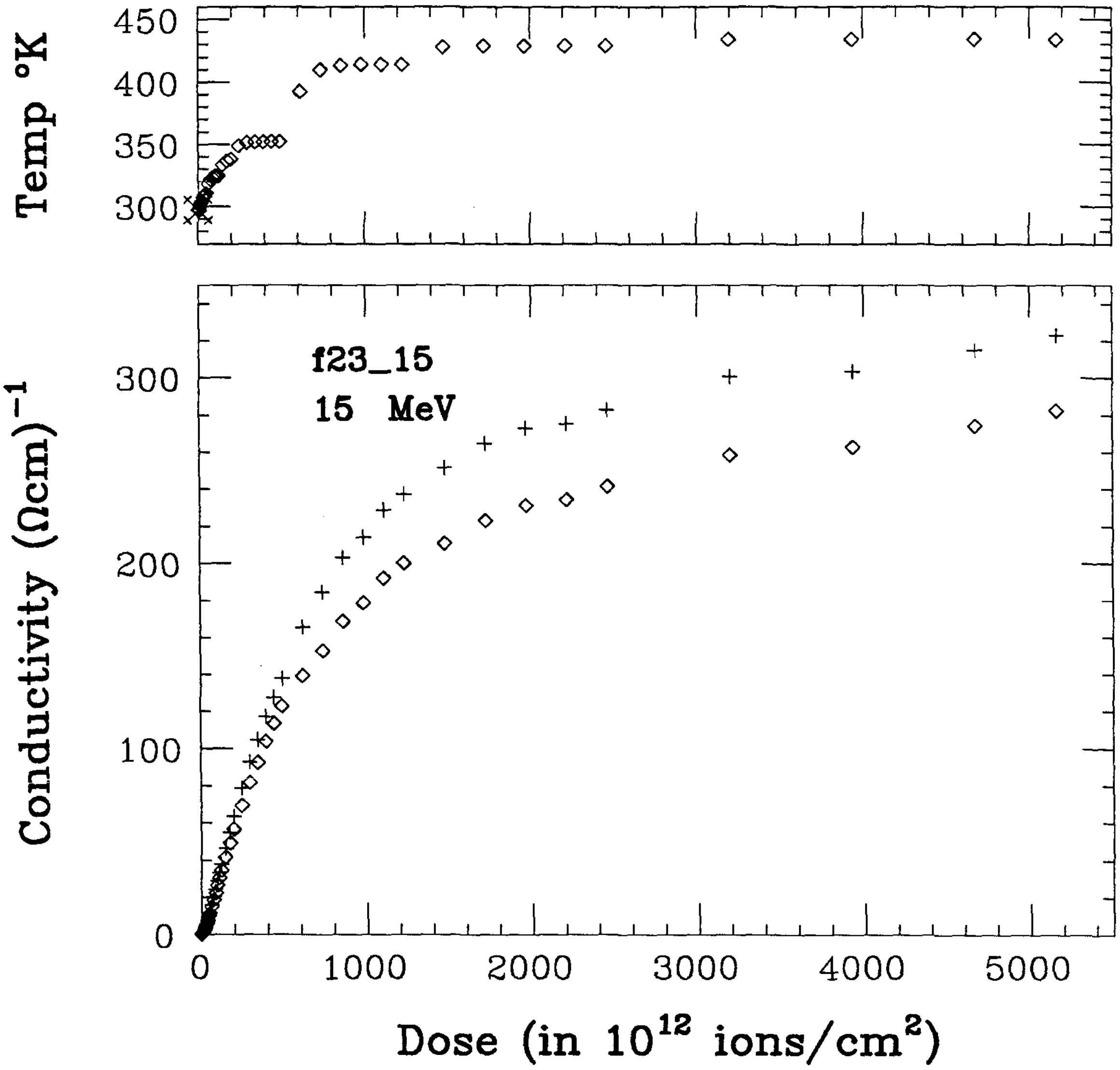

Figure 5.7

Last in a series of seven figures showing the detailed increase in conductivity with ion beam irradiation. In this figure the conductivity has nearly saturated and the entire curve takes on the appearance of a coverage function such as Equation (5.4). The low dose slope is no longer detectable. The plus symbols are uncorrected data and the diamonds are corrected data. The graph at the top shows the temperature used to calculate the correction.

the cross section, b. Writing σ_s for the conductivity part gives:

$$d\sigma = \sigma_s b d\phi, \tag{5.1}$$

for small $d\phi$. This $d\phi$ is reduced slightly when overlap is included. The amount of overlap is proportional to the conductivity at hand. Including the overlap effect:

$$d\sigma = \sigma_s b d\phi - \sigma b d\phi \ . \tag{5.2}$$

Integration yields:

$$-\ln\left(\frac{\sigma_s - \sigma}{\sigma_s}\right) = b\phi + C \ , \tag{5.3}$$

where C is the constant of integration. If the initial conductivity is $\sigma_{pristine}$ then the value of C is $\sigma_{pristine}$. When ϕ is infinite the conductivity is expected to be σ_{sat}. Forcing this condition yields $\sigma_s = \sigma_{sat} - \sigma_{pristine}$. Since $\sigma_{sat} \gg \sigma_{pristine}$, it is reasonable to approximate σ_s by σ_{sat}. Then the solution $\sigma(\phi)$ to Equation (5.2) is:

$$\sigma(\phi) = \sigma_{pristine} + \sigma_{sat}(1 - e^{-b\phi}) \ . \tag{5.4}$$

This is a typical coverage function. It represents the cumulative effect of the cross section b.

The actual dose dependence is much more complicated than Equation (5.4). However, the coverage function does closely represent the dose dependence near saturation. It is even useful in the region of the medium dose slope just before saturation. It is in that range where ϕ is not too small nor too large. In this range $\sigma_{pristine}$ is negligible. The region of the medium dose slope is where the coverage function is still linear:

$$\sigma(\phi) = \sigma_{sat}[1 - (1 - b\phi + b^2\phi^2 - \cdots)]$$

$$\cong \sigma_{sat} b\phi \ . \tag{5.5}$$

The slope is simply:

$$\frac{d\sigma}{d\phi} = \sigma_{sat} b \ . \tag{5.6}$$

Knowing both $\frac{d\sigma}{d\phi}$ and σ_{sat} gives the cross section:

$$b = \frac{1}{\sigma_{sat}} \frac{d\sigma}{d\phi} \ . \tag{5.7}$$

Thus, it is possible to determine the cross section for conductivity change by ion irradation simply by measuring the medium dose slope and the saturation value.

The slopes of all the conductivity curves were plotted and a few examples are shown in Figures 5.8 to 5.13. With the exception of the 1 MeV data, all of the $\frac{d\sigma}{d\phi}$ curves increase to a peak and then fall toward zero. The first few points represent the low dose slope. The points at the peak give the medium dose slope.

3. Cross Sections at Different Energies

It is evident from Figures 4.2, 4.3, and 4.4 that some energies are more effective in raising conductivity. This means that there is a higher cross section associated with those energies. There may even be two cross sections associated with each energy as discussed in the previous section. Figure 4.4 hints that this is so. There are some curves that cross one another. This could be because the low dose cross section is larger for one energy, while its medium dose cross section is smaller. The 15 MeV and 20 MeV curves show this effect. It must be noted, though, that this is speculative, since there was one 15 MeV curve (not shown) that was always higher than the 20 MeV data.

All of the low dose slopes have been measured and appear in Figure 5.14. All of the medium dose slopes have been measured and are shown in Figure 5.15. The larger amount of uncertainty in the low dose slopes can

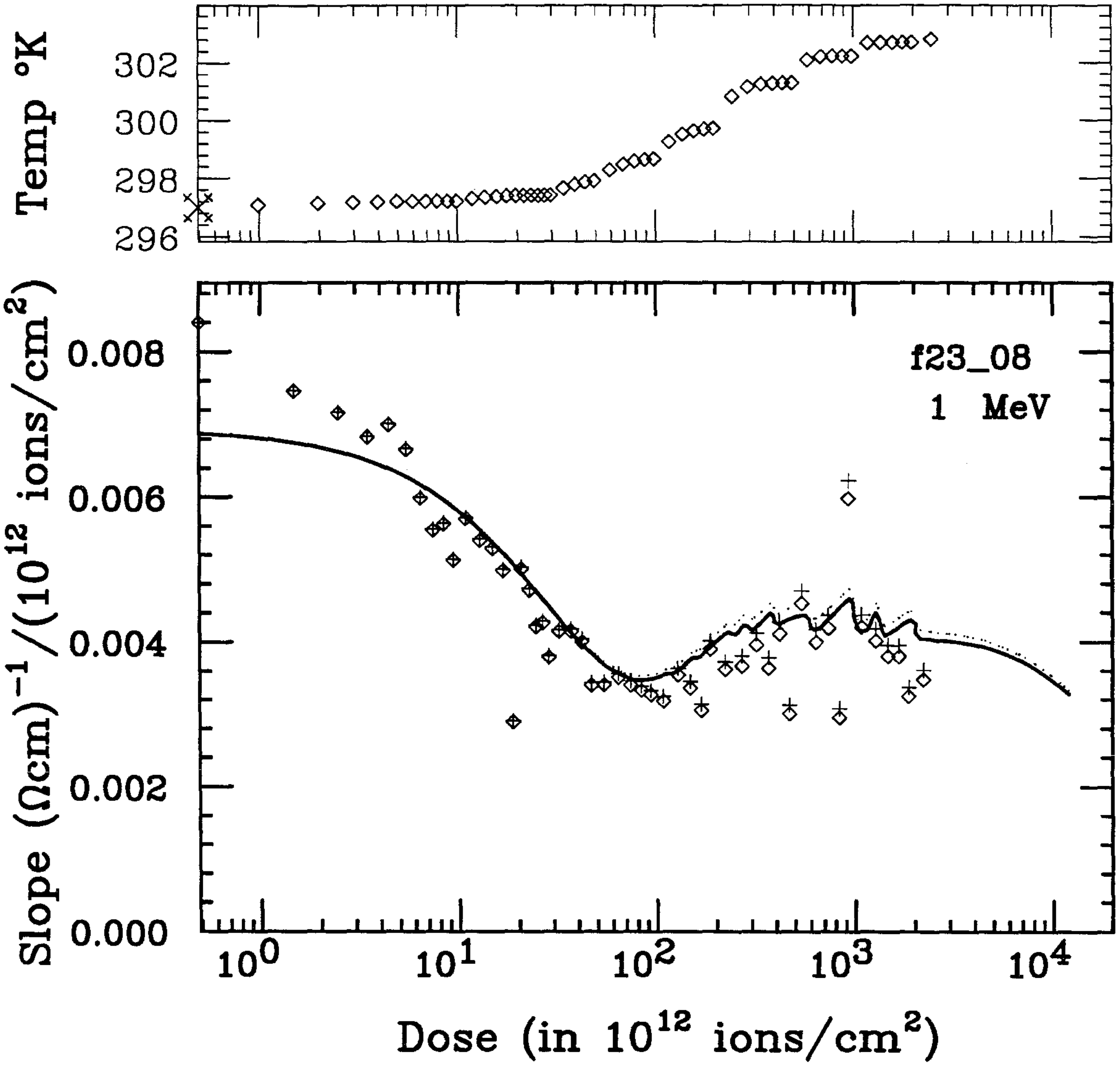

Figure 5.8

An example of the rate of conductivity change with ion beam irradiation. The interpretation of the symbols is the same as in Figure 4.9. In this figure 1 MeV Cl^+ *ions bombarded the carbon film to a dose of* 2.5×10^{15} *ions/cm*^{2}*. At this energy, the slope at low doses is larger than it is at moderate doses. The low dose slope is* 0.0084*. The medium dose slope is* 0.003 *(units given in the figure).*

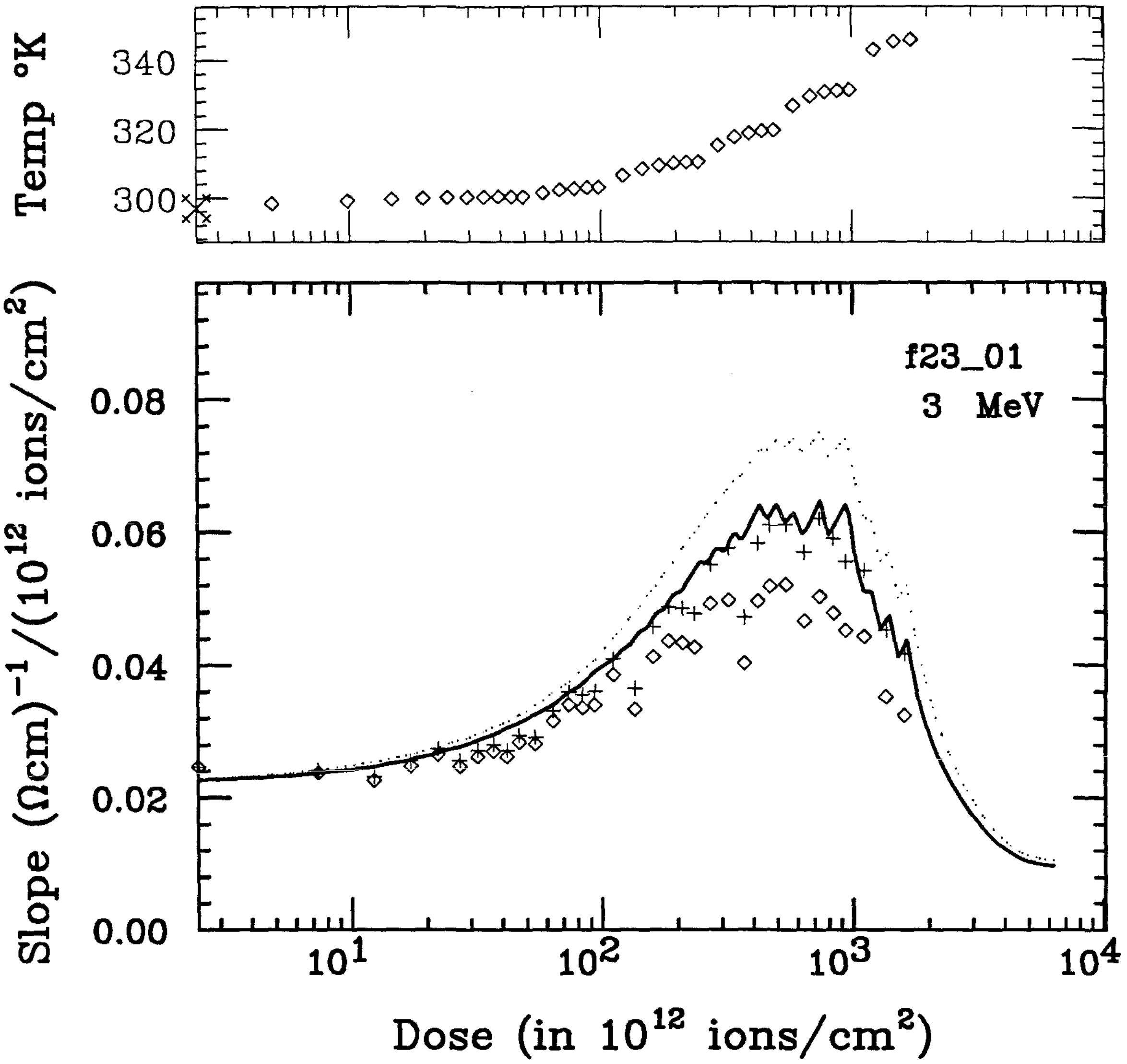

Figure 5.9

An example of the rate of conductivity change with ion beam irradiation. The interpretation of the symbols is the same as in Figure 4.9. In this figure 3 MeV Cl^{2+} *ions bombarded the carbon film to a dose of* 1.7×10^{15} $ions/cm^2$*. The low dose slope is* 0.0204*. The medium dose slope is* 0.053 *(units given in the figure).*

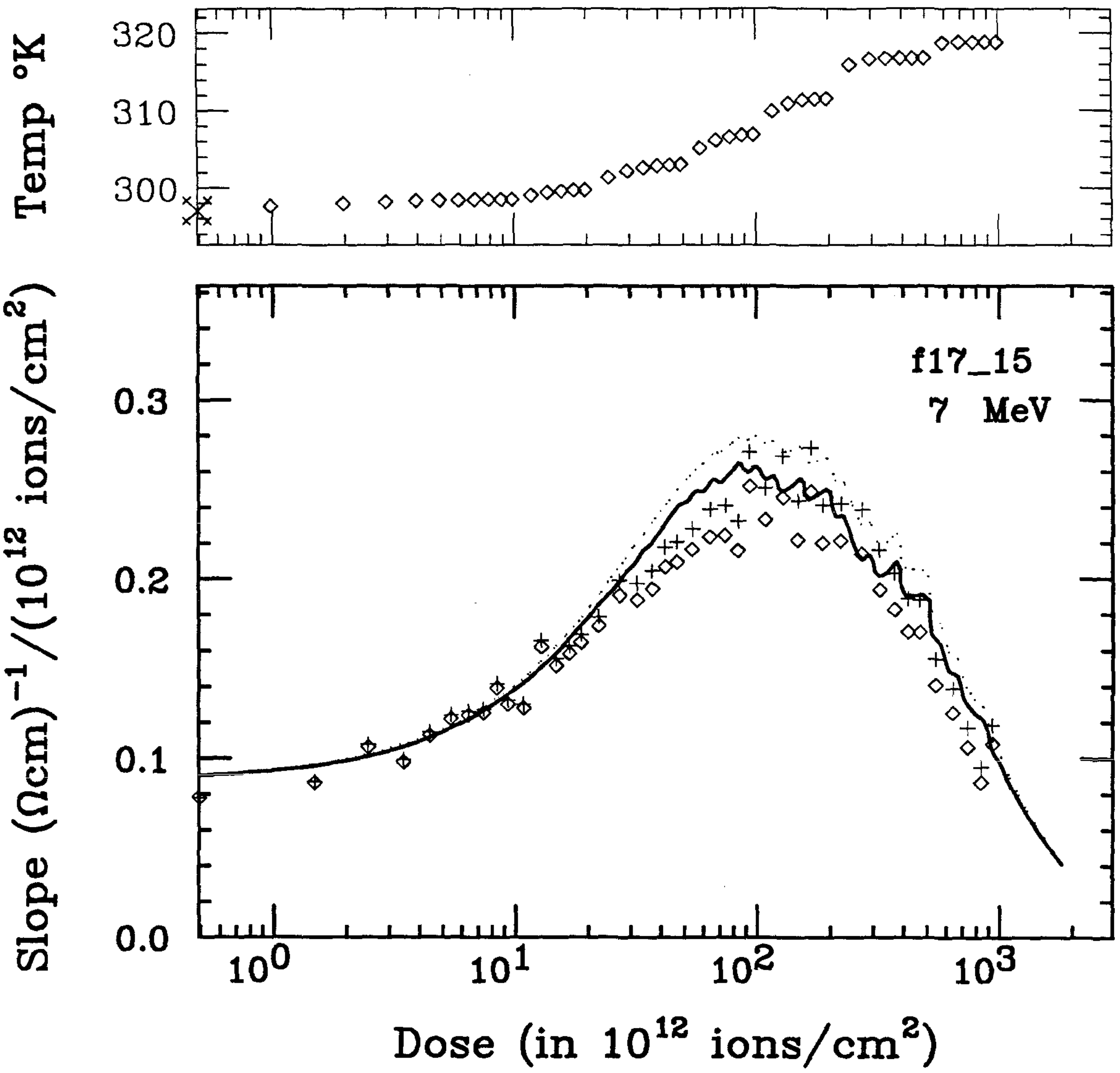

Figure 5.10

An example of the rate of conductivity change with ion beam irradiation. The interpretation of the symbols is the same as in Figure 4.9. In this figure $7\,MeV$ Cl^{3+} *ions bombarded the carbon film to a dose of* 9.8×10^{15} *ions/cm^2. The low dose slope is* 0.0780. *The medium dose slope is* 0.259 *(units given in the figure).*

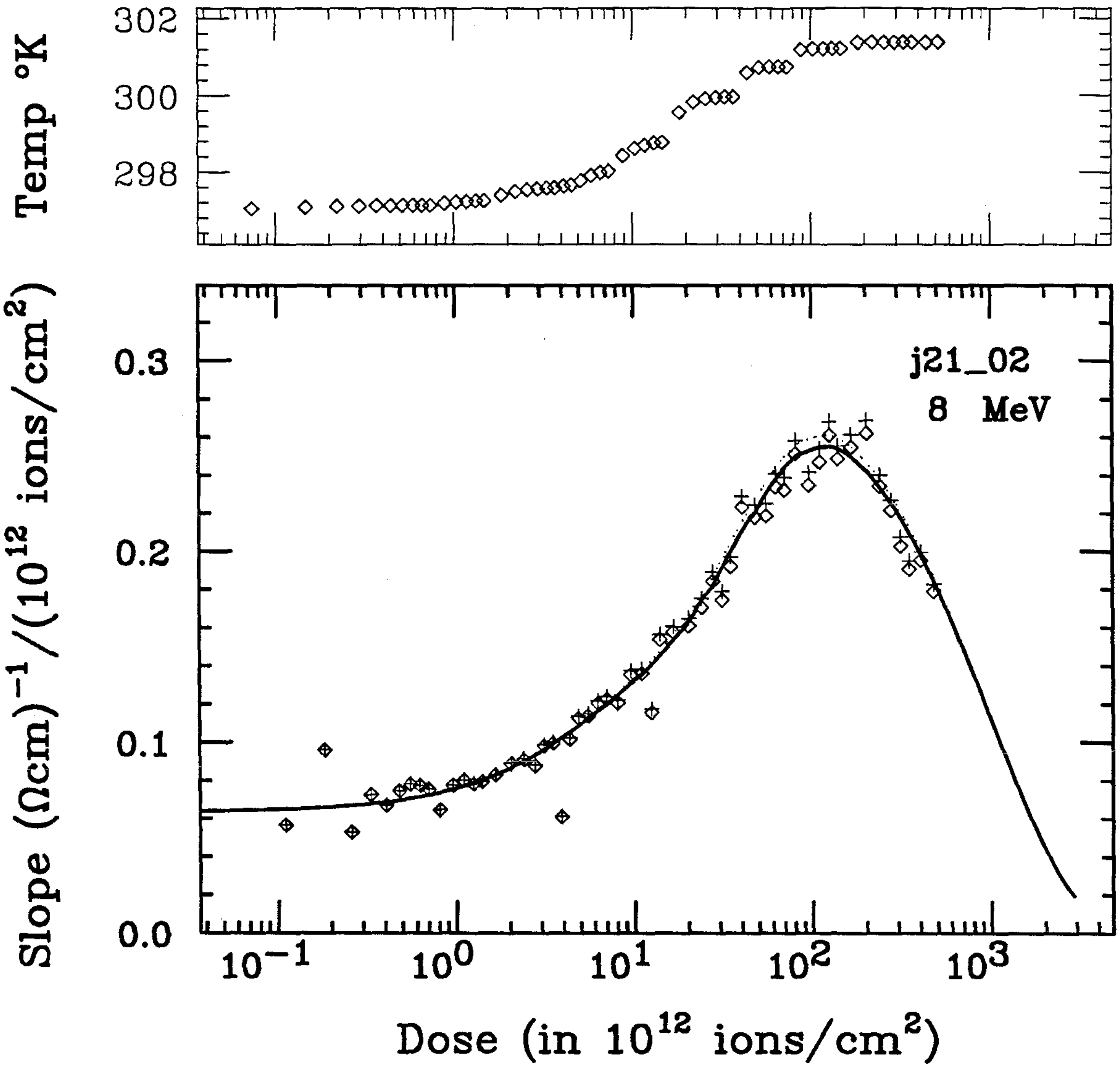

Figure 5.11

An example of the rate of conductivity change with ion beam irradiation. The interpretation of the symbols is the same as in Figure 4.9. In this figure 8 MeV Cl^{4+} *ions bombarded the carbon film to a dose of* 5.2×10^{14} *ions/cm*^{2}. *The low dose slope is* 0.072. *The medium dose slope is* 0.262 *(units given in the figure).*

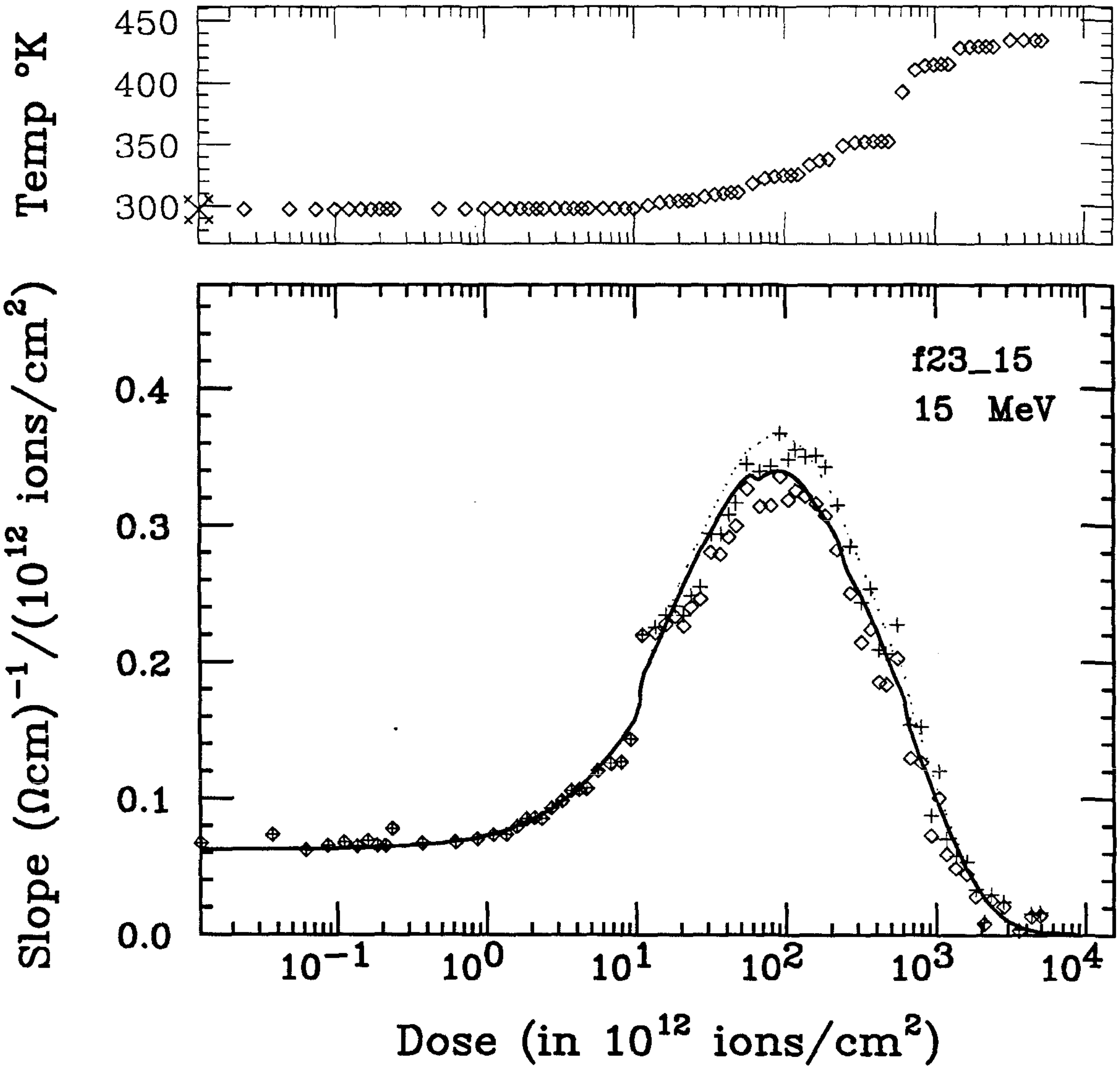

Figure 5.12

An example of the rate of conductivity change with ion beam irradiation. The interpretation of the symbols is the same as in Figure 4.9. In this figure 15 MeV Cl^{4+} *ions bombarded the carbon film to a dose of* 5.1×10^{15} *ions/cm*^{2}*. The low dose slope is* 0.068*. The medium dose slope is* 0.340 *(units given in the figure).*

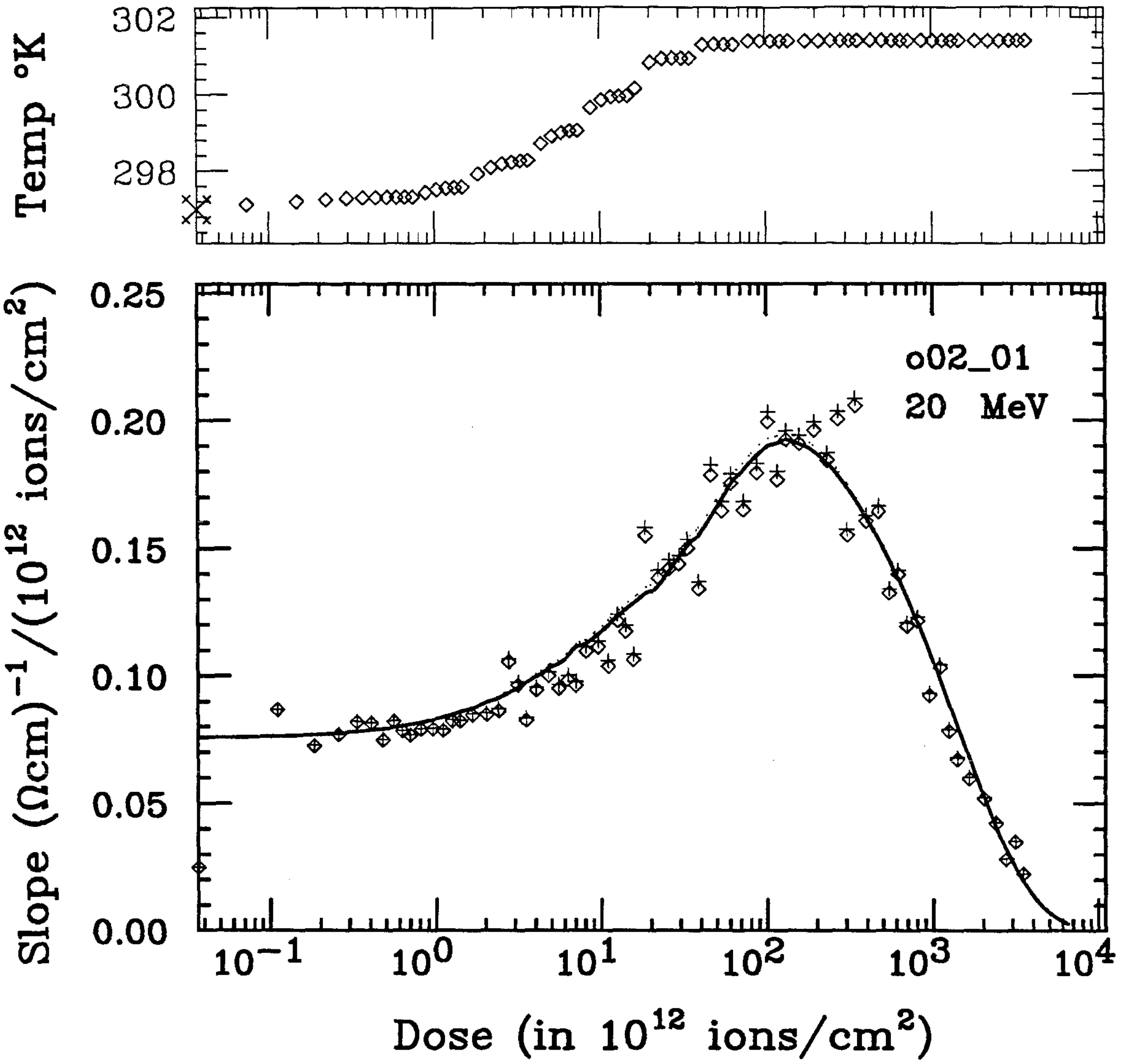

Figure 5.13

An example of the rate of conductivity change with ion beam irradiation. The interpretation of the symbols is the same as in Figure 4.9. In this figure 20 MeV Cl^{5+} *ions bombarded the carbon film to a dose of* 3.5×10^{15} $ions/cm^2$. *The low dose slope is* 0.076. *The medium dose slope is* 0.200 *(units given in the figure).*

be attributed to the different pristine conductivities with which each sample started. These plots of slopes, which are directly related to cross sections, are called excitation curves. They are energy-dependent cross sections. They are both peaked at an ion energy of about 12 MeV. They are both different from the electronic stopping power curve shown in Figure 3.1. This suggests that something more involved than just energy deposition is behind the process that increases the conductivity.

4. Comparision with the Ion-Track Model

The ion-track model was discussed in Section 3.2. This model accounts for the diminishing of deposited energy *density* as bombarding energy increases. The 25 MeV energy ions (peak in $\frac{dE}{dx}$ curve) may deposit more energy-per-unit length, but the deposition covers a larger disk perpendicular to the ion track. The disk is larger because the δ electrons penetrate to a radius proportional to the ion's kinetic energy per *amu*. This results in a shifting of the excitation curve's peak to an energy lower than that of the stopping power. The amount of downshift is adjustable by the 50% ion energy deposition radius $r_{0.5}$. The larger $r_{0.5}$ is made, the more the peak shifts. Setting $r_{0.5}$ to 3.5Å gives excitation curves peaked at 12 MeV. This means that a fairly large core 7Å in diameter receives 50% of the deposited energy, but it does not contribute to the increased conductivity. The concentration of energy is, perhaps, too high in this region.

There are three other measurements that go into the final form of the theoretical curve. As discussed in Section 3.2, they are the radius of destruction r_d, the region size L, and the number of δ electron hits m. The radius of destruction should not be too much different from the 50% energy deposition radius $r_{0.5}$. However, because of the singularity in Equation (3.22), it must be larger than $\frac{1}{2}L$. The integration in Equation (3.16) should not

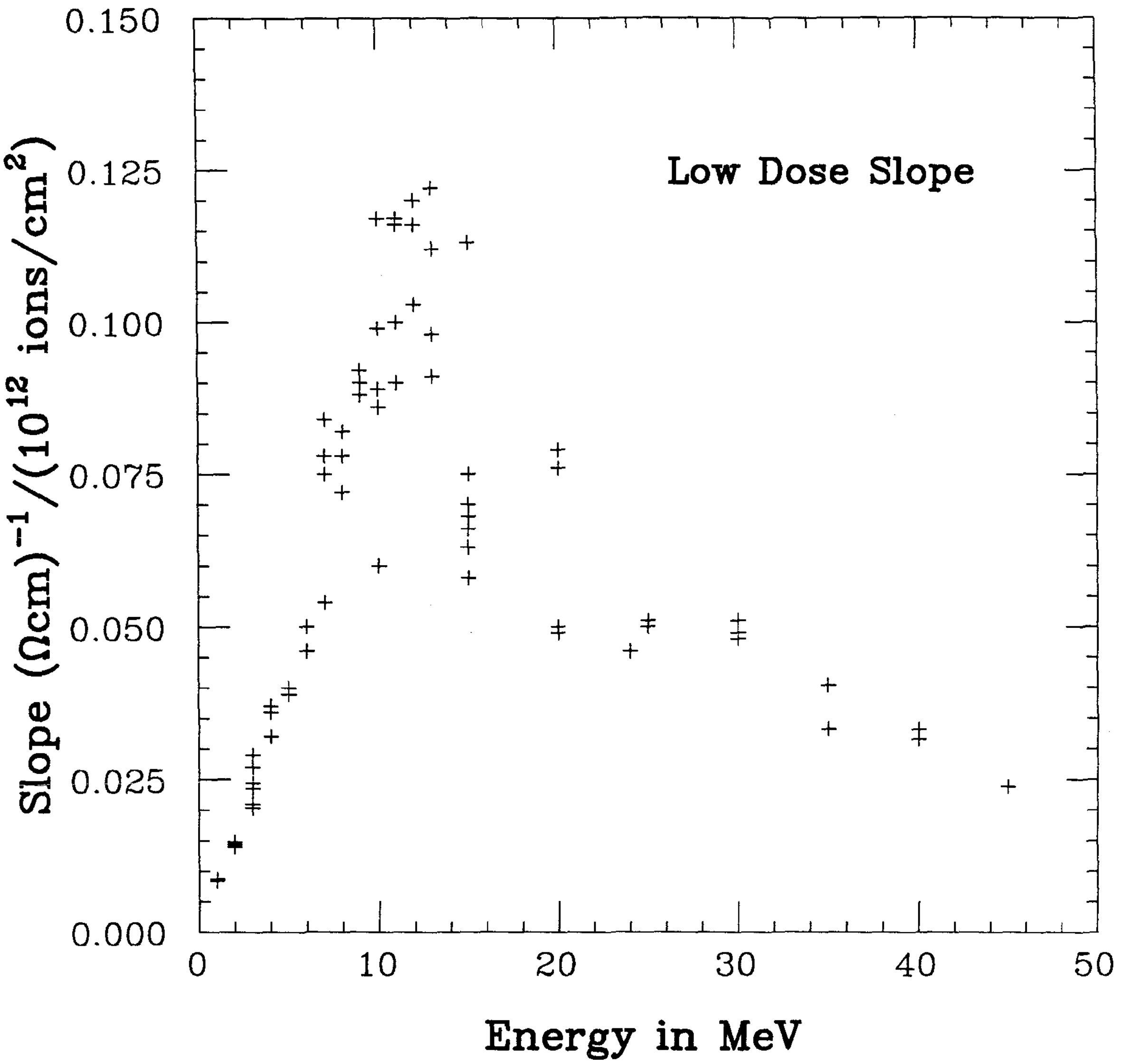

Figure 5.14

Low dose slopes of conductivity data are plotted against the energy of the incident chlorine ion. These data were taken from curves such as those in Figures 5.8 to 5.13. The peak in the curve is $\sim 12\ MeV$*, which is much lower in energy than the peak in the electronic stopping power (see Figure 3.1).*

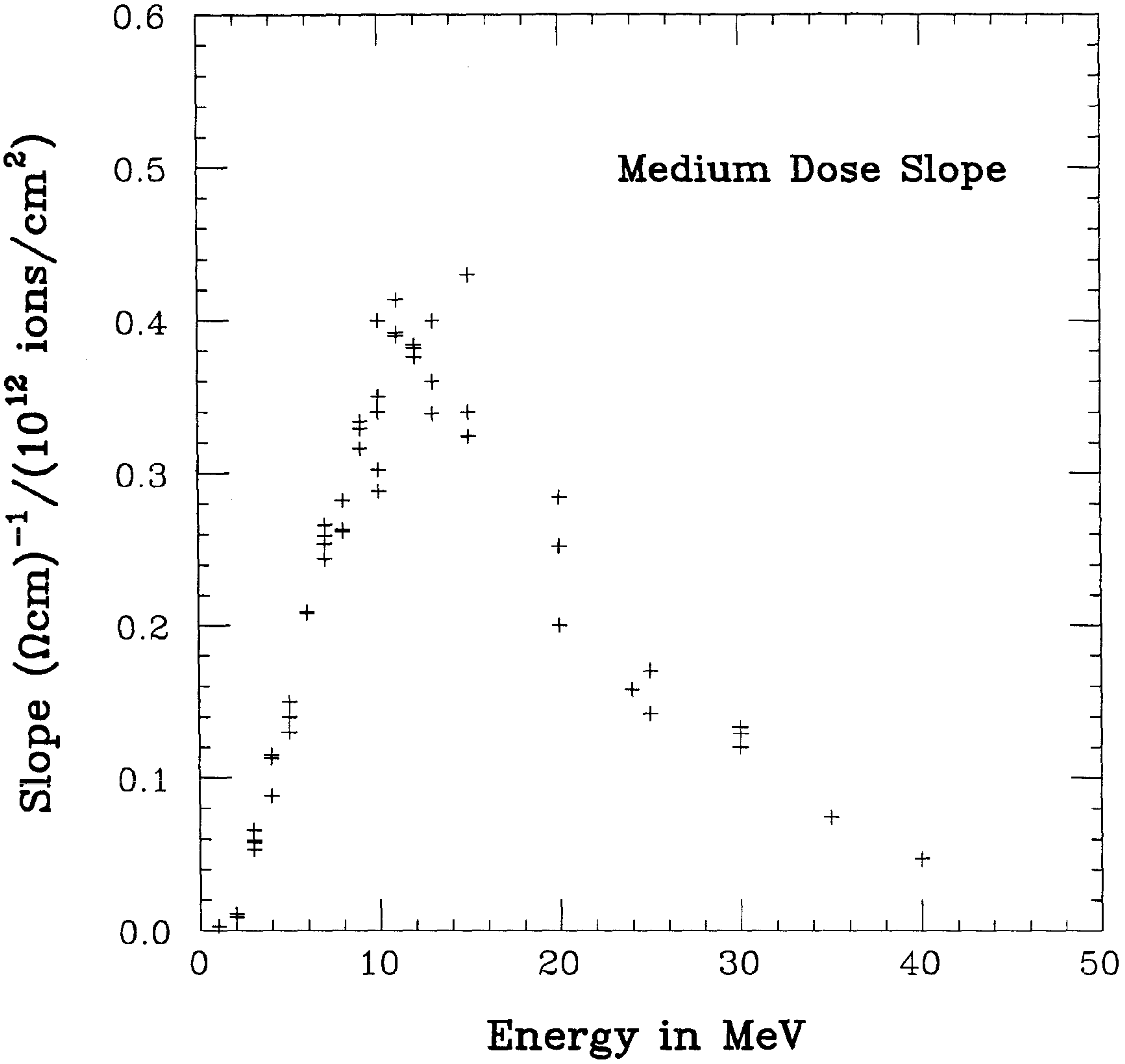

Figure 5.15

The medium dose slopes of conductivity data are plotted against the incident ion energy. These data were taken from curves such as those in Figures 5.8 to 5.13. This excitation curve also peaks at $\sim 12\ MeV$.

bring the region L within the core defined by $r_{0.5}$. This means that

$$r_d = \frac{1}{2}L + r_{0.5} \ . \tag{5.8}$$

With two of the four variables nailed down, it is rather simple to find those pairs of L and m that produce excitation curves close to the ones that go with the slope data.

Some close-fitting excitation curves have been drawn in Figure 5.16 using carefully chosen hit numbers and region sizes. Included in that figure are the medium dose slope data from Figure 5.15. Those data have been divided by the saturation conductivity according to Equation (5.6). The value used was $\sigma_{sat} = 300(\Omega cm)^{-1}$.

Similarly, the low dose slope data are treated in Figure 5.17.

A hit number of $m = 22$ with region size $L = 28.1$Å seems to produce an excitation curve that most closely represents the medium dose slope data. The low dose slope data are best represented by 8 hits upon a region 6.2 Å on a side. These matches to the experimental data are subject to some variation as can be seen in the figures. The rather large amount of spread in the data near the peaks makes a perfect match impossible.

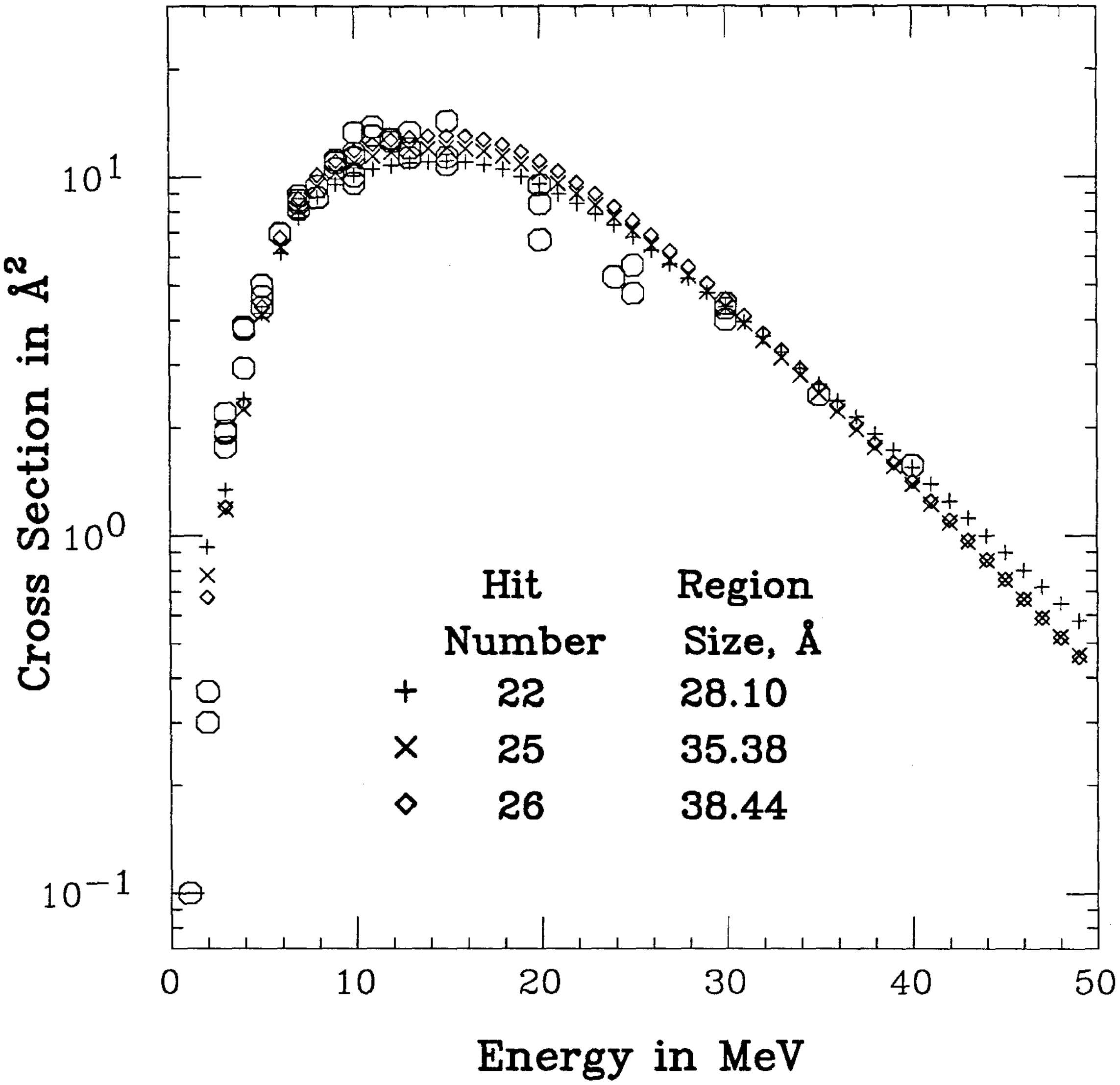

Figure 5.16

A comparison of excitation curves predicted by the Ion-Track Model with medium dose slope data. The slope data have been divided by σ_{sat} *to produce cross sections. The experimentally determined cross sections are marked by large octagons. Several theoretical curves are drawn to demonstrate the ranges of hit numbers and region sizes that best represent the experimental data.*

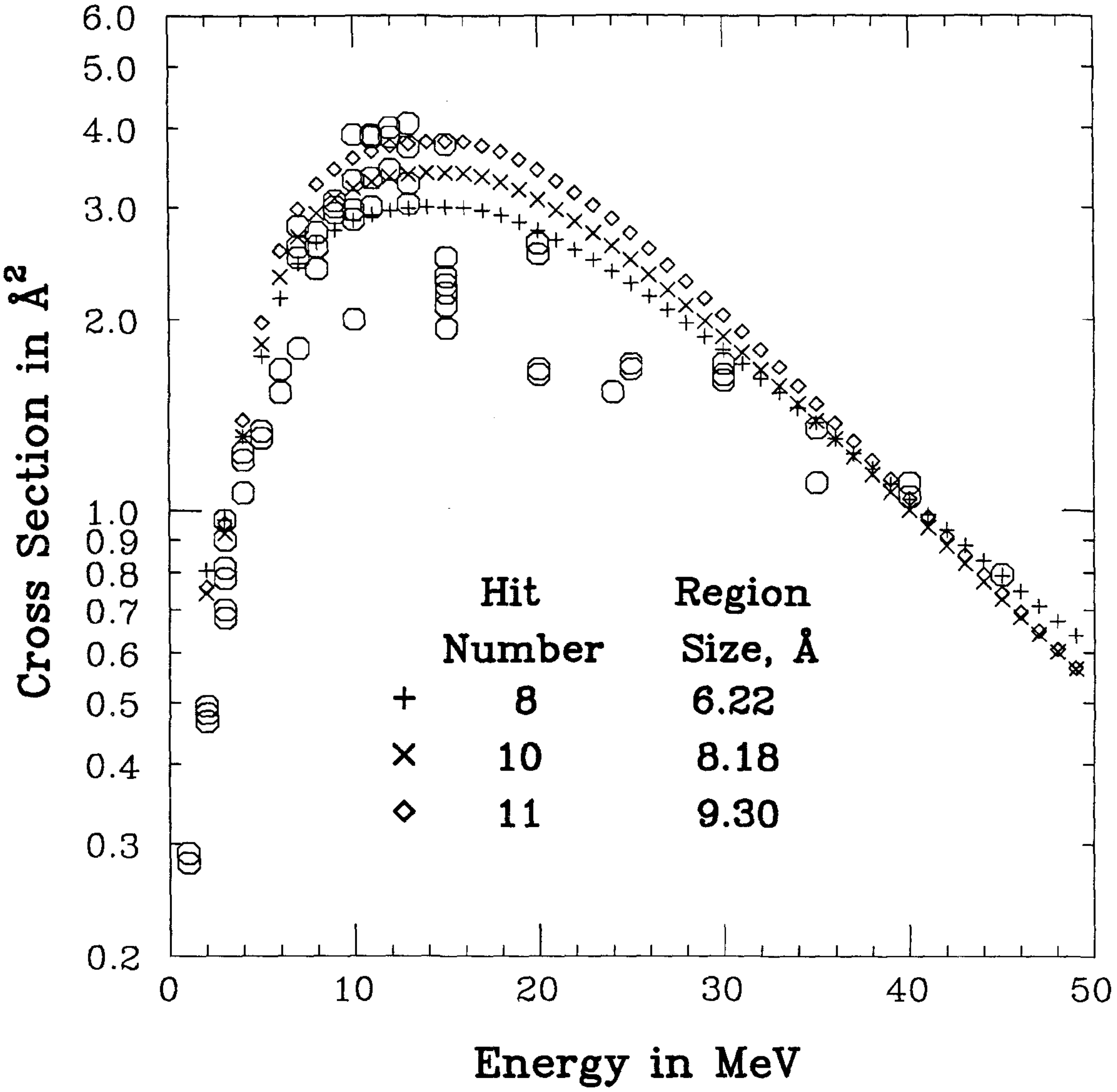

Figure 5.17

A comparison of excitation curves predicted by the Ion-Track Model with low dose slope data. These slopes were also divided by the saturation conductivity in order to produce the associated cross sections. These are drawn as large octagons.

VI. CONCLUSIONS

1. Temperature-Dependent Conductivity

Unirradiated amorphous carbon films have a temperature dependence of approximately +1.2% *per* $°C$ at room temperature. Over a large range of temperatures, this dependence fits the Mott hopping conductivity formula with exponent $\alpha = \frac{1}{2}$. Irradiated films have a lesser temperature dependence of +0.15% *per* $°C$. The conductivity of these films fits the Mott formula with $\alpha = \frac{1}{4}$. The change from $\frac{1}{2}$ to $\frac{1}{4}$ in this model reflects a change in the form of the density of localized states g. The transition suggests that g changes from a parabolic shape to a constant. The transition occurs over an interval of irradiation two orders of magnitude in width. It is coincident with the change in slope (cross section) of the conductivity versus dose.

2. Cross Sections and Hydrogen Loss

The cross sections reported in Chapter Five are consistent with those reported by others (Ba83) and (St87). Baumann et al. found three cross sections of 10Å^2, 2Å^2, and 0.4Å^2 measured by the ^{15}N nuclear resonance reaction. Stecher reported cross sections of 1.6Å^2 for ^{15}N and 6Å^2 for ^{19}F. He also produced TEM photos that indicate that small graphitic crystallites may be formed by the ion irradiation.

The Ion-Track Model suggests that small regions ~6.2Å on a side which are hit by eight δ electrons transform to a higher conductivity. This region size and hit number produce an excitation curve similar to the cross sections associated with the low dose slopes. Such a region contains ~24 carbon atoms. These are coordinated as either sp^2 or sp^3. The transformation of the region is accomplished by the eight δ electrons that deposit energy there. This suggests that eight sp^3 carbons are transformed to sp^2 coordination. Optical spectroscopy studies (Di83) of amorphous carbon indicate that the relative concentration of sp^3 and sp^2 is 0.68 and 0.30, respectively. This changes to 1.0 sp^2 as the carbon is thermally annealed into graphite. These percentages are consistent with the model proposed above.

The medium dose slope cross sections are most closely matched by an Ion-Track Model excitation curve from a region size of ~ 28Å on a side hit by 22 δ electrons. These values indicate that 2% of the carbon atoms are affected by the δ electrons. The larger size and small number of targeted carbons seem to imply that several smaller 6Å–type regions have been joined.

3. Low Energy Effect

Venkatesan et al.(Ve85) showed that 200 keV ion irradiation caused the conductivity to decrease. Figure 3.6 shows that the reason for this is in the form of energy deposition. Low energy ions slow down primarily by nuclear collisions, whereas at high energies the stopping power is dominated by electronic processes. The 1 MeV and 2 MeV irradiations show some of the effect of the nuclear stopping. The low dose slope exceeds the medium dose slope in the case of the 1 MeV irradiation. The 2 MeV irradiation behaved similarly; at first, its slope diminished with dose; later it increased to a medium dose slope which was marginally larger than the low dose slope. These low energy data show that the nuclear stopping destroys the structures responsible for enhanced conduction.

4. Further Work

A more accurate set of measurements is needed to assess the transformation of α from $\frac{1}{2}$ to $\frac{1}{4}$. New apparatus for accurate beam current integration will be necessary. It must be able to account for the secondary electrons that originate both off and on the target. A means of keeping the target at room temperature (or some specified temperature) during irradiation will help to eliminate temperature uncertainty in the conductivity versus dose measurements.

The carbon films could be evaporated in the laboratory in order to understand the effect that thermal history has on the pristine conductivity.

A temperature-controlled target holder would help to answer questions about how the graphite structures form. Is the effect the same if the target is held at liquid-nitrogen temperature during irradiation?

More experiments are needed to investigate the transition from keV to MeV irradiation effects. Perhaps there is an energy that has no effect on the conductivity. That would mean that the rate of structure formation was equivalent to that of structure destruction.

And finally, other ions could be used to test the predictions of the Ion-Track Model. Different ions have different stopping powers. Would plots of low and medium dose slopes match the theoretical excitation curves?

APPENDIX A

Four-Point Probe Voltage

The four-point probe used in this work consisted of an array of four tips evenly spaced in a line. A current I enters the conducting medium through tip number 1 and leaves through tip number 4. This produces a voltage V across tips 2 and 3. This voltage is proportional to the current and the resistivity ρ of the medium,

$$V = \frac{I\rho}{\Lambda} , \qquad (A1)$$

where Λ is a geometrical factor to be derived in this appendix.

When a current I enters an infinite sheet at a point source taken to be the origin, the current density $\mathbf{j}$ at position $\mathbf{r}$ will obey charge conservation:

$$\int_D \mathbf{j}(\mathbf{r})\cdot d\mathbf{s} - I = 0 . \qquad (A2)$$

The current density will be directed outward uniformly $\mathbf{j}(\mathbf{r}) = j(r)\hat{\mathbf{r}}$. If the surface D is taken to be a disk of radius r and thickness τ, then

$$\mathbf{j}(\mathbf{r}) = \frac{I}{2\pi\tau r}\hat{\mathbf{r}} . \qquad (A3)$$

The current density $\mathbf{j}(\mathbf{r})$ is proportional to the electric field $\mathbf{E}(\mathbf{r})$ in the film:

$$\mathbf{j}(\mathbf{r}) = \sigma(\mathbf{r})\mathbf{E}(\mathbf{r}) , \qquad (A4)$$

where the conductivity σ is the proportionality constant. The electric field is the negative of the gradient of the electric potential $\phi(\mathbf{r})$:

$$\mathbf{E}(\mathbf{r}) = -\nabla\phi(\mathbf{r}) . \qquad (A5)$$

Equations (A3), (A4), and (A5) give

$$\frac{I}{2\pi\tau r}\hat{\mathbf{r}} = -\sigma(\mathbf{r})\nabla\phi(\mathbf{r}) \ . \qquad (A6)$$

The electric potential is radially symmetric as is the current density;

$$\nabla\phi(\mathbf{r}) = \frac{d\phi(\mathbf{r})}{dr}\hat{\mathbf{r}}. \qquad (A7)$$

Since the conductivity is uniform across the film

$$\sigma(\mathbf{r}) = const = \frac{1}{\rho} \ , \qquad (A8)$$

where ρ is the resistivity. Using Equation (A7) in Equation (A6) gives

$$\frac{I}{2\pi\tau r} = -\frac{1}{\rho}\frac{d\phi}{dr} \ , \qquad (A9)$$

with solution

$$\phi(\mathbf{r}) = -\frac{I\rho}{2\pi\tau}\ln\frac{r}{r_o} \ . \qquad (A10)$$

Equation (A10) gives the electric potential on the film at any distance $r \neq 0$ from the current source. The radius r_o defines the zero potential.

If the current source is located at $\mathbf{r}_{source}$ and the point of measurement is at $\mathbf{r}$ then the distance r from the source to the point of measure is

$$r = \mid \mathbf{r} - \mathbf{r}_{source} \mid \ , \qquad (A11)$$

and

$$\phi(\mathbf{r}) = -\frac{I\rho}{2\pi\tau}\ln\frac{\mid \mathbf{r} - \mathbf{r}_{source} \mid}{r_o} \ . \qquad (A12)$$

When there is an incoming current source at $\mathbf{r}_{in}$, the measured potential is:

$$\phi_{in}(\mathbf{r}) = -\frac{I_{in}\rho}{2\pi\tau}\ln\frac{\mid \mathbf{r} - \mathbf{r}_{in} \mid}{r_o} \ . \qquad (A13)$$

When there is an outgoing potential source at $\mathbf{r}_{out}$, the measured potential is :

$$\phi_{out}(\mathbf{r}) = -\frac{I_{out}\rho}{2\pi\tau} \ln \frac{\mid \mathbf{r} - \mathbf{r}_{out} \mid}{r_o} \ . \qquad (A14)$$

When there is both incoming and outgoing current sources, the potential is by superposition:

$$\phi(\mathbf{r}) = -\frac{I_{in}\rho}{2\pi\tau} \ln \frac{\mid \mathbf{r} - \mathbf{r_{in}} \mid}{r_o} - \frac{I_{out}\rho}{2\pi\tau} \ln \frac{\mid \mathbf{r} - \mathbf{r_{out}} \mid}{r_o} \ . \qquad (A15)$$

If the currents balance each other, $I_{in} = -I_{out} = I$. Then

$$\phi(\mathbf{r}) = -\frac{I\rho}{2\pi\tau} \ln \frac{r_1}{r_2} \ , \qquad (A16)$$

where

$$r_1 = \mid \mathbf{r} - \mathbf{r}_{in} \mid \ ,$$

and

$$r_2 = \mid \mathbf{r} - \mathbf{r}_{out} \mid \ .$$

In this work the four probes are placed in a line with separation s between them. The potential measured at point 2 is by Equation (A16):

$$V_+ = -\frac{I\rho}{2\pi\tau} \ln \frac{s}{2s} \ . \qquad (A17)$$

At point 3:

$$V_- = -\frac{I\rho}{2\pi\tau} \ln \frac{2s}{s} \ . \qquad (A18)$$

The measured voltage difference $V_+ - V_-$ is:

$$V = \frac{I\rho}{\pi\tau} \ln 2 \ . \qquad (A19)$$

Equation (A19) applies to infinite sheets. The method of images is used to determine the potential distribution in a finite rectangle. When the edges of the rectangle are nonconducting, the resulting array of current sources is

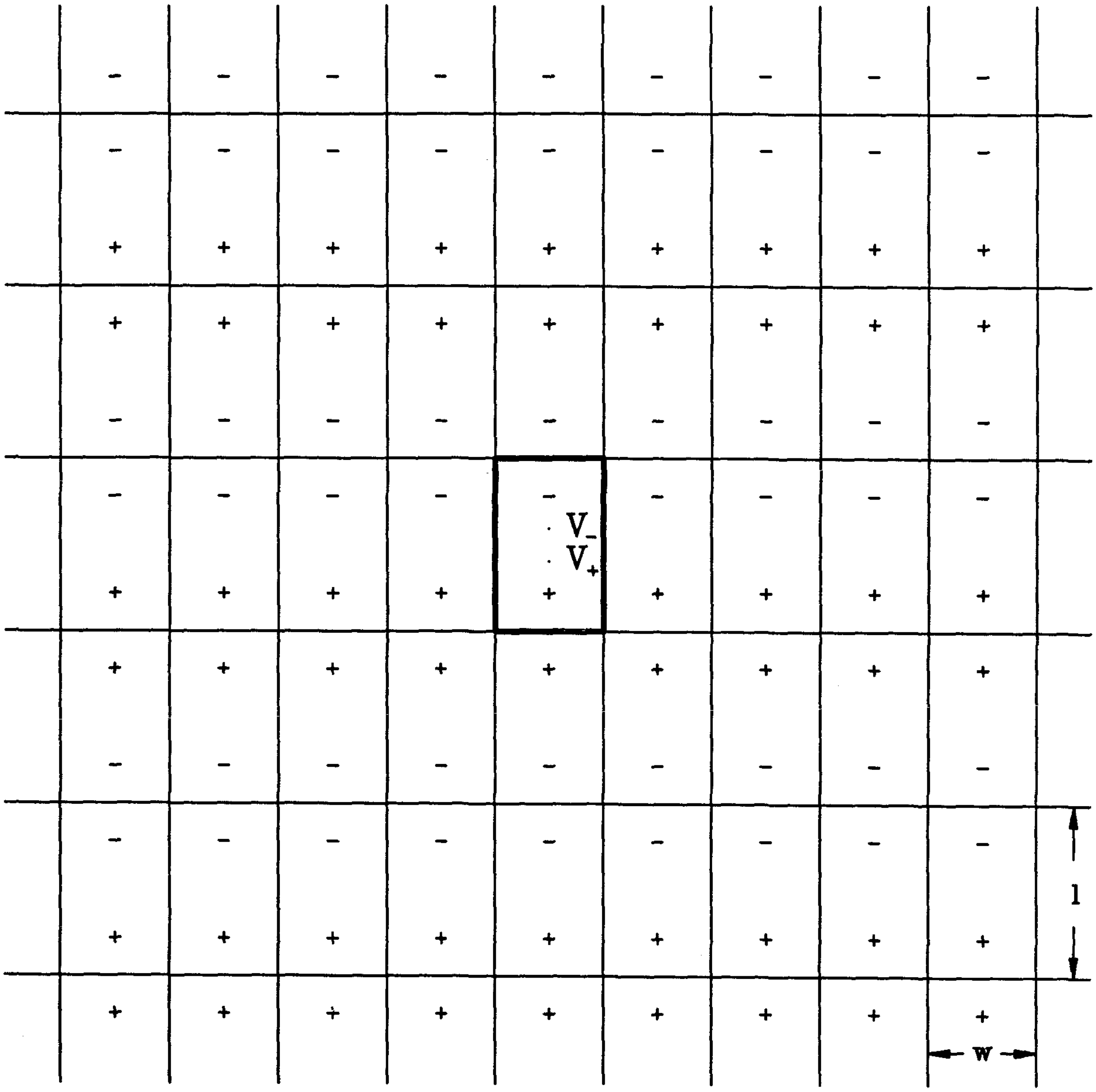

Figure A1

Image current source locations for a rectangular sample (shown in thick lines) of width w and length l. The four-point probe voltage, $V_+ - V_-$, is measured from the locations indicated by the two small dots within the sample.

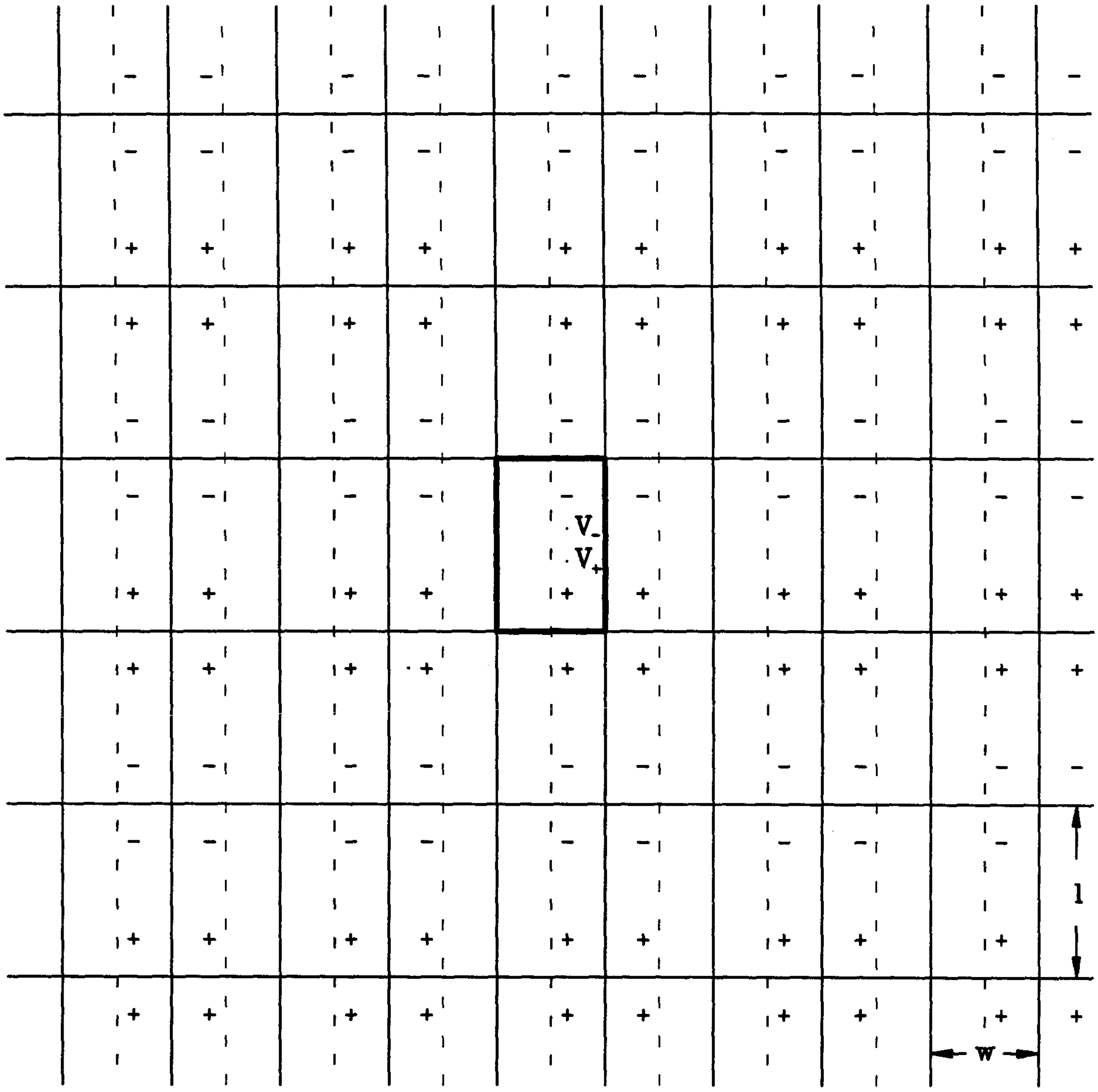

Figure A2

Image current source locations for the case of a widthwise displaced pair of current sources. The centerline of the sample is marked by the dashed line. The + and − sources are shown at a distance δ from the centerline. The points of probe-voltage measurement are also displaced by same amount.

shown in Figure A1 for a rectangle of width w and length l, and the line containing the current sources runs in the center of the rectangle.

If the current source pair is not in the geometrical center then the image sources shift about. Figure A2 shows the case when the current sources are displaced from the width center by amount δ. When $w \ll l$, the effect of a displacement along the other axis is negligible. For an infinite linear array of current sources evenly spaced by distance D, the potential at coordinate (x, y) is (O132):

$$\phi(x,y) = -\frac{I\rho}{2\pi\tau} \ln \left[2\sqrt{sin^2\frac{\pi x}{D} + sinh^2\frac{\pi y}{D}} \right] , \qquad (A20)$$

where the y-axis is perpendicular to the line of sources and $x = 0$ at one of the sources. In the case of Figure A2, there are two sets of linear arrays. The first set has $D = 2w$ and $x = 0$. The second set has $D = 2w$ and $x = w + 2\delta$. In a Cartesian coordinate system having its origin midway between probe tips 2 and 3, the y-coordinates of the positive linear arrays are:

$$y_{+en} = -\tfrac{3}{2}s + 2nl \ ;$$

and

$$y_{+on} = -\tfrac{3}{2}s + a + 2nl \ . \qquad (A21)$$

And the y-coordinates of the negative linear arrays are:

$$y_{-en} = \tfrac{3}{2}s + 2nl \ ;$$

and

$$y_{-on} = \tfrac{3}{2}s + a + 2nl \ . \qquad (A22)$$

In these equations, n takes on the integer values from $-\infty$ to $+\infty$.

The y-coordinate of the V_+ probe is $y_p = -\frac{1}{2}s$. The potential at V_+ is the total of eight infinite sums:

$$
\begin{aligned}
V_+ = &-\frac{I\rho}{2\pi\tau}\sum_{n=-\infty}^{\infty}\ln\left[2\sqrt{0 + sinh^2\left(\frac{\pi(y_p - y_{+en})}{2w}\right)}\right] + \\
&-\frac{I\rho}{2\pi\tau}\sum_{n=-\infty}^{\infty}\ln\left[2\sqrt{sin^2\left(\frac{\pi(w+2\delta)}{2w}\right) + sinh^2\left(\frac{\pi(y_p - y_{+en})}{2w}\right)}\right] + \\
&-\frac{I\rho}{2\pi\tau}\sum_{n=-\infty}^{\infty}\ln\left[2\sqrt{0 + sinh^2\left(\frac{\pi(y_p - y_{+on})}{2w}\right)}\right] + \\
&-\frac{I\rho}{2\pi\tau}\sum_{n=-\infty}^{\infty}\ln\left[2\sqrt{sin^2\left(\frac{\pi(w+2\delta)}{2w}\right) + sinh^2\left(\frac{\pi(y_p - y_{+on})}{2w}\right)}\right] + \\
&+\frac{I\rho}{2\pi\tau}\sum_{n=-\infty}^{\infty}\ln\left[2\sqrt{0 + sinh^2\left(\frac{\pi(y_p - y_{-en})}{2w}\right)}\right] + \\
&+\frac{I\rho}{2\pi\tau}\sum_{n=-\infty}^{\infty}\ln\left[2\sqrt{sin^2\left(\frac{\pi(w+2\delta)}{2w}\right) + sinh^2\left(\frac{\pi(y_p - y_{-en})}{2w}\right)}\right] + \\
&+\frac{I\rho}{2\pi\tau}\sum_{n=-\infty}^{\infty}\ln\left[2\sqrt{0 + sinh^2\left(\frac{\pi(y_p - y_{-on})}{2w}\right)}\right] + \\
&+\frac{I\rho}{2\pi\tau}\sum_{n=-\infty}^{\infty}\ln\left[2\sqrt{sin^2\left(\frac{\pi(w+2\delta)}{2w}\right) + sinh^2\left(\frac{\pi(y_p - y_{-on})}{2w}\right)}\right] \quad . \qquad (A23)
\end{aligned}
$$

The y-coordinate of the V_- probe is $y_n = \frac{1}{2}s$. The potential at V_- is given by Equation (A23) with y_n in place of y_p. The net voltage difference between tips 2 and 3 is

$$V = V_+ - V_- \ . \qquad (A24)$$

A rapidly convergent series for V is obtained by grouping the positive and negative integer values of n in Equations (A23) and (A24).

The effect of the probe-tip displacement δ turns out to be very small. For the sample geometries used in this work there is no more than a

3% increase in the measured voltage over the case with $\delta = 0$. This effect is shown in Figure A3 where δ is allowed to vary from zero to $\frac{1}{2}w$.

In the event that δ is zero, then Equations (A23) and (A24) give, upon summation:

$$V = \frac{I\rho}{\pi\tau}\left[\frac{\pi s}{w} + \ln\left(\frac{1 - e^{-4\pi s/d}}{1 - e^{-2\pi s/d}}\right) + \sum_{n=1}^{\infty} a_n\right] , \tag{A25}$$

where

$$a_n = \frac{1}{n} e^{-2\pi(l-2s)n/d} \frac{(1 - e^{-6\pi sn/d})(1 - e^{-2\pi sn/d})}{(1 + e^{-2\pi nl/d})} . \tag{A26}$$

Define C through Equation (A25) and

$$V = \frac{I\rho}{\pi\tau}\frac{\pi s}{w} C . \tag{A27}$$

Then the resistivity is given by

$$\begin{aligned} \rho &= \frac{w\tau}{sC}\frac{V}{I} \\ &= \Lambda \frac{V}{I} , \end{aligned} \tag{A28}$$

with

$$\Lambda = \frac{\frac{w\tau}{s}}{1 + \frac{w}{\pi s}\ln\left(\frac{1-e^{-4\pi s/d}}{1-e^{-2\pi s/d}}\right) + \frac{w}{\pi s}\sum_{n=1}^{\infty} a_n} . \tag{A29}$$

For this work, the denominator of Λ is very nearly unity, making

$$\rho \sim \frac{w\tau V}{sI} \tag{A30}$$

a very good approximation.

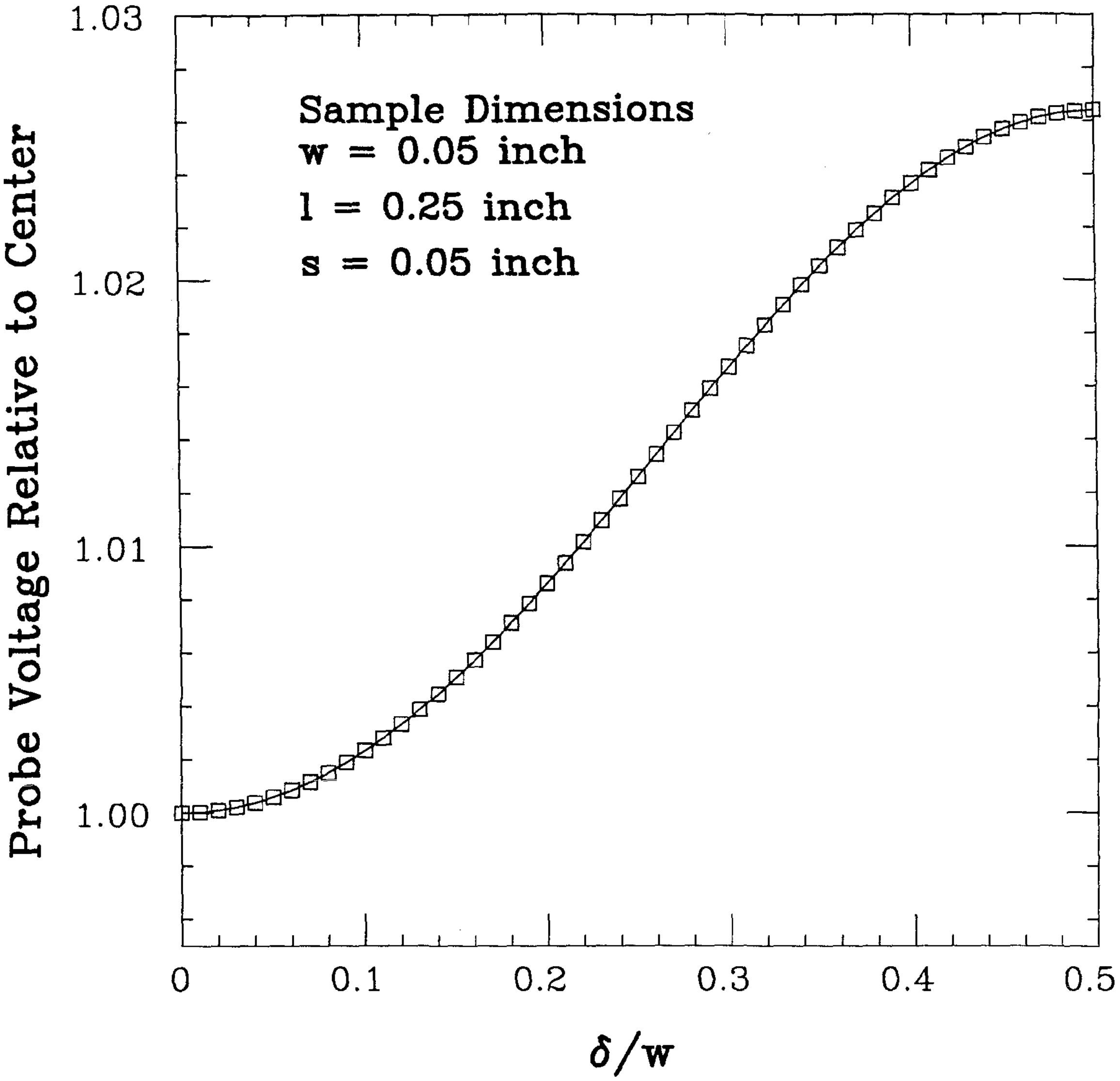

Figure A3

Four-point probe voltage relative to voltage at exact sample center. The probe is displaced by amount δ. As the probe reaches the sample's edge, the expected voltage reaches its maximum deviation of $\sim 3\%$ *more than the voltage found in the middle of the sample.*

APPENDIX B

Curve-Fitting Conductivity vs. Dose Data

The conductivity vs. dose data curves were fit by the model:

$$\sigma(\phi) = \sigma_o(\phi) \exp\left[-\left(\frac{C(\phi)}{k_b T(\phi)}\right)^2\right] , \qquad (B.11)$$

where:

$$\sigma_o(\phi) = \sigma_i + \sigma_{sat}(1 - e^{-\phi/a_{sat}}) , \qquad (B.12)$$

and

$$C(\phi) = \frac{C_{pristine}}{\left[1 + c_1(1 - e^{-\phi/a_1})\right]\left[1 + c_2(1 - e^{-\phi/a_2})\right]} , \qquad (B.13)$$

and $T(\phi)$ is calculated as described in Section (4.2).

The method of fitting involved the minimization of the error-weighted deviations:

$$\delta\Phi = 0 , \qquad (B.14)$$

where:

$$\Phi = \sum_{data}\left(\frac{\sigma(\phi_i) - d_i}{\delta_i}\right)^2 , \qquad (B.15)$$

with $\sigma(\phi)$ given by Equation (B.11). The error δ_i was described in Section 4.1 and is taken to be 1% of the data value d_i. The program that performed the fitting was *Nufit*, supplied by Bruce Vogelaar and Dave Jamieson. It is a very elaborate program that allows the freezing of certain parameters while others are optimized. It allows the user to see the results of the fitting graphically when the minimization of Equation (B.14) is completed.

There are many parameters that go into the fitting function shown in equation (B.11). Most, however, are fixed according to physical circumstances. The most important variable parameters are those in the coverage functions: a_{sat}, c_1, a_1, c_2, and a_2. $C_{pristine}$ is also an important parameter, but it is expected to be "constant" from sample to sample. Similarly, the pristine conductivity $\sigma_{pristine}$ is a "constant." These two parameters may be slightly different from sample to sample. Together they yield the parameter σ_i, setting $\phi = 0$ in eqns. (B.11) and (B.12):

$$\sigma_i = \sigma_{pristine} \exp\left[\frac{C_{pristine}}{k_B T_o}\right] , \tag{B.16}$$

where T_o is room temperature. The parameter σ_{sat} gives the saturated conductivity. It is several orders of magnitude larger than σ_i.

On a crude scale the change of conductivity with dose follows the form of a single coverage function. It is linear at first and comes to a plateau as ϕ/a_{sat} gets larger than unity. If this were exactly true then $\sigma_o(\phi)$ would be adequate to fit the curves. However, there is a change in the slope at low dose. The linearity is preserved as the slope switches over to a (generally) higher value. The functional form of $C(\phi)$ accounts for the change in slope. The change of C with dose is expressed in Equation (B.13).

Two coverage functions were used to account for the, in general, lowering of $C(\phi)$ with dose. It was discovered that one coverage function was inadequate because the curve-fitting process attempted to mimic the effect of a second coverage function by adjusting the thermal parameters in $T(\phi)$ to ridiculous values. Introduction of the second coverage function permitted the thermal parameters to take on reasonable values.

One particular set of data that went well into the saturation region was used to determine a value for the particular parameter σ_{sat}. Then σ_{sat} was fixed to that value for the rest of the fits. This was necessary because most of the data sets stop short of saturation and hence cannot provide any useful information about the value of σ_{sat}. There was, however, no evidence to show that σ_{sat} was different for ions of different energy.

The parameter a_1 was found to be very large for all of the fits. This suggested that the associated coverage function could be simplified to the linear form:

$$f_1(\phi) = 1 + \frac{c_1}{a_1}\phi \ . \qquad (B.17)$$

The parameter a_1 was set equal to 10^5 dose units for all fits. A dose unit is $10^{12}\ \frac{ions}{cm^2}$. Then the variation of c_1 with ion energy contains the useful information of the new linear form of $f_1(\phi)$.

Several data sets were fit on a preliminary basis to establish the many thermal parameters that are used to calculate the target temperature at each measurement. These parameters are:

t_r = time between beam chop and measurement;

t_w = time between measurement and beam start;

T_{hex} = initial temperature of the hexagonal target holder;

T_{slab0} = initial temperature of the brass slab;

C_p = heat capacity of target region;

κ = conductivity of heat away from target region to the brass slab;

$C_{p(holder)}$ = heat capacity of brass slab;

κ_{holder} = conductivity of heat from slab to aluminum holder.

Using data sets f23–15, f23–08, f23–15, and f28–08, the thermal parameters were found to be:

$t_r = 4\ seconds;$

$t_w = 8\ seconds;$

$T_{hex} = 297^\circ K;$

$T_{slab0} = 297^\circ K;$

$C_p = 0.2\ J/^\circ K;$

$\kappa = 0.01\ sec^{-1};$

$C_{p(holder)} = 15.5\ J/^\circ K;$

$$\kappa_{holder} = 0.001\ sec^{-1}\ . \tag{5.1}$$

These values are also consistent with physical arguments and the voltage drift problem of Section 4.3; i.e., the constant κ closely matched the decay constant of the voltage drift.

It is conceivable that the parameters T_{hex} and T_{slab0} could be different for different targets. However, it was found that allowing them to vary did not improve the quality of the fits significantly. So, they were held constant and set to room temperature.

The data set f23–15 was fitted in order to determine the saturation conductivity σ_{sat}. The fitting gave $\sigma_{sat} \sim 303\ (\Omega cm)^{-1}$. The rest of the data curves were fit with this parameter held constant at that value. Similarly $C_{pristine}$ was determined to be approximately 0.0376 eV and supplied to the other data curves.

Table III contains the sample dependent constants:

w = sample width;

τ = sample thickness;

$\sigma_{pristine}$ = Pristine conductivity.

There is a certain amount of variation in $\sigma_{pristine}$ from sample to sample. The greatest jumps in $\sigma_{pristine}$ occur for samples of differing film thickness. This is because they come from physically distinct glass microscope slides. Each slide may have experienced a different thermal history during the thin-film evaporation process. In fact, there were probably thermal gradients across each slide. Thus, the conductivity at one end is somewhat different from that at the other.

Table IV contains the sample irradiation information:

E = ion energy;

TABLE III

Sample Information

Sample Number	Width (cm)	Thickness $(\mu grams/cm^2)$	$\sigma_{pristine}$ $(\Omega cm)^{-1}$
f11–07	$0.1438 \pm .0071$	22.1	0.14133
f11–08	$0.1113 \pm .0036$	22.1	0.13328
f11–09	$0.1455 \pm .0036$	22.1	0.14151
f11–12	$0.1087 \pm .0036$	22.1	0.13961
f11–13	$0.1440 \pm .0046$	22.1	0.14641
f11–14	$0.1387 \pm .0071$	22.1	0.14417
f11–16	$0.1328 \pm .0023$	22.1	0.14943
f11–17	$0.1509 \pm .0023$	22.1	0.14246
f17–02	$0.1478 \pm .0036$	22.1	0.14849
f17–03	$0.1417 \pm .0046$	22.1	0.14030
f17–04	$0.1158 \pm .0036$	22.1	0.15187
f17–05	$0.1405 \pm .0036$	22.1	0.14063
f17–06	$0.1405 \pm .0046$	22.1	0.15813
f17–07	$0.1628 \pm .0036$	22.1	0.14085
f17–08	$0.1326 \pm .0023$	22.1	0.13727
f17–09	$0.1740 \pm .0023$	22.1	0.14794
f17–10	$0.1318 \pm .0036$	22.1	0.16110
f17–11	$0.1349 \pm .0023$	22.1	0.15578
f17–12	$0.1333 \pm .0036$	22.1	0.16457
f17–13	$0.1382 \pm .0036$	22.1	0.16151
f17–14	$0.1885 \pm .0036$	22.1	0.14024
f17–15	$0.1666 \pm .0023$	22.1	0.15958
f17–16	$0.1400 \pm .0036$	22.1	0.16029
f17–17	$0.1374 \pm .0046$	22.1	0.13785
f20–02	$0.1427 \pm .0036$	22.2	0.08199
f20–06	$0.1524 \pm .0023$	22.2	0.08506
f20–07	$0.1384 \pm .0046$	22.2	0.08773
f20–08	$0.1356 \pm .0046$	22.2	0.09315
f20–09	$0.1534 \pm .0036$	22.2	0.09174
f20–11	$0.1412 \pm .0046$	22.2	0.08879
f20–12	$0.1270 \pm .0066$	22.2	0.09007

TABLE III (cont.)

Sample Information

Sample Number	Width (cm)	Thickness ($\mu grams/cm^2$)	$\sigma_{pristine}$ $(\Omega cm)^{-1}$
f20–13	0.1618 ± .0036	22.2	0.09442
f20–14	0.1351 ± .0046	22.2	0.09485
f20–16	0.1250 ± .0046	22.2	0.08993
f20–17	0.1969 ± .0023	22.2	0.09491
f20–18	0.1514 ± .0023	22.2	0.09868
f23–01	0.1402 ± .0036	22.2	0.08320
f23–02	0.1430 ± .0036	22.2	0.10192
f23–03	0.1148 ± .0023	22.2	0.10675
f23–04	0.1621 ± .0036	22.2	0.08902
f23–05	0.1407 ± .0023	22.2	0.10356
f23–06	0.1709 ± .0023	22.2	0.09727
f23–07	0.1326 ± .0023	22.2	0.09946
f23–08	0.1821 ± .0023	22.2	0.09905
f23–09	0.1552 ± .0023	22.2	0.10287
f23–10	0.1646 ± .0023	22.2	0.10346
f23–11	0.1534 ± .0023	22.2	0.10445
f23–12	0.1214 ± .0023	22.2	0.09443
f23–14	0.1356 ± .0023	22.2	0.09656
f23–15	0.1412 ± .0036	22.2	0.10460
f23–16	0.1410 ± .0033	22.2	0.11482
f23–17	0.1410 ± .0036	22.2	0.10778
f23–18	0.1402 ± .0036	22.2	0.10881
f28–01	0.1328 ± .0036	22.2	0.10572
f28–02	0.1422 ± .0046	22.2	0.10638
f28–04	0.1443 ± .0023	22.2	0.10895
f28–05	0.1529 ± .0036	22.2	0.10761
f28–06	0.1316 ± .0036	22.2	0.11028
f28–07	0.1471 ± .0036	20.5	0.09155
f28–08	0.1387 ± .0036	20.5	0.09106
f28–09	0.1440 ± .0036	20.5	0.09336
f28–10	0.1440 ± .0036	20.5	0.08981

TABLE III (cont.)

Sample Information

Sample Number	Width (cm)	Thickness $(\mu grams/cm^2)$	$\sigma_{pristine}$ $(\Omega cm)^{-1}$
j21–01	0.1565 ± .0036	20.5	0.09479
j21–02	0.1422 ± .0051	22.1	0.13096
j21–04	0.1306 ± .0036	22.1	0.14017
j10–01	0.1499 ± .0015	20.5	0.10097
j13–01	0.1811 ± .0025	20.5	0.11124
j18–03	0.1283 ± .0025	22.1	0.14086
j18–04	0.1270 ± .0015	22.1	0.15488
o02–01	0.1730 ± .0023	20.6	0.25424
o31–01	0.1554 ± .0023	20.6	0.19995
s23–01	0.1405 ± .0023	20.6	0.22524

TABLE IV

Sample Irradiation Information

Sample Number	Ion Energy (MeV)	Charge State	Beam Current (nA)	Maximum Dose in $10^{12}(ions/cm^2)$	Final σ $(\Omega cm)^{-1}$
f11–07	13	4^+	30	368.6	106.3
f11–08	13	4^+	30	73.7	22.8
f11–09	13	4^+	45	589.8	160.4
f11–12	12	4^+	30	147.4	51.3
f11–13	12	4^+	30	51.6	16.0
f11–14	12	4^+	25	59.0	19.3
f11–16	11	4^+	20	516.1	148.1
f11–17	11	4^+	20	51.6	15.7
f17–02	11	4^+	15,30	103.2	34.1
f17–03	11	4^+	3.5	8.8	1.4
f17–04	10	3^+	30	108.5	35.0
f17–05	10	3^+	22	589.8	148.8
f17–06	10	3^+	25	68.8	18.2
f17–07	10	3^+	25	58.0	14.2
f17–08	9	3^+	30	134.2	41.0
f17–09	9	3^+	30	587.8	147.2
f17–10	9	3^+	22	68.8	18.3
f17–11	8	3^+	20	786.4	159.3
f17–12	8	3^+	30	98.3	22.5
f17–13	7	3^+	27	29.5	3.8
f17–14	7	3^+	27	137.6	19.6
f17–15	7	3^+	35	983.0	170.0
f17–16	7	3^+	35	103.2	22.8
f17–17	7	3^+	45	98.3	20.5
f20–02	7	3^+	37	137.6	30.0
f20–06	7	3^+	37	19.7	2.2
f20–07	6	3^+	35	491.8	90.9
f20–08	6	3^+	35	98.3	15.8
f20–09	5	3^+	25	688.1	96.1
f20–11	5	3^+	32	88.5	9.0
f20–12	5	3^+	30	98.3	10.6

TABLE IV (cont.)

Sample Irradiation Information

Sample Number	Ion Energy (MeV)	Charge State	Beam Current (nA)	Maximum Dose in $10^{12}(ions/cm^2)$	Final σ $(\Omega cm)^{-1}$
f20–13	4	3^+	22	294.9	29.9
f20–14	4	3^+	19	137.6	12.0
f20–16	3	3^+	3.5	98.3	2.6
f20–17	3	3^+	3.5	68.8	1.7
f20–18	3	2^+	55	383.4	17.5
f23–01	3	2^+	100	1720.2	87.0
f23–02	3	2^+	100	245.7	11.3
f23–03	3	2^+	100	246.7	11.5
f23–04	2	2^+	14	1179.6	25.8
f23–05	2	2^+	14	589.8	11.1
f23–06	2	2^+	14	589.8	10.6
f23–07	1	1^+	15	983.0	4.5
f23–08	1	1^+	15	2457.4	9.9
f23–09	15	4^+	34	13.3	1.9
f23–10	15	4^+	20	13.3	1.9
f23–11	15	4^+	11.5	12.3	1.7
f23–12	15	4^+	6	13.3	1.6
f23–14	15	4^+	2	13.3	1.7
f23–15	15	4^+	0.3,50,100	5160.6	323.0
f23–16	20	4^+	21	184.3	51.0
f23–17	20	4^+	26	73.7	15.9
f23–18	25	5^+	35	118.0	16.9
f28–01	25	5^+	15	118.0	15.7
f28–02	30	5^+	28	106.2	11.7
f28–04	30	5^+	31	118.0	13.4
f28–05	30	5^+	40	118.0	13.4
f28–06	35	6^+	14	78.6	5.5
f28–07	35	6^+	5	32.8	1.5
f28–08	40	7^+	3.5	42.1	1.7
f28–09	40	7^+	5	25.3	1.0
f28–10	45	8^+	0.3	0.3	0.097

TABLE IV (cont.)

Sample Irradiation Information

Sample Number	Ion Energy (MeV)	Charge State	Beam Current (nA)	Maximum Dose in $10^{12}(ions/cm^2)$	Final σ $(\Omega cm)^{-1}$
j21–01	10	4^+	10	285.3	98.1
j21–02	8	4^+	3	516.1	112.9
j21–04	4	3^+	7	655.3	52.9
j10–01	15	4^+	30	1843.1	290.0
j13–01	24	5^+	3	294.9	43.5
j18–01	20	5^+	30	176.9	24.7
j18–04	20	5^+	10	196.6	24.8
o02–01	20	5^+	3	3676.5	276.9
o31–01	13	4^+	13	1718.8	282.3
s23–01	15	4^+	3	221.1	58.9

Q = charge state;

i_o = beam current;

ϕ_{final} = maximum dose;

σ_{final} = conductivity at maximum dose.

Table V contains the sample data fit information: dose scale factor, χ^2 per degree of freedom, and the coverage function parameters. The pre-exponential coverage function, σ_o, is the most dominant term in the fitting equation.

The χ^2 per degree of freedom (χ^2/dof) is a one-figure indication of the quality of fit. Samples with large χ^2/dof may have experienced small drifts in ion beam quality during irradiation. The data set f17–07 has a $\chi^2/dof = 0.80$. This means that the fitted curve lies within the 1% uncertainty of each data point.

TABLE V

Sample Data Fit Information

Sample Number	Ion Energy (MeV)	χ^2/dof	a_{sat} $(10^{12}\frac{ions}{cm^2})$	c_1	c_2	a_2 $(10^{12}\frac{ions}{cm^2})$
f11–07	13	0.80	830.1	1523.0	0.270	5.6
f11–08	13	0.41	778.4	1546.4	0.275	5.8
f11–09	13	4.75	718.9	1807.5	0.295	5.0
f11–12	12	1.97	754.2	1756.9	0.277	4.9
f11–13	12	2.03	375.1	333.1	0.187	7.2
f11–14	12	0.82	458.4	464.9	0.281	7.4
f11–16	11	1.20	727.3	1740.0	0.309	4.8
f11–17	11	0.67	453.8	455.6	0.263	7.7
f17–02	11	1.21	688.7	1159.7	0.236	5.6
f17–03	11	1.83	2245.7	5939.3	4.039	104.8
f17–04	10	3.69	799.8	1497.2	0.355	13.8
f17–05	10	1.30	834.7	1561.6	0.351	4.7
f17–06	10	0.41	929.1	1795.4	0.232	6.3
f17–07	10	1.29	982.8	2067.1	0.203	4.9
f17–08	9	0.80	851.2	1606.9	0.236	4.8
f17–09	9	1.41	841.6	1440.3	0.239	5.2
f17–10	9	0.51	845.7	1311.0	0.274	6.3
f17–11	8	1.86	987.1	1295.5	0.269	6.0
f17–12	8	1.29	1033.7	1204.4	0.249	6.6
f17–13	7	0.33	863.6	259.5	0.238	5.9
f17–14	7	1.40	511.9	25.6	0.140	22.1
f17–15	7	4.69	429.9	56.1	0.245	45.5
f17–16	7	1.65	505.6	159.6	0.205	20.0
f17–17	7	0.79	529.3	157.5	0.193	19.8
f20–02	7	0.45	1093.6	1081.3	0.198	6.6
f20–06	7	0.80	955.2	477.9	0.224	15.7
f20–07	6	0.46	1289.7	691.6	0.223	7.9
f20–08	6	0.32	1346.4	1024.1	0.201	6.4
f20–09	5	0.46	1697.1	537.5	0.225	8.1
f20–11	5	0.40	2268.0	1041.1	0.236	6.0
f20–12	5	0.40	1899.1	857.4	0.215	6.1

TABLE V (cont.)

Sample Data Fit Information

Sample Number	Ion Energy (MeV)	χ^2/dof	a_{sat} ($10^{12}\frac{ions}{cm^2}$)	c_1	c_2	a_2 ($10^{12}\frac{ions}{cm^2}$)
f20–13	4	1.28	2711.9	494.6	0.259	7.4
f20–14	4	0.29	1705.8	82.0	0.065	38.0
f20–16	3	0.08	2242.8	65.8	-0.017	29.3
f20–17	3	0.18	2250.9	103.3	-0.191	324.7
f20–18	3	0.95	2251.1	65.0	-0.231	388.7
f23–01	3	1.71	2260.0	35.5	-0.708	3731.7
f23–02	3	0.27	2217.4	38.8	-0.029	51.8
f23–03	3	1.58	2298.4	86.6	-0.340	354.5
f23–04	2	4.27	3131.6	13.6	-0.107	44.9
f23–05	2	0.33	3142.4	20.1	-0.078	44.3
f23–06	2	0.55	3195.2	19.0	-0.082	43.1
f23–07	1	1.10	4179.6	4.1	-0.142	55.9
f23–08	1	1.89	4467.1	2.2	-0.154	59.7
f23–09	15	0.44	1106.4	2144.8	0.185	4.3
f23–10	15	2.91	1100.6	2217.0	0.189	5.1
f23–11	15	0.18	890.5	1173.3	0.224	6.5
f23–12	15	0.26	2577.2	5365.9	1.153	37.7
f23–14	15	1.99	2471.5	5400.7	1.139	37.3
f23–15	15	2.84	783.9	885.0	0.309	13.4
f23–16	20	0.46	1021.5	602.7	0.254	6.9
f23–17	20	0.49	1111.2	983.6	0.258	5.5
f23–18	25	1.11	1527.6	779.0	0.246	7.9
f28–01	25	2.10	1212.8	223.6	0.186	7.0
f28–02	30	3.68	2102.2	768.5	0.225	6.6
f28–04	30	1.52	2027.1	796.0	0.241	7.0
f28–05	30	0.71	2040.8	880.3	0.204	6.2
f28–06	35	2.39	4233.7	1634.0	0.188	5.4
f28–07	35	0.66	3200.5	597.2	0.251	6.6
f28–08	40	0.13	6393.6	1562.7	0.244	8.3
f28–09	40	0.26	5606.7	1281.3	0.261	8.1
f28–10*	45	—	—	—	—	—

---

* Only three data points for this run.

TABLE V (cont.)

Sample Data Fit Information

Sample Number	Ion Energy (MeV)	χ^2/dof	a_{sat} $(10^{12}\frac{ions}{cm^2})$	c_1	c_2	a_2 $(10^{12}\frac{ions}{cm^2})$
j21–01	10	5.38	690.8	1389.0	0.156	15.5
j21–02	8	0.99	1076.4	1216.0	0.208	5.5
j21–04	4	0.61	3530.3	354.4	0.302	11.9
j10–01	15	5.54	656.2	1671.0	0.190	8.6
j13–01	24	0.99	1753.4	823.2	0.270	9.4
j18–03	20	1.04	1926.2	1138.8	0.148	4.8
j18–04	20	0.48	1758.3	474.2	0.279	11.7
o02–01	20	2.21	1476.5	1035.6	0.268	9.5
o31–01	13	4.75	702.2	1452.7	0.322	3.1
s23–01	15	1.11	951.6	1341.7	0.322	5.8

REFERENCES

(Ab75) B. Abeles, P. Sheng, M.D. Coutts, and Y. Arie, Structural and Electrical Properties of Granular Metal Films, *Advances in Physics*, **24** (1975) 407.

(Ab82) J.S. Abel, H. Mazurek, D.R. Day, E.W. Maby, S.T. Senturia, G. Dresselhaus, and M.S. Dresselhaus, Electrical Properties of Ion Implanted Poly(P-Phenylene Sulfide), *Metastable Materials Formation by Ion Implantation*, eds. S.T. Picraux, W.J. Choyke (Elsevior Science, New York, 1982), p.173.

(Am71) V. Ambegaokar, B.I. Halperin, and J.S. Langer, Hopping Conductivity in Disordered Systems, *Physical Review B*, **4** (1971), 4.

(Ba83) H. Baumann, K. Bethge, F. Rauch, W. Reeh, and H. Wirth, Further Investigations on Hydrogenated Carbon Foils, *Jahresbericht GSI* (1983).

(Ch77) C.K. Chiang, C.R. Fincher, Jr., Y.W. Park, A.J. Heeger, H. Shirakawa, E.J. Louis, S.C. Gau, and A.G. MacDiarmid, Electrical Conductivity in Doped Polyacetylene, *Physical Review Letters*, **39** (1977), 1098.

(Di83) B. Dischler, A. Bubenzer, and P. Koidl, Bonding in Hydrogenated Hard Carbon Studied by Optical Spectroscopy, *Solid State Communications*, **48** (1983), 105.

(Dr84) M.S. Dresselhaus, B. Wasserman, and G.E. Wnek, Ion Implantation of Polymers, p. 413; B. Wasserman, G. Braunstein, M.S. Dresselhaus, and G.E. Wnek, Implantation-Induced Conductivity of Polymers, p. 423;

B.S. Elman, M.S. Dresselhaus, G. Braunstein, G. Dresselhaus, T. Venkatesan, B. Wilkens, and J.M. Gibson, Two-Dimensional Ordering of Ion Damaged Graphite, p. 461;

T. Venkatesan, B.S. Elman, G. Braunstein, M.S. Dresselhaus, and G. Dresselhaus, Channeling Studies of Thermal Regrowth in Ion Damaged Graphite, p. 467;
G. Braunstein B.S. Elman, M.S. Dresselhaus, G. Dresselhaus, and T. Venkatesan, High Temperature Implantation in Graphite, p. 475;
L. Salamanca-Riba, B.S. Elman, M.S. Dresselhaus, and T. Venkatesan, Stoichiometric Determination of Graphite Intercalation Compounds Using Rutherford Backscattering Spectrometry, p. 481;
L.E. McNeil, B.S. Elman, M.S. Dresselhaus, G. Dresselhaus, and T. Venkatesan, Magnetoreflection in Ion-Implanted Graphite, p. 493; *Materials Research Society Symposia Proceedings, Volume* **27**, *Ion Implantation and Ion Beam Processing of Materials*, Boston, November 1983, eds. G.K. Hubler, C.R. Clayton, O.W. Holland, and C.W. White (North Holland, New York, 1984).

(Ha72) E.M. Hamilton, Variable Range Hopping in a Non-Uniform Density of States, *Philosophical Magazine*, **26** (1972), 1043.

(He85) A. Hedin, P. Håkansson, B. Sundqvist, and, R.E. Johnson, Ion-Track Model for Fast-Ion-Induced Desorption of Molecules, *Physical Review B*, **31** (1985), 1780.

(Hi83) T. Hioki, S. Noda, M. Sugiura, M. Kakeno, K. Yamada, and J. Kawamoto, Electrical and Optical Properties of Ion-Irradiated Polymer Kapton H, *Applied Physics Letters*, **43** (1983), 30.

(Ka78) R. Katz, Track Structure Theory in Radiobiology and in Radiation Detection, *Nuclear Track Detection*, **2** (1978), 1.

(Ko68) E.J. Kobetich and R. Katz, Energy Deposition by Electron Beams and δ Rays, *Physical Review B*, **170** (1968), 391.

(Ma83) H. Mazurek, D.R. Day, E.W. Maby, J.S. Abel, S.D. Senturia, M.S. Dresselhaus, and G. Dresselhaus, Electrical Properties of Ion- Implanted Poly(p-Phenylene Sulfide), *Journal of Polymer Science: Polymer Physics Edition*, **21** (1983), 537.

(Mo68) N.F. Mott, Conduction In Glasses Containing Transition Metal Ions, *Journal of Non-Crystalline Solids*, **1** (1968), 1.

(Mo87) N.F. Mott, *Conduction In Non-Crystalline Materials* (Clarendon Press, Oxford, 1987), p.29.

(Ni79) P.J. Nigrey, A.G. MacDiarmid, and A.J. Heeger, Electrochemistry of Polyacetylene, $(CH)_x$: Electrochemical Doping of $(CH)_x$ Films to the Metallic State, *Journal of the Chemical Society, Chemical Communications*, Number 14 (1979), 594.

(No70) L.C. Northcliffe and R.F. Schilling, Range and Stopping-Power Tables for Heavy Ions, *Nuclear Data Tables*, **A7** (1970), 233.

(No84) K. Nobuyoshi and Y. Wachi, Application of Ion Implation for Doping of Polyacetylene Films, *Applied Physics Letters*, **45** (1984), 436.

(Ol32) F. Ollendorf, *Potentialfelder der Elektrotechnik* (Springer, Berlin, 1932), p.168.

(St87) G.J. Stecher, The Formation of Graphite in Amorphous Carbon Under Heavy Ion Bombardment, Senior Thesis, California Institute of Technology, 1987.

(Sz81) S.M. Sze, *Physics of Semiconductor Devices*, 2^{nd} *Edition* (John Wiley & Sons, New York, 1981), p.849.

(Ta80) T. Tani, P.M. Grant, W.D. Gill, G.B. Street, and T.C. Clark, Phototransport Effects in Polyacetylene, $(CH)_x$, *Solid State*

Communications, **33** (1980), 499.

(Ve83) T. Venkatesan, S.R. Forrest, M.L. Kaplan, C.A. Murray, P.H. Schmidt, and B.J. Wilkens, Ion-Beam-Induced Conductivity in Polymer Films, *Journal of Applied Physics*, **54** (1983), 3150.

(Ve85) T. Venkatesan, R. Livi, T.C. Banwell, T. Tombrello, M. Nicolet, R. Hamm, and A.E. Meixner, Modification of Electronic Transport in Polymer and Carbon Films by High and Low Energy Ion Irradiation, *Materials Research Society Symposia Proceedings, Volume* **45**, *Ion Beam Processes in Advanced Electronic Materials and Device Technology*, San Francisco, April 15–18 1985, eds. F.H. Eigen, T.W. Signan, and B.R. Appleton (Materials Research Society, Pittsburgh, 1985), p.189.

(We89) D.L. Weathers, Sputtering by Multiply-Charged Ions, and Preferential Sputtering of Isotopic Mixtures, Ph.D. Thesis, California Institute of Technology, 1989.